Cosmological Variations in the Space–Time Distribution of Absorption Systems in Quasar Spectra

A. I. Ryabinkov, A. D. Kaminker*, and D. A. Varshalovich

Ioffe Physical-Technical Institute, Russian Academy of Sciences, Politekhnicheskaya ul. 26, St. Petersburg, 194021 Russia
Received April 13, 2001

Abstract—Based on the catalog of Junkkarinen *et al.* (1991), we analyze the space–time distribution of absorption systems in quasar spectra at cosmological redshifts $z = 0$–3.7. The z distribution of absorbing matter is shown to have a pattern of alternating maxima (peaks) and minima (dips). Within statistical uncertainty, the positions of such peaks and dips do not depend on the direction of observation. We have found a periodicity in the distribution of absorption systems in the functions $\ln(1 + z)$ and $(1 + z)^{-1/2}$. We show that the derived sequence of maxima and minima in the space–time distribution of absorbing matter is not a manifestation of the spatial large-scale structure alone, but it is more likely temporal in nature. The most probable source of the putative structure could be an alternation (in the course of cosmological evolution) of pronounced and depressed epochs with a characteristic time interval of 520 ± 160 Myr, depending on the cosmological model chosen. © *2001 MAIK "Nauka/Interperiodica".*

Key words: *galaxies, quasars, absorption line systems, large-scale structure of Universe*

1. INTRODUCTION

Most current cosmological models are based on the so-called cosmological principle (see, e.g., Peebles 1993). It suggests that all points in space are equivalent and that the Universe is, on average, homogeneous and isotropic. This principle has been reliably confirmed by recent observations of the cosmic microwave background radiation on angular scales up to $\vartheta \sim 1°$ at a relative level of $\sim 10^{-5}$ (see, e.g., de Bernardis *et al.* 2000). On the other hand, the distribution of matter in the immediate vicinity of our Galaxy is nonuniform. Moreover, in addition to the ordinary small-scale inhomogeneity of galaxies, a large-scale hierarchy extending from hundreds of kpc to hundreds of Mpc has been reliably detected (Miller and Batuski 2000). The largest observed inhomogeneities of matter corresponding to k $k \lesssim 0.1h$ Mpc^{-1} [where $k = 2\pi/L$ is the wave number that determines the components of the power spectrum, L is the corresponding spatial scale in Mpc, $h = H_0/(100$ km s^{-1} Mpc$^{-1})$, and H_0 is the Hubble constant] are widely believed to form the so-called large-scale structure of galaxy clusters and superclusters (see, e.g., Broadhurst *et al.* 1990; Landy *et al.* 1996; Einasto *et al.* 1997, 1999). The existence of such a structure was established by statistically analyzing deep surveys of galaxies and galaxy clusters for relatively low cosmological redshifts ($z \lesssim 0.5$). Accordingly, it is of particular interest to study the space–time distribution of matter at high redshifts.

The spatial correlation function for C IV absorption systems in quasar spectra along the line of sight was analyzed by Quashnock *et al.* (1996) in the redshift range $z = 1.2$–4.5. They found that the C IV absorbers tend to be clustered on comoving scales ($\sim 100h^{-1}$ Mpc) typical of the large-scale structure. However, the pair correlation function used in this paper describes only the relative distribution of absorption systems and does not provide complete information inhomogeneities in the z distribution (see section 3).

This work is a continuation of our studies of the space–time distribution of matter initiated previously [see Ryabinkov *et al.* (1998, 1999), below referred to as Papers I and II; Kaminker *et al.* (2000), below referred to as Paper III]. In the above papers, we used the resonance doublets of C IV and Mg II absorption systems observed in quasar spectra at cosmological redshifts $z = 0.2$–3.2 as an indicator of matter, with special emphasis on the selection of statistical material to remove the possible selection effects. Here, we use considerably larger statistical material from the catalog by Junkkarinen *et al.* (1991) in the extended range $z = 0$–3.7 without any additional restrictions. Below, we present the results of our statistical analysis and discuss their possible cosmological implications.

2. RESULTS

2.1. Nonuniformity of the Distribution

Figure 1a shows the z distribution of 847 absorption systems composed of more than 2200 absorption lines in the range $z = 0$–3.7 broken down into $n = 52$ equal

---

* E-mail address for contacts: kam@astro.ioffe.rssi.ru

independent bins. This breakdown corresponds to the bin width $\Delta z = 0.071$ obtained in Papers I, II, and III by analyzing the dependence of the χ^2 test (which characterizes the deviation from the hypothesis of a uniform distribution) on the number of bins n in the z range under consideration (for more details, see Paper III). Here, we performed a similar analysis. We broke down the range $z = 0$–3.7 into n equal independent bins, but with the difference that the χ^2 test was used to test the hypothesis of a uniform distribution of absorption systems relative to the smooth trend (Fig. 1a). The trend is attributable to observational selection at low ($z \lesssim 1$) and high ($z \gtrsim 2$) redshifts. For each n, we described the trend in two ways: (i) by two (ascending and descending) linear functions of the form $N_{tr} = az + b$ and (ii) by a parabolic function $N_{tr} = az^2 + bz + c$, where the coefficients a, b, and c were determined by the least squares method (LSM). The maximum deviation from the hypothesis of a uniform distribution was found (at a significance level $>3\sigma$) to correspond to $n = 52$ and $n = 53$ for cases (i) and (ii), respectively. This yields bin widths that virtu-

ally coincide with those obtained previously: $\Delta z = 0.071$ in case (i) and $\Delta z = 0.070$ in case (ii).

Figure 1b shows the distribution of the same absorption systems obtained by the so-called moving-average method, which allows the positions of maxima and minima to be determined more accurately (within the bin width). In this case, we counted the number of absorptions in bin $\Delta z = 0.071$, which was sequentially displaced along the z axis at steps of $h_z = 0.01$. Subsequently, we subtracted a trend and determined the positions peaks and dips relative to the derived horizontal level. The positions of peaks z_{max} and dips z_{min} were determined as weighted means (centroids) of the points that formed the peak (dip). The significance of peaks and dips was estimated by the method of a transforming function, which ensures a constant (unit) variance of the frequencies of absorptions being fallen within each of the established bins (for more details, see Paper III). Note that the inferred positions of peaks (dips) and their statistical significance, within statistical uncertainty, did not depend on how the trend was drawn.

The table gives z_{max} and z_{min} obtained here (with an accuracy of ± 0.04) and significance levels of the corresponding peaks (columns 3, 5 and 4, 6, respectively). Also given for comparison are z_{max} from Papers I, II, and III for Mg II and C IV systems in the ranges $z = 0.2$–2.1 (column 1) and $z = 1.2$–3.2 (column 2), respectively. We can see good agreement between the corresponding z_{max} within the limits of the above errors. All the peaks detected in the distribution of Mg II systems and all but one of the peaks ($z_{max} = 2.64$) in the distribution of C IV systems have been confirmed. Note also the appearance of new peaks, $z_{max} = 0.22$, 3.16, and 3.56, at a 2σ significance level.

To test the results, we also performed a similar analysis for different numbers of bins n in the full z range, i.e., for different bin widths. In particular, for $n = 29 \simeq \sqrt{847}$ (bin width $\Delta z = 0.128$), we also found a series of peaks with essentially the same centroids (cf. table), $z_m = 0.22$, 0.45, 0.80, 1.08, 1.31, 1.45, 1.66, 1.96, 2.39, 2.87, 3.15, and 3.56 (with an accuracy of ± 0.064), but with lower significance levels, 1.5σ, 2σ, 2σ, σ, σ, σ, σ, 2.5σ, 2σ, 3σ, 2σ, and 1.5σ. We can see that only two peaks with the centroids $z_{max} = 1.75$ and 2.13 whose significance is too low ($<\sigma$) are absent. On the other hand, for $n > 52$, additional peaks appear at a low significance level ($<\sigma$), which are more likely attributable to statistical fluctuations. An analysis shows that the above bin width ($\Delta z = 0.071$) corresponds to the highest significance of the distinguished sequence of inhomogeneities in the z distribution of absorption systems.

Fig. 1. The z distribution of absorption systems: (a) a histogram; (b) the distribution obtained by the moving-average method, i.e., by sequentially displacing the bin $\Delta z = 0.071$ along the z axis at steps of 0.01.

2.2. Isotropy of the Distribution

To determine the possible spatial variations in the z distributions of absorption systems, we compared the z distributions obtained both in opposite (independent) hemispheres separated by the meridional plane and in
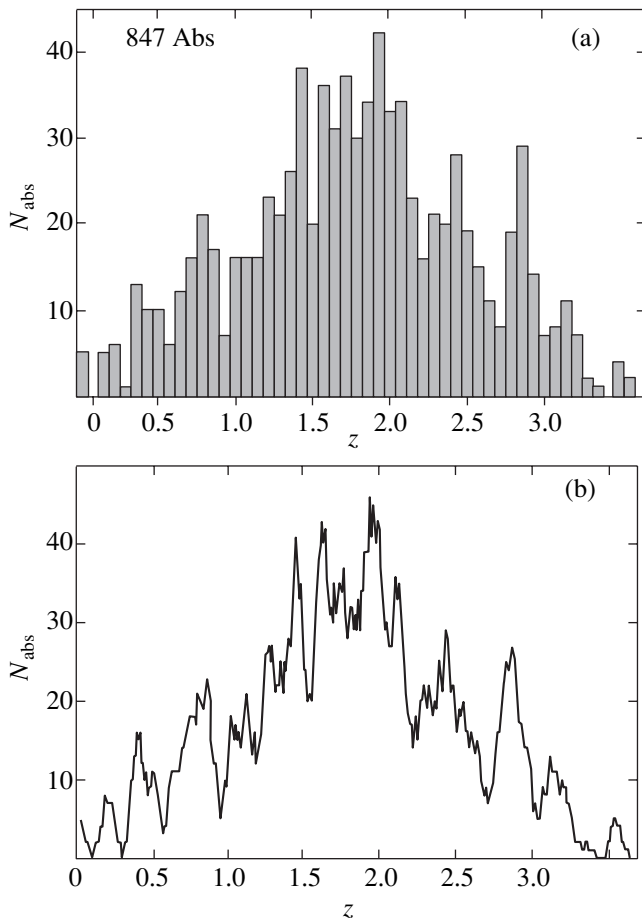
independent (nonoverlapping) 90° (6-hour) sectors. We constructed the z distributions in 12 pairs of hemispheres derived by sequentially rotating the meridional plane in the equatorial coordinate system around the celestial axis $\delta = \pm 90°$ at steps $\Delta\alpha = 15°$ (1^h), where δ and α are the declination and right ascension, respectively. Similar calculations were performed in the Galactic coordinate system (Galactic longitude l and latitude b). In this case, the plane dividing the celestial sphere into two equal parts was rotated around the axis passing through the north and south Galactic poles (at the same step $\Delta l = 15°$). When constructing the z distributions in each hemisphere, we determined the trend and calculated the function $y(z) = N(z) - N_{tr}(z)$ (trend subtraction). The trend was described by the above functions; the parameters were determined by the LSM. For each pair of opposite hemispheres, we calculated the correlation coefficient r between the corresponding functions $y(z)$, which was compared with the tabular value r_β of the sample correlation coefficient for a given sample size ($n = 52$) and confidence β. For $r > r_\beta$, the distributions may be considered to correlate with a confidence exceeding β. Figs. 2a and 2b show that the pairwise correlation of the distributions is significant at a level $\geq (2$–$3)\sigma$ for all pairs of independent hemispheres in the equatorial and Galactic coordinate systems. Similarly, we calculated the correlation coefficients between the distributions derived for $n = 29$ ($\Delta z = 0.128$). In this case, the significance levels of the correlation coefficients slightly increased.

Figures 3a and 3b show the z distributions of the absorption systems for each of the 24 hemispheres in the equatorial and Galactic coordinate systems. The black and white regions correspond to enhanced (maxima) and reduced (minima) concentrations of absorption systems, respectively. We can see the solid black vertical bands corresponding to all the maxima z_{max} in the table except for $z_{max} = 1.1$ and 1.75. For the latter maxima, the bands are fragmentary in pattern, probably because of insufficient statistics or observational selection. Note also a similar correspondence between the positions of white bands and z_{min}. For the solid bands, the positions of maxima (and minima) in the z distributions do not depend (within the error limits) on the coordinate of the center of the rotating hemisphere, α_c or l_c; i.e., they are the same for all hemispheres. We see from a comparison of Figs. 3a and 3b that the band positions did not change when passing from the equatorial coordinate system to the Galactic one. This also suggests that the positions of maxima and minima in the z distributions do not depend on the direction of observation.

Figures 4a and 4b show similar distributions for 90° (6-hour) sectors: $\alpha_c - 45° \leq \alpha \leq \alpha_c + 45°$ (α_c is the right ascension of the sector center) and $l_c - 45° \leq l \leq l_c + 45°$ (l_c is the Galactic longitude of the sector center) for the equatorial and Galactic coordinate systems, respectively. The distributions were constructed for 24 sectors formed by sequentially rotating α_c and l_c around the
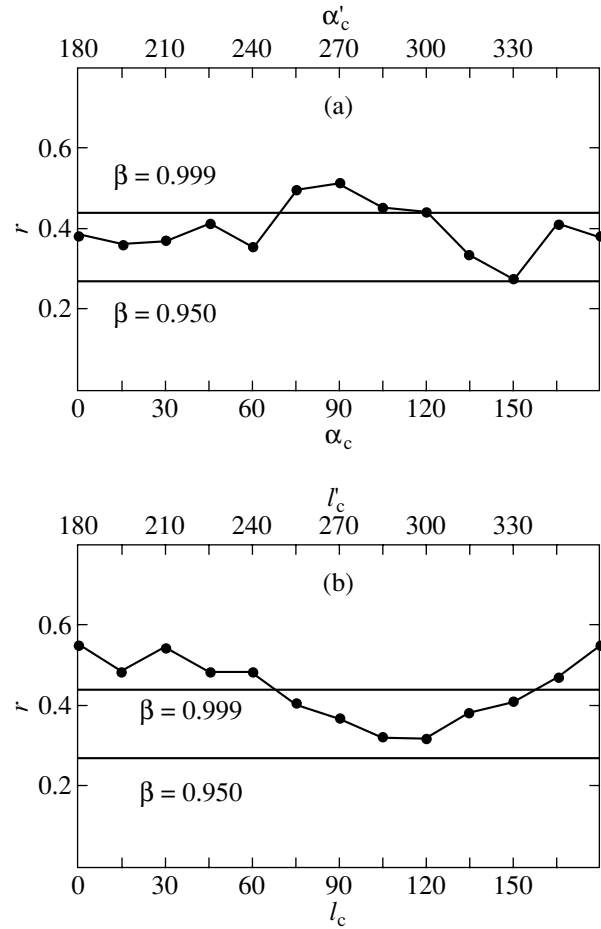
Fig. 2. Correlation coefficient r between the z distributions of absorption systems in pairs of opposite hemispheres. (a) The equatorial coordinate system, where α_c and α'_c are the right ascensions of the centers of opposite hemispheres. (b) The Galactic coordinate system, where l_c and l'_c are the Galactic longitudes of the centers of opposite hemispheres. The straight lines indicate the tabular values $r_\beta = 0.490$ for the confidence level $\beta = 0.999$ (3σ) and $r_\beta = 0.304$ for $\beta = 0.950$ (2σ).

celestial axis (Galactic axis) at steps of 15°. Because of insufficient statistics, the black and white bands became more tortuous and fragmentary than those in Figs. 3a and 3b. In general, however, the structure of the black and white bands remained as before. Several solid black bands do not go outside the error band near the centroids of the most significant peaks: $z_{max} = 0.45$, 0.79, 1.44, 2.42, 2.87, and 3.56. Several other black bands, for example, those near $z_{max} = 0.22$, 1.28, 1.63, 1.96, and 3.16, are more fragmentary in pattern than those in Figs. 3a and 3b but contain solid vertical portions that considerably exceed the width of the individual sector. As in Figs. 3a and 3b, the positions of the bands and their pattern do not change significantly when passing from the equatorial coordinate system to the Galactic one (cf. Figs. 4a and 4b).
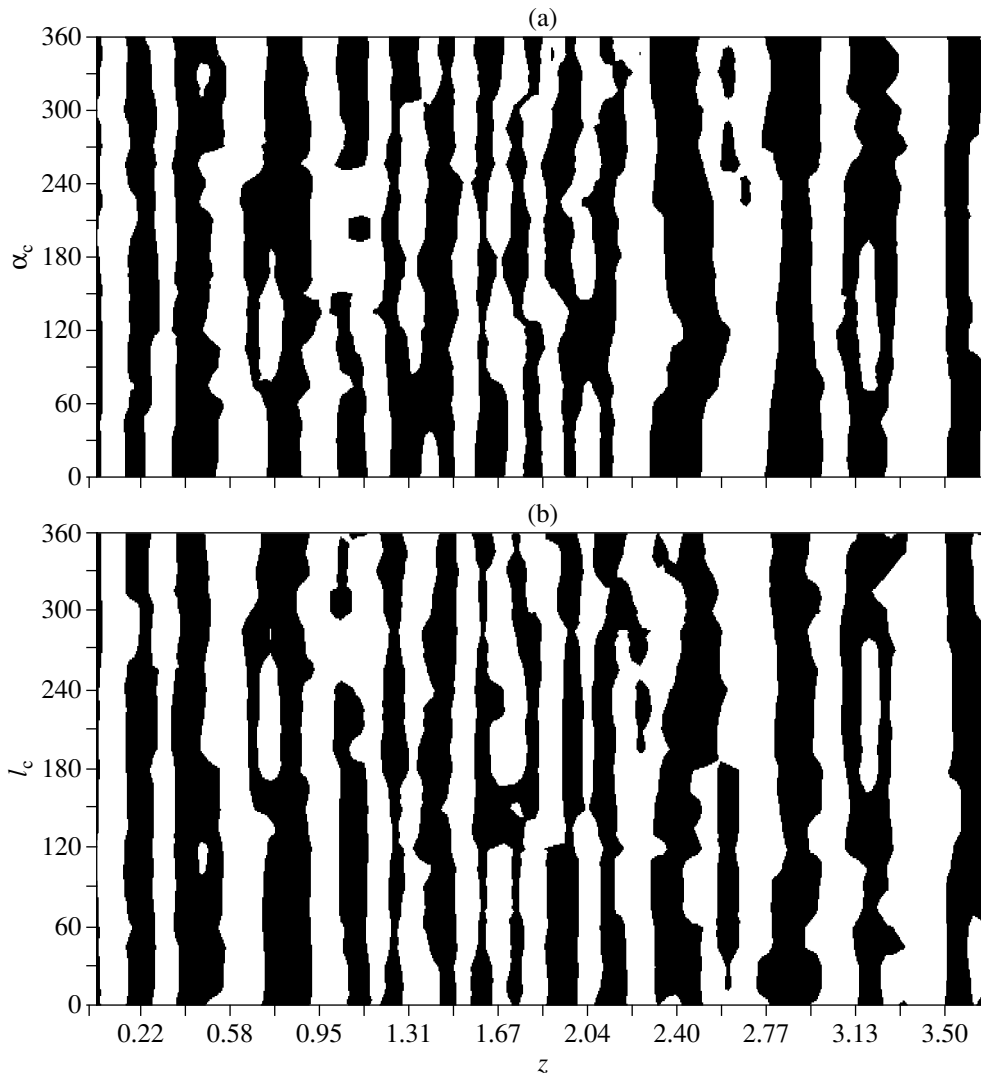
Fig. 3. The *z* distribution of absorption systems in 24 hemispheres. (a) The equatorial coordinate system; the right ascensions α_c of the hemisphere centers are plotted along the vertical axis, in degrees. (b) The Galactic coordinate system; the Galactic longitudes l_c of the hemisphere centers are plotted along the vertical axis.

We also calculated the correlation coefficients between the distributions in 156 pairs of independent 90° sectors. In the equatorial coordinate system, the correlation is significant at a level $\geq 2\sigma$ in 150 of the 156 pairs. In the Galactic coordinate system, the correlation between the distributions is significant at the same level for all pairs of independent sectors.

Thus, the high correlation between the *z* distributions in pairs of independent hemispheres and in non-overlapping pairs of 90° sectors, as well as the fixed (within statistical uncertainty) positions of maxima (peaks) and minima (dips) in these distributions for various orientations of the hemispheres and 90° sectors (black and white bands in Figs. 3a, 3b and 4a, 4b, respectively) suggest that the system of alternating peaks and dips in the distribution of absorbing matter in the redshift range under consideration is isotropic.

2.3. Estimating the Periodicity

We tested the regularity (periodicity) of the derived *z* distribution within the entire range $0 \leq z \leq 3.7$ under consideration. The test was performed by two independent methods: (i) a regression analysis of the positions of peaks z_{max} and dips z_{min}; and (ii) an analysis of the power spectrum for the total number of absorption systems considered. We searched for a periodicity in four trial functions of argument *z*:

$$f_1(z) = \ln(1+z), \quad f_2(z) = (1+z)^{-1/2},$$
$$f_3(z) = (1+z)^{-1}, \quad f_4(z) = (1+z)^{-3/2}. \tag{1}$$

Note that in this paper, we restrict ourselves to searching for the principal possibility of periodicity without discussing conclusions referring to specific cosmological models.

Redshifts z_{max} and z_{min} corresponding to the maxima and minima in the z distribution of absorption systems

MgII 216 systems	CIV 299 systems	847 systems	Significance level	847 systems	Significance level
z_{max}	z_{max}	z_{max}	σ	z_{min}	σ
		0.22	2	0.10	2
0.44		0.45	3	0.31	3
0.77		0.79	3	0.58	3
1.04		1.10	1	0.96	2
1.30		1.28	1	1.18	1
	1.46	1.44	2	1.35	1
1.66	1.60	1.63	2	1.54	2
1.78	1.78	1.75	1	1.71	1
	1.98	1.96	2	1.84	1
	2.14	2.13	1	2.07	1
	2.45	2.42	3	2.24	2
	2.64				
	2.86	2.87	3	2.72	3
		3.16	2	3.05	2
		3.56	2	3.40	3

(i) As a regression model, we considered an equation of the form $f_k(z_k(l)) = a_k + \Delta_k l$, where $k = 1, 2, 3, 4$; a_k is the initial constant; and $\Delta_k = f_k(z_k(l + 1)) - f_k(z_k(l))$ is the constant shift between the values of trial function f_k at two succeeding points, $z_k(l + 1)$ and $z_k(l)$. In the approach, the sequences of maxima $z_{max}(n)$ or minima $z_{min}(n)$ given in the table, where $n = 1, 2, \ldots$ number the peaks or dips in order of increasing z, are correlated with the sequences of points $z_k(l)$ (different for different k), where $l = 0, 1, 2, \ldots$ is the period number of trial function $f_k(l)$ (in general, $l \geq n$). We found that for the trial functions f_1 and f_2, the hypotheses about periodicity of the derived peaks z_{max} and independently dips z_{min} are significant at a level $>3\sigma$. The corresponding regression coefficients for z_{max} and z_{min} (primed) are given below:

$$\Delta_1 = 0.068 \pm 0.002, \quad a_1 = 0.001 \pm 0.029;$$

$$\Delta_2 = 0.019 \pm 0.001, \quad a_2 = -0.001 \pm 0.027;$$

$$\Delta_1' = 0.069 \pm 0.002, \quad a_1' = 0.028 \pm 0.026; \tag{2}$$

$$\Delta_2' = 0.019 \pm 0.001, \quad a_2' = 0.009 \pm 0.026.$$

We can see that the parameters obtained independently for the sequences of $z_{max}(n)$ and $z_{min}(n)$ are in good agreement.

(ii) We analyzed the power spectrum for the four trial functions in (1). The power spectrum was defined in a standard way:

$$P(m) = \frac{1}{\mathcal{N}}\left\{\left[\sum_{i=1}^{\mathcal{N}} \tilde{y}(z_i)\cos\left(\frac{2\pi m f_k(z_i)}{F_k}\right)\right]^2 + \left[\sum_{i=1}^{\mathcal{N}} \tilde{y}(z_i)\sin\left(\frac{2\pi m f_k(z_i)}{F_k}\right)\right]^2\right\}, \tag{3}$$

where $\mathcal{N} = 363$ is the number of points in the distribution shown in Fig. 1b, which was obtained by the moving-average method (see subsection 2.1); $\tilde{y}(z_i) = y(z_i) - \sum_{i=1}^{\mathcal{N}} y(z_i)/\mathcal{N}$, with $y(z_i) = N(z_i) - N_{tr}(z_i)$; here, $N(z_i)$ is the number of absorption systems in the ith bin, z_i being the coordinate of its center, and $N_{tr}(z_i)$ is the trend described by a parabolic function; $f_k(z_i)$ is one of the four trial functions (1), $F_k = |f_k(z_{\mathcal{N}}) - f_k(z_1)|$ is the full interval of function $f_k(z_i)$; m is the harmonic number or the number of periods in the full interval F_k. The search for harmonic components was made in the same range of periods (frequencies) in which the above results of our regression analysis were obtained. Since the total number of established periods l varied from 23 (model f_1) to 41 (model f_4), we chose only the high-frequency portions of the spectrum corresponding to $22 \leq m \leq 48$ for our spectral analysis. To obtain more reliable results of the harmonic analysis characterizing the isotropic component in the distribution of absorption systems, we constructed the power spectra separately in pairs of independent hemispheres. Subsequently, we calculated an arithmetic mean of the spectra in each pair.

Figure 5 shows typical results of averaging pairs of spectra for each of the four trial functions in two independent hemispheres: $0° \leq \alpha < 180°$ and $180° \leq \alpha < 360°$. The power spectra of trial functions f_1 and f_2 are seen to contain peaks ($m = 23$ and 28, respectively) whose significance level exceeds 3σ. The corresponding periods, $\Delta_1 = 0.066 \pm 0.002$ and $\Delta_2 = 0.0186 \pm 0.0004$, are in good agreement with the results of our regression analysis [see (2)].

Thus, the results of applying the two methods under discussion suggest that the derived system of peaks and dips is regular (at a significance level $>3\sigma$). Note that our regression analysis confirms the results obtained in
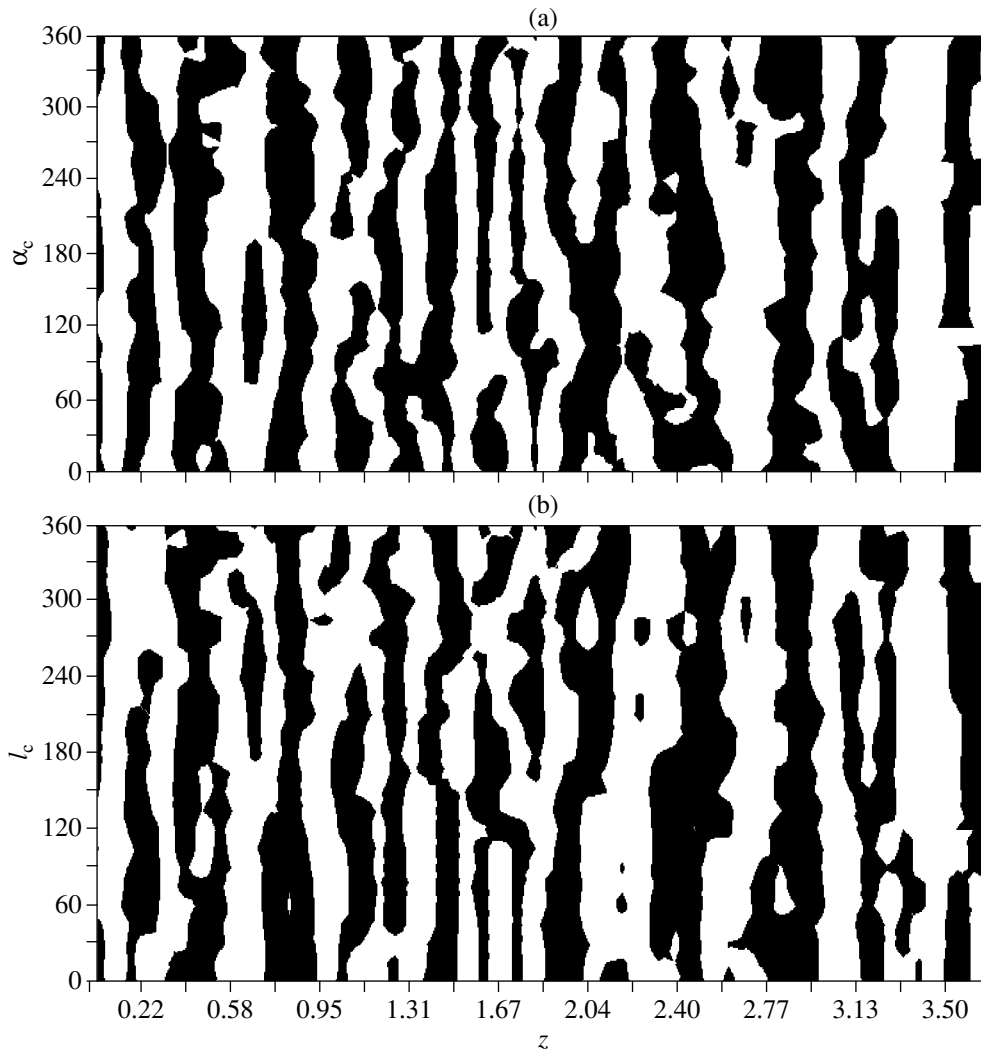
Fig. 4. Same as Fig. 3 for the *z* distributions obtained for 90° sectors with the same relative displacement of 15° (1$^{\text{h}}$): (a) α_c are the right ascensions of the sector centers, in degrees; (b) l_c are the Galactic longitudes of the sector centers.

Paper III by the same method for the distribution of C IV and Mg II absorption systems in the redshift range $0.2 \leq z \leq 3.2$.

A peak in the power spectrum for the distribution of C IV and Mg II absorption systems for the trial function f_1 that corresponded to the period $\Delta_1 = 0.066 \pm 0.003$ was found in the same paper, which is in agreement with the results of this paper. Note also that the significance level of this peak given in Paper III ($>2\sigma$) was underestimated. A more accurate estimate gives a level exceeding 4σ.

3. CONCLUSIONS AND DISCUSSION

Our statistical analysis of the distribution of 847 absorption systems in the redshift range $z = 0$–3.7 confirms the main conclusions of Papers I, II, and III. Below, we briefly formulate our results.

(1) The *z* distribution of absorption systems is non-uniform. A system of alternating maxima (peaks) and minima (dips) stands out against the background of a smooth nonuniformity (trend). The significance of most peaks exceeds 2σ, but some of them are less significant, probably because of insufficient statistics. The positions of maxima and minima (centroids of the corresponding peaks and dips) in the distribution of absorption systems are given in the table with an accuracy of ±0.04.

(2) The positions of maxima and minima in the *z* distribution do not depend on the direction of observation, within statistical uncertainty. In particular, we found a correlation (at a significance level $\gtrsim 2\sigma$) between the *z* distributions in 12 pairs of opposite (independent) hemispheres and in 150 pairs of independent 90° sectors.

(3) The above system of peaks and dips shows certain regularity. The power spectra for the *z* distribution

obtained in the trial functions $f_1 = \ln(1 + z)$ and $f_2 = (1 + z)^{-1/2}$ contain peaks whose significance level exceeds 3σ. The trial functions (1) reflect the z dependencies of cosmological time in various cosmological models. Thus, we showed that there are cosmological models in which peaks with a certain period can appear in the distribution of absorbing matter.

(4) The derived distribution of absorption systems is most likely coupled with the appearance of alternating pronounced (peaks) and depressed (dips) epochs in the course of cosmological evolution, i.e., with the existence of cosmological variations (CVs).

(5) The characteristic time interval T between the maxima of pronounced epochs strongly depends on the trial function chosen and, hence, on the adopted cosmological model. For example, we can estimate the periods $T_1 = \Delta_1/H_0 = (660 \pm 20)h^{-1} \times 10^6$ yrs and $T_2 = 2\Delta_2/H_0 = (380 \pm 20)h^{-1} \times 10^6$ yrs for the trial functions f_1 and f_2, respectively.

It should be noted that the hypothesis about the existence of CVs at cosmologically distant epochs considered here is consistent with the cosmological principle mentioned in the Introduction. The observed isotropic structure does not correspond to a particular fixed cosmological time, but it most likely to be specific for cosmological evolution. The epoch of hydrogen recombination associated with the formation of cosmic microwave background serves as an example of this kind of pronounced epoch.

An additional argument for the idea of pronounced and depressed epochs can be the testing in Paper III of the hypothesis that the system of peaks in the derived space–time distribution results from an enhanced concentration of absorbing matter in the direction of large galaxy clusters and superclusters (see, e.g., Quashnock *et al.* 1996). Such regions of enhanced concentration of absorption systems could imitate the observed peaks in the z distribution. We constructed the distribution of C IV absorption systems by removing two groups of systems from the complete statistics: (i) we excluded double and triple associations of quasars (along with absorption systems in their spectra) within a $1° \times 1°$ angular box in the sky as well as the spectra of five quasars containing ≥ 4 C IV doublets within the spatial interval $100h^{-1}$ Mpc presented in Table 1 from Quashnock *et al.* (1996); and (ii) we excluded the groups of C IV systems with relative radial velocities $<10\,000$ km s^{-1}. Although the statistics was greatly reduced, the positions of peaks in the distributions (see the second column of the table) remained as before in both cases. The correlation coefficients between the two new distributions and the initial distribution based on the complete statistics of the selected C IV systems proved to be high (the significance levels were 3σ and 2σ, respectively). These results argue against the assumption that the derived sequence of peaks and dips results from a purely spatial clustering of absorption systems.
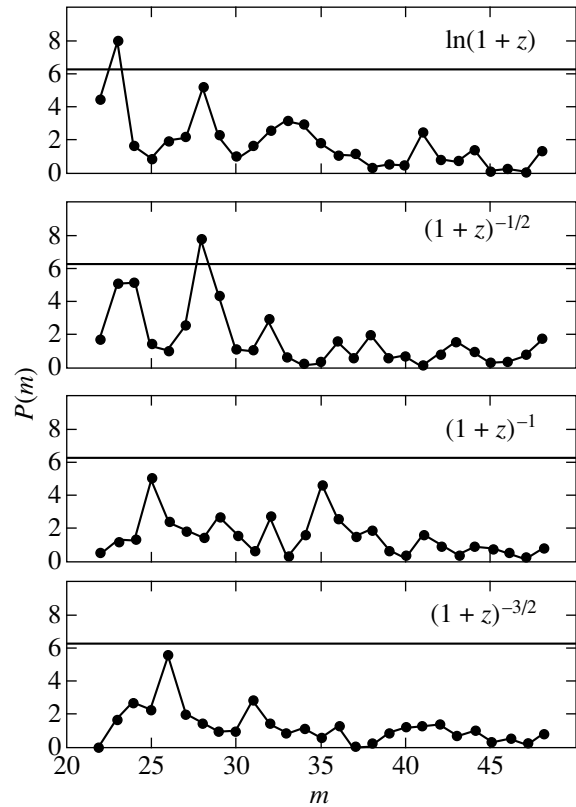
Fig. 5. Power spectra $P(m)$ (m is the harmonic number) for the total z distribution of the 847 absorption systems under consideration constructed for four trial functions [see (1)], which are indicated in each of the four panels. The horizontal lines in each panel specify the confidence level $\beta = 0.998$.

On the other hand, our hypothesis about temporal variability at cosmologically distant epochs is consistent with the existence of the spatial large-scale structure mentioned in the Introduction. Note, in particular, that our bin width significantly exceeds Δz, which is determined by the peculiar motions of galaxies, including their motions in clusters and superclusters as well as the possible gravitational shifts. Consequently, the approach under consideration leads to averaging of the inhomogeneities associated with the large-scale motions and spatial structures in the distribution of absorbing matter.

Note that the sequence of peaks in the z distribution of quasars was found by Burbidge and Burbidge (1967) and subsequently noted by many authors (see, e.g. Arp *et al.* 1990). Several maxima were also detected in the distribution of absorption systems (see Chu and Zhu 1989; Arp *et al.* 1990). Recently, Liu and Hu (1998) have shown that there is a significant sequence of alternating peaks and dips in the z dependence of the mean free path of an average photon $\lambda_0(z)$. They found the fitting function for $\lambda_0(z)$ to include a periodic component of the time variable $t = t_0(1 + z)^{-3/2}$ [the trial function f_4 of (1)] with the period $T = 155h^{-1} \times 10^6$ yrs. The positions of the minima of the periodic component in $\lambda_0(z)$

(z_m = 1.79, 2.02, 2.30, 2.66, 3.13) roughly correspond to the maxima in the distribution of absorption systems discussed here. By comparing this sequence of z_m with z_{max} from the table, we can see qualitative agreement between the two sequences. Moreover, the regression analysis in subsection 2.3 yields virtually the same period $T_4 = 2\Delta_4/3H_0 = (150 \pm 70)h^{-1} \times 10^6$ yrs, but at a lower significance level than the periods T_1 and T_2 presented above.

A periodicity of the peak positions in the z distribution of quasars in $\ln(1 + z)$ was first discovered by Karlsson (1971) (see also Karlsson 1977). The shifts between adjacent peaks on the scale of this function were found to correspond to a period $\Delta_1 \approx 0.20$. This period was confirmed by many authors (see, e.g., Fang *et al.* 1982; Khodyachikh 1988, 1990; Chu and Zhu 1989; Arp *et al.* 1990; Karlsson 1990) using different statistical material. In particular, the hypothesis about the existence of CVs considered here was advanced by Khodyzchikh (1990) based on a statistical analysis of the z distributions of quasar radio luminosities. Note that the period derived in subsection 2.3 in the same trial function $f_1(z)$ [see (2)] differs from the above value by a factor of 3 (within statistical uncertainty).

The appearance of pronounced epochs may be associated with the intrinsic evolutionary properties of galaxies and their clusters (see, e.g., Liu and Hu 1998). On the other hand, it can be understood in terms of the cosmological scenarios that consider the scalar field and/or phase transitions at late evolutionary stages. In turn, this may lead to quasi-periodic oscillations in effective gravitational constant G, Hubble constant H, cosmological constant Λ_0, etc. (see, e.g., Morikawa 1991; Damour and Polyakov 1994; Sisterna and Vucetich 1994).

The existence of CVs at cosmologically distant epochs seems to be a highly plausible explanation of the results obtained here and in the previous papers cited above. The rapid development of ground-based and space-borne observational facilities in the optical, infrared, and near-ultraviolet ranges in recent years gives hope that the hypothesis about the existence of pronounced epochs of enhanced and/or reduced concentration of luminous matter in the Universe can be tested in the immediate future. Note only that with the accumulation of statistical material, the CVs under discussion can show up with a higher probability at comparatively large redshifts ($z \gtrsim 1$), because the peculiar velocities of galaxies are comparable to the cosmological expansion velocities at low z ($z \ll 1$).

ACKNOWLEDGMENTS

REFERENCES

1. H. Arp, H. G. Bi, Y. Chu, and X. Zhu, Astron. Astrophys. **239**, 33 (1990).

2. T. J. Broadhurst, R. S. Ellis, D. C. Koo, and A. S. Szalay, Nature **343**, 726 (1990).

3. G. R. Burbidge and E. M. Burbidge, Astrophys. J. Lett. **148**, L107 (1967).

4. Y. Chu and X. Zhu, Astron. Astrophys. **222**, 1 (1989).

5. T. Damour and A. M. Polyakov, Nucl. Phys. B **423**, 532 (1994).

6. P. de Bernardis, P. A. R. Ade, J. J. Bock, *et al.,* Nature **404**, 955 (2000).

7. J. Einasto, M. Einasto, S. Gottlöber, *et al.*, Nature **385**, 139 (1997).

8. J. Einasto, M. Einasto, E. Tago, *et al.*, Astrophys. J. **519**, 441 (1999).

9. L. Fang, Y. Chu, Y. Liu, and Ch. Cao, Astron. Astrophys. **106**, 287 (1982).

10. V. Junkkarinen, A. Hewitt, and G. Burbidge, Astrophys. J., Suppl. Ser. **77**, 203 (1991).

11. A. D. Kaminker, A. I. Ryabinkov, and D. A. Varshalovich, Astron. Astrophys. **358**, 1 (2000).

12. K. G. Karlsson, Astron. Astrophys. **13**, 333 (1971).

13. K. G. Karlsson, Astron. Astrophys. **58**, 237 (1977).

14. K. G. Karlsson, Astron. Astrophys. **239**, 50 (1990).

15. M. F. Khodyachikh, Kinematika Fiz. Nebesnykh Tel **4**, 53 (1988).

16. M. F. Khodyachikh, Astron. Zh. **67**, 218 (1990) [Sov. Astron. **34**, 111 (1990)].

17. S. D. Landy, S. A. Shectman, H. Lin, *et al.*, Astrophys. J. Lett. **456**, L1 (1996).

18. Y. Liu and F. Hu, Astron. Astrophys. **329**, 821 (1998).

19. C. J. Miller and D. J. Batuski, astro-ph/0002295 (2000).

20. M. Morikawa, Astrophys. J. **369**, 20 (1991).

21. P. J. E. Peebles, *Principles of Physical Cosmology* (Princeton Univ. Press, Princeton, 1993).

22. J. M. Quashnock, D. E. Vanden Berk, and D. G. York, Astrophys. J. Lett. **472**, L69 (1996).

23. A. I. Ryabinkov, D. A. Varshalovich, and A. D. Kaminker, Pis'ma Astron. Zh. **24**, 488 (1998) [Astron. Lett. **24**, 418 (1998)].

24. A. I. Ryabinkov, A. D. Kaminker, and D. A. Varshalovich, Gravitation and Cosmology, Suppl., *Proceedings of the "Cosmion-96" and "Cosmion-97,"* Ed. by M. Yu. Khlopov *et al.* (Russian Grav. Soc., Moscow, 1999), Part II, p. 72.

25. P. D. Sisterna and H. Vucetich, Phys. Rev. Lett. **72**, 454 (1994).

Translated by V. Astakhov

Photometric Observations of Galaxy Clusters from a New X-ray Survey

R. A. Burenin*, A. A. Vikhlinin, and M. N. Pavlinsky

Space Research Institute, Russian Academy of Sciences, Profsoyuznaya ul. 84/32, Moscow, 117810 Russia
Received April 19, 2001

Abstract—We present the first results of our photometric observations of galaxy clusters from a new ROSAT X-ray survey of clusters. The observations were begun in the fall of 2000 with the 1.5-m telescope (AZT-22) that recently became operational at TUBITAK National Observatory (Turkey). The first series of observations was carried out in September–November 2000. Magnitudes of the brightest galaxies were measured for seven clusters, and photometric estimates of their redshifts were obtained. These first observations show that the necessary photometry for most galaxy clusters from the X-ray survey can be performed even during this year. © 2001 MAIK "Nauka/Interperiodica".

Key words: *galaxy clusters, photometric observations*

INTRODUCTION

Measuring various characteristics of galaxy clusters and studying their evolution with redshift are among the most important tools of observational cosmology. In particular, the shape and evolution of the cluster mass function strongly depend on the cosmological parameters Ω and Λ as well as on the initial perturbation spectrum, making it possible to determine these parameters from cluster observations (see, e.g., Eke *et al.* 1998; Mathiesen and Evrard 1998; Viana and Liddle 1999). Such studies require large, complete, and homogeneous samples of clusters suitable for a statistical analysis.

The new X-ray survey of bright distant galaxy clusters is an extension of the survey by Vikhlinin *et al.* (1998; below referred to as 160D). It is aimed at producing a sample of clusters suitable for studying the evolution of the luminosity function for clusters of galaxies with a high X-ray luminosity ($L_{44} > 3$, where L_{44} is the 0.5–2 keV luminosity in units of 10^{44} erg s^{-1}). At present, the evolution of such clusters is poorly understood in terms of existing surveys because of their small area covered or low sensitivity (Stocke *et al.* 1991; Rosati *et al.* 1998; Jones *et al.* 1998; Ebeling *et al.* 2000). At the same time, the evolution of precisely these clusters is most sensitive to changes in cosmological parameters, because they are richest and most massive.

Just as in the 160D survey, clusters were distinguished in our new survey by the property of their X-ray sources being extended. In our search for clusters, we used central fields, 17′.5 in radius, of more than 1800 pointings of the ROSAT telescope with a position-sensitive proportional counter (PSPC) in its focal plane. The preliminary reduction of the X-ray data was performed by Burenin and Vikhlinin (2000). The area covered by the survey is more than 400 square degrees, i.e., ~1% of the total sky area; it is limited to clusters with fluxes above 10^{-13} erg s^{-1} cm^{-2}, corresponding to clusters with luminosity $L_{44} \gtrsim 3$ located at $z \lesssim 0.8$[1]. The survey has revealed more than 400 extended sources with fluxes above the specified limit. Experience of the 160D survey and Monte Carlo simulations (Burenin and Vikhlenin 2000) show that the overwhelming majority of these sources are genuine clusters and that the sample is complete. Thus, this is the largest (in size), complete and homogeneous sample of galaxy clusters to date.

Using digital sky survey (DSS) photographic plates and various catalogs of extragalactic sources, we made a preliminary optical identification of the extended sources detected in our survey. Its results are summarized in Table 1. Since the clusters without optical identifications are most likely distant, galaxies from these clusters are faint and unseen in the photographic plates used. Further optical observations are required to identify these clusters.

To measure the distances to clusters from our survey, also requires optical observations. A simple, although rough, estimate of the distances to galaxy clusters can be obtained from photometric measurements. This estimate uses the fact that the absolute magnitudes of the

---

[1] All fluxes are given in the range 0.5–2 keV. In our calculations of cluster luminosities and radii, we took the Hubble constant $H_0 = 50$ km s^{-1} Mpc^{-1} and the acceleration parameter $q_0 = 0.5$.

* E-mail address for contacts: br@hea.iki.rssi.ru

Table 1. Optical identifications of clusters

Flux, 10^{-13} erg s^{-1} cm^{-2}	>1	>2
Number of objects	424	234
Clusters identified	312	195
Nearby galaxies	15	9
Previously known clusters	219	139
Clusters from 160D	139	76
Clusters with measured z	193	120

brightest cluster galaxies M_{BCG} differ only slightly. The scatter of absolute magnitudes is $\sigma_M \approx 0.3$ (Sandage 1972). Taking into account the correlation between the brightest galaxy's absolute magnitude and the cluster X-ray luminosity (Ebeling *et al.* 1997) significantly reduces the scatter in cluster distance determinations. The m_{BCG}–redshift relation corrected for the luminosity for distant clusters was calibrated by using the 160D catalog of clusters (Vikhlinin *et al.* 1998; see below). At the first stage, we plan to use this calibration to obtain photometric redshift estimates for the clusters from our survey.

To obtain an acceptable photometric estimate for the cluster redshift, the magnitude of the brightest cluster galaxy must be measured with an accuracy no lower than $\Delta m \approx 0.1$; in this case, the measurement error will be definitely smaller than the scatter of galaxy magnitudes about the m_{BCG}–z relation. First, we plan to observe clusters with X-ray fluxes above 2×10^{-13} erg s^{-1} cm^{-2}. This corresponds to a cluster with the luminosity $L_{44} = 3$ located at $z \approx 0.6$ or to a cluster with $L_{44} = 10$ at $z \approx 1.1$.

In order the measurement error be necessarily smaller than the scatter of galaxy magnitudes about the m_{BCG}–z relation, it will suffice to measure the magnitude of the brightness cluster galaxy with an accuracy no lower than $\Delta m \approx 0.1$. We primarily plan to observe clusters with the X-ray fluxes higher than 2×10^{-13} erg s^{-1} cm^{-2}, which corresponds to a cluster with luminosity $L_{44} = 3$ at $z \approx 0.6$ or to a cluster with $L_{44} = 10$ at $z \approx 1.1$.

OBSERVATIONS

The observations were carried out with a SBIG ST-8E CCD array mounted at the telescope's 1 : 8 Cassegrain focus. This CCD has 1530×1020 pixels with a pixel size of 9×9 μm. We used 2×2 binning, with each pixel of the images obtained having an angular size of $0''3 \times 0''3$. The CCD is cooled by a Peltier element to a temperature lower than the ambient temperature by $-25°$. It is equipped with a block of replaceable filters corresponding to the *UBVRI* bands of the Johnson–Morgan standard photometric system.

Compared to nitrogen-cooled CCDs, the ST-8E CCD has a noticeable dark current that must be taken into account. In addition, as usual, we subtracted a

median bias frame from the images and divided them by flat fields taken at dusk and dawn. Subsequently, all frames were corrected for bad points and strong cosmic rays. The images were reduced mainly with the standard IRAF (Image Reduction and Analysis Facility) package[2].

Currently, the telescope's drive is not working smoothly enough; the error reaches $1''$ in several minutes of exposure time. To obtain high-quality cluster images, we had to break down the total exposure into separate 30-s-long frames. After reducing each frame separately, we added them up with the offset determined from maximum cross-correlation. As a result, the quality of cluster images was very high, on average, $\sim 1''$ (see Table 2). However, in order that the frames were deep enough, we had to slightly increase the total exposure time. At a 20-min-long exposure, limiting magnitudes of fainter than 21^m were reached in R images.

To calibrate the cluster observations photometrically, we observed standard stars from the catalog of Landolt (1992) several times during each night. The reduction of star images was similar to that of cluster images, except that the total exposure times in this case did not exceed 30 s and there was no need to break them down into individual frames. We constructed a photometric solution for each night from these observations and used it to determine the magnitudes in the standard Johnson–Kron–Cousins system (Landolt 1992). This photometric system was used to calibrate the m_{BCG}–z relation for clusters from the 160D catalog, which will be used to estimate the cluster redshifts. Therefore, there should be no systematic differences between our photometric measurements and the measurements during the 160D survey. This will be checked by direct observations of clusters from the 160D survey, which were included in the program of observations with the AZT-22 telescope in April–May 2001.

The photometric solutions were corrected for color and for atmospheric extinction, which is determined by the air mass at a given zenith distance. Since an insufficient number of standard stars were observed on some of the nights, the color correction was calibrated separately for all the photometric nights taken together. This can be done, because the color correction is determined mainly by the CCD array and by the filter used and does not depend on the state atmosphere. The observations of standard stars showed that two of the eight nights were not photometric; there were apparently cirrus clouds in the sky.

The observations of the Baade IV standard field (Baade and Swope 1963) performed on one of the photometric nights concurrently with the cluster observations (October 24, 2000) confirm that the measured magnitudes are correct. Figure 1 shows the differences between the actual V magnitudes of some stars from this field and the V magnitudes measured during our

[2] http://tucana.tuc.noao.edu

Table 2. Observations of the clusters

Cluster designation	Resolution	Flux	m_R	m_V	m_B	m'	z_{phot}	L_{44}
2138–1431	1.1″	2.53	–	–	–	–	–	–
2323+1811	1.0	4.65	16.26	–	18.81	16.01	0.12	0.30
0029+1330	0.9	2.90	17.2*	–	–	17.1*	0.19*	0.5*
0106+3209	0.9	4.23	16.2*	–	18.4*	15.9*	0.12*	0.3*
0116–0330	0.9	2.94	15.87	–	18.06	15.40	0.09	0.11
0322–1338	1.3	2.01	18.40	19.44	–	18.38	0.32	0.93
0338–1111	1.6	5.05	16.51	–	18.90	16.33	0.14	0.43
0446–0421	1.1	7.16	16.73	–	19.24	16.69	0.16	0.83

observations. The Baade IV field was imaged with a total exposure time of 10 min, which was broken down into 30-s-long frames and reduced in the same way as the cluster images. To transform the instrumental magnitudes to the photometric system chosen, we used the same photometric solutions as for the magnitudes of cluster galaxies. The figure shows that the accuracy of our photometry is considerably higher than the required level ($\Delta m < 0.1$).

RESULTS OF CLUSTER OBSERVATIONS

In the first series, we managed to observe eight clusters with X-ray fluxes higher than 2×10^{-13} erg s^{-1} cm^{-2}. Basic data on these observations are given in Table 2. It contains the resolution obtained in the cluster image (full width at half maximum of the response to a point source). As was already said above, the images were of high quality in most cases. Only for the cluster 0338–1111 was the resolution lower than 1″.5. This deterioration of image quality was associated with the atmospheric state on this night. The X-ray fluxes are given in the table in units of 10^{-13} erg s^{-1} cm^{-2}. The table also lists the magnitudes of the brightest cluster galaxies measured in *BVR* through a fixed 4″ aperture (the m_{BCG}–z relation was calibrated precisely for the magnitudes through this aperture; see below). No magnitudes are given in the table for the extended source 2138-1431, because we failed to unambiguously identify it with a galaxy cluster using our images. In the remaining cases, the magnitude is not given in one of the bands, if no observations were carried out in this band. The magnitudes obtained on nonphotometric nights (the clusters 0029+1330 and 0106+3209) are marked by asterisks. The observations for these clusters should be repeated.

As was already said above, the m_{BCG}–z relation corrected for the luminosities of distant galaxies was calibrated by using the 160D catalog of clusters (Vikhlinin *et al.* 1998). This relation was calibrated in such a way that the magnitudes through the fixed 4″ aperture could also be used without the K-correction being applied. Since these dependencies are monotonic and moderately strong, they were included in the fitting of data by

the law of cosmological decrease in magnitudes with redshift, $m' = m_0 + 5\log z + 1.086(q_0 - 1)z$, with $m_0 = 20.45$ and some effective acceleration parameter, $q_0 = -0.121$. Here, m' is the magnitude of the brightest cluster galaxy corrected for the cluster luminosity using the formula $m' = m_R + 0.5\log L_{44}$. According to this calibration, the error in the photometric estimate of the redshift was $^{+0.04}_{-0.07}$. Table 2 gives magnitudes m', photometric estimates for the cluster redshifts z_{phot}, and cluster luminosities L_{44} corresponding to these estimates. There is no cluster with a measured redshift among these clusters. David *et al.* (1999) gave a photometric estimate of the redshift for the cluster 0338–1111, $z_{phot} = 0.18$, obtained by the standard method from the magnitude of the tenth brightest cluster galaxy. The difference between this estimate and our value is within the error limits of the methods.

As we see from Table 2, all the clusters observed in September–November 2000 are comparatively close and have X-ray luminosities typical of poor clusters or groups of galaxies. Only two clusters, 0322–1338 and 0446–0421, have luminosities $L_{44} \sim 1$. Figures 2 and 3 show AZT-22 images of the central regions in these clusters. The exposure times were 20 and 15 min,
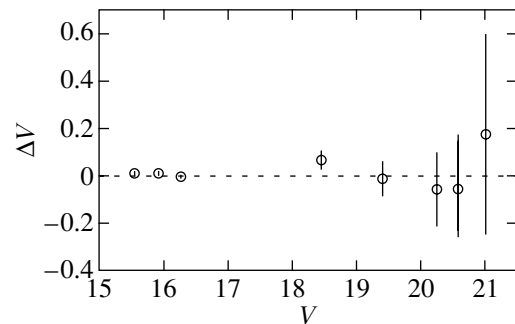

Fig. 1. Differences between the actual *V* magnitudes of some stars from the Baade IV field and the measured *V* magnitudes.
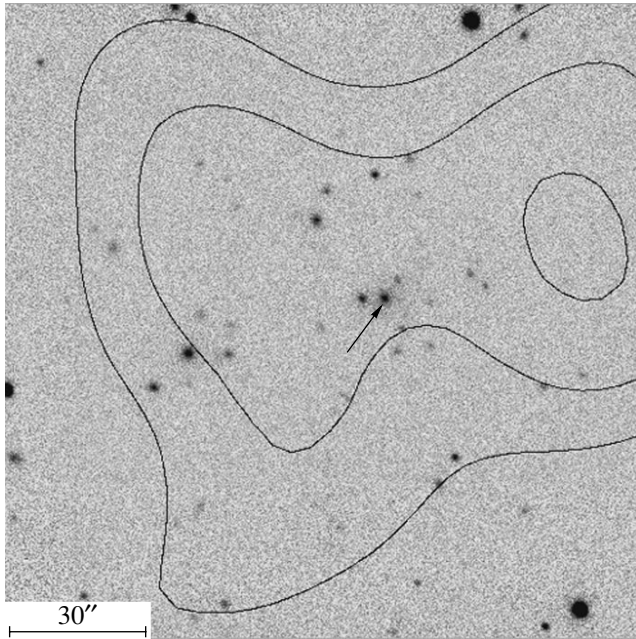
Fig. 2. The image of the central region in the cluster 0322–1338 obtained with an exposure time of 20 min. The angular scale is shown, and the arrow indicates the brightest cluster galaxy. Also shown are ROSAT X-ray isophotes.
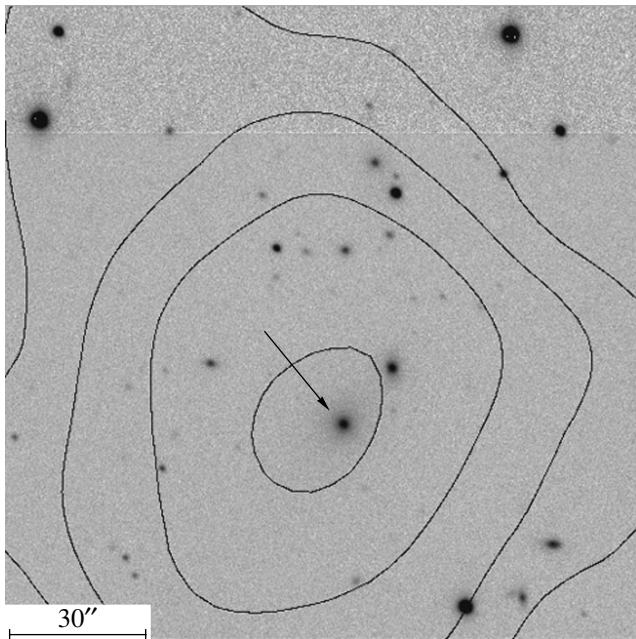

Fig. 3. The image of the central region in the cluster 0446–0421 obtained with an exposure time of 15 min.

respectively. The angular scale is shown in the figures and the arrow mark the brightest cluster galaxy whose magnitude is given in Table 2. The contours represent ROSAT X-ray isophotes.

CONCLUSION

We have presented our photometric observations of eight galaxy clusters from the new X-ray survey using the Russian 1.5-m AZT-22 telescope installed at TUBITAK Observatory (Turkey). We obtained high-quality images of the clusters' central regions and measured, with the required accuracy, the magnitudes of the brightest cluster galaxies, which yielded photometric estimates for the cluster redshifts.

The quality of our images proved to be high. The FWHM of the response to a point source was ~$1''$ in most cases. As was said above, in order to allow for the drive errors, we had to break down the total exposure into 30-s-long frames. Since the bulk of the noise arises when an image is read out from the CCD, we had to significantly increase the exposure time to obtain sufficiently deep images. For example, to obtain an image with a limiting magnitude >21^m requires an exposure time of about 20 min or longer, instead of approximately 5 min. that would be required if there were no drive errors. After this error is removed, the observing time will be used much more efficiently.

The clusters from our survey are uniformly distributed in the sky at high Galactic latitudes, so most clusters from our survey should be observed during late winter–early summer. These observations were included in the telescope's observing program. Based on the observations presented here, we optimized the observing technique. Our observations show that, despite the drive error of the telescope, most of our observing program can be performed by the mid-summer of 2001. These data will be used for a preliminary study of the evolution for clusters with high X-ray luminosities. In addition, these data will also allow a program of spectroscopic cluster observations to be started.

REFERENCES

1. Z. Aslan, I. F. Bikmaev, É. A. Vitrichenko, *et al.*, Pis'ma Astron. Zh. **27**, 464 (2001) [Astron. Lett. **27**, 398 (2001)].

2. W. Baade and H. H. Swope, Astron. J. **68**, 435 (1963).

3. R. A. Burenin and A. A. Vikhlinin, Preprint No. Pr-2029, IKI RAN (Space Research Inst., Russian Academy of Sciences, 2000).

4. L. P. David, W. Forman, and C. Jones, Astrophys. J. **519**, 533 (1999).

5. H. Ebeling, A. C. Edge, A. C. Fabian, *et al.*, Astrophys. J. Lett. **479**, L101 (1997).

6. H. Ebeling, A. C. Edge, S. W. Allen, *et al.*, Mon. Not. R. Astron. Soc. **318**, 333 (2000).

7. V. R. Eke, S. F. Cole, S. Carlos, and P. J. Henry, Mon. Not. R. Astron. Soc. **298**, 1145 (1998).

8. L. R. Jones, C. Scharf, H. Ebeling, *et al.*, Astrophys. J. **495**, 100 (1998).

9. A. U. Landolt, Astron. J. **104**, 340 (1992).

10. B. Mathiesen and A. E. Evrard, Mon. Not. R. Astron. Soc. **295**, 769 (1998).

11. P. Rosati, R. della Ceca, C. Norman, and R. Giacconi, Astrophys. J. Lett. **492**, L21 (1998).

12. A. Sandage, Astrophys. J. **173**, 495 (1972).

13. J. T. Stocke, S. L. Morris, I. M. Gioia, *et al.*, Astrophys. J. Suppl. Ser. **76**, 813 (1991).

14. P. T. P. Viana and A. R. Liddle, Mon. Not. R. Astron. Soc. **303**, 535 (1999).

15. A. A. Vikhlinin, B. R. McNamara, W. Forman, *et al.*, Astrophys. J. **502**, 558 (1998).

Translated by N. Samus'

Background-Field Effects in Astrometric Microlensing

V. I. Zhdanov*, S. A. Salata, and E. V. Fedorova**

Astronomical Observatory, Kiev State University, 252053 Ukraine

Received March 29, 2001

Abstract—We consider the motion of the image of a distant radiation source microlensed by one and many point masses in the presence of an external background field, which produces a shear in the lens equation. The trajectories of the image brightness centroid (BC) in a Chang-Refsdal lens are very sensitive to the magnitude of the shear and to the direction of motion of the microlenses, allowing these parameters to be unambiguously determined from the BC motion. Stochastic motions of the BC for an extended source are simulated in a problem with a large number of randomly arranged microlenses. We derive dependences of the root-mean-square variations in BC velocity on microlens density, on external shear, and on the continuous component of the mass density, which may be related to dark matter in extragalactic lenses. © *2001 MAIK "Nauka/Interperiodica"*.

Key words: *gravitational lenses, astrometric microlensing, dark matter*

1. INTRODUCTION

For several years, gravitational lenses have been attracting attention as a unique tool for obtaining astrophysical data. Individual lines of research in this field have to do with the near microlensing of distant sources by massive compact objects in our Galaxy; the potentialities of extragalactic gravitational-lens systems (GLSs) both in microlensing and in producing macroimages are far from being completely unveiled (see, e.g., Zakharov 1997; Wambganss 1998; Claeskens and Surdej 2000). In recent years, the prospects for microarcsecond astrometry have aroused interest in position displacements of microlensed images (Hog *et al.* 1995; Paczynski 1998). It is easier to record microarcsecond displacements in the average brightness centroid (BC) of a microlensed image than to separate it into individual microimages. Astrometric effects are expected to become observable with the space interferometer that is being developed (Paczynski 1998).

The position displacements of microlensed images are produced by the same general-relativity effects as microlensing brightness variations. However, these displacements do not decrease so rapidly as brightness effects with angular distance from the source to the lens, and they are less noisy because of intrinsic brightness variations of the quasar in GLS. Therefore, when the required positioning accuracy is achieved, observations of the BC trajectories in GLSs can successfully complement the conventional light-curve monitoring. Theoretical questions of such astromeric microlensing were touched upon in application to both our Galaxy and extragalactic GLSs (see, e.g., Hog *et al.* 1995; Williams and Saha 1995; Paczynski 1998; Lewis and Ibata 1998; Zhdanov and Salata 1998).

When microlensing effects are modeled, the background gravitational-field component, which is produced by masses far from the line of sight and varies slowly both on spatial scales of the order of the microlens size and with time, is usually isolated. Thus, the average field of the entire lensing galaxy on the line of sight is taken into account in extragalactic systems. This component determines a shear matrix, which is one of the main elements in the lens equation. An analysis of shear effects is of interest in estimating the background field and in constructing GLS models (Schneider *et al.* 1992; Wambsganss 1998; Claeskens and Surdej 2000). In the case of microlensing by stars in our own Galaxy, the background field can be produced by a companion of a binary or by the nearest stars on the line of sight.

In this paper, we consider the shear effects on the trajectories described by the BC of microlensed images. First, we analyze the case of a low optical density for strong and weak microlensing by individual masses, where these effects show up most clearly. Subsequently, we present the results of statistically modeling the BC motions of an extended source microlensed by a large number of point masses. We discuss the possibility of determining the shear and the continuous component of mass surface density using data on BC motions.

2. GENERAL RELATIONS

Gravitational-lens models, whose parameters can be determined by taking into account the visible macroimage configuration as well as the brightness distribution and stellar velocity dispersion in the lensing galaxy,

---

*, ** E-mail addresses for contacts: Zhdanov@observ.univ.kiev.ua
Elena-f@mail.univ.kiev.ua

allow, with known reservations, the local shear γ and optical density of the total mass $\sigma = \sigma_m + \sigma_c$ in the vicinity of each image to be calculated (Schneider *et al.* 1992; Wambsganss 1998; Claeskens and Surdej 2000). Here, σ_m is the optical density of microlensing stars, and σ_c describes the continuous component of optical depth of the mass in the lens equation. The fraction of σ_c in the total density and its origin are currently unknown; its estimation is an important element of gravitational-lens studies.

The basic equation that described the microlensing of a distance object by N identical point masses can be reduced to (Schneider *et al.* 1992)

$$
\begin{aligned}
\mathbf{y} &= \mathbf{A}\mathbf{x} - \sum_{g=1}^{N} \frac{R_E^2(\mathbf{x} - \mathbf{x}_g)}{|\mathbf{x} - \mathbf{x}_g|^2}, \\
\mathbf{A} &= \left\| \begin{matrix} 1 - \gamma - \sigma_c & 0 \\ 0 & 1 + \gamma - \sigma_c \end{matrix} \right\|.
\end{aligned}
\tag{1}
$$

This equation relates the angular position $\mathbf{x}$ of the image of an object's point on a unit sphere to its undistorted position $\mathbf{y}$; $\mathbf{x}_g$ are the angular positions of the point microlenses ($g = 1, 2, \ldots, N$) of equal mass M; $R_E^2 = 4GMD_{GS}/(D_S D_G)$ is the angular radius of the Einstein ring in the absence of a background field; D_G, D_S, and D_{GS} are the distances (in angular diameter) to the masses, to the source, from the masses to the source, respectively; the direction of the coordinate axes coincide with the principal directions of shear matrix $\mathbf{A}$, in accordance with Eq. (1).

To determine the position of the brightness centroid for an extended source, we must add up the contributions from all images of each of its point with a weight proportional to the brightness. Passing from integration over the source's $\mathbf{y}$ coordinate to integration over the $\mathbf{x}$ coordinate, we can represent the result as (Zhdanov and Salata 1998)

$$
\Delta \mathbf{y} = \mathbf{y}_c - \mathbf{y}_{c0} = \frac{\int \mathbf{x} \cdot B(\mathbf{y}(\mathbf{x})) d^2 x}{\int B(\mathbf{y}(\mathbf{x'})) d^2 x'},
\tag{2}
$$

where $\mathbf{y}_{c0} = 0$ is the undistorted BC placed at the coordinate origin, and $\mathbf{y}_c$ is the image BC of the microlensed source; the integration is performed over the entire image region.

3. A SPARSE SYSTEM OF MICROLENSES

For microlensing with a low optical density σ_m, we may consider individual events by using only one term [$N = 1$ in Eq. (1)] to describe them.

Let us first consider the case with $\sigma_c = 0$. At a low optical density, the typical distance between the lensing mass and the source is large, $|\mathbf{x} - \mathbf{x}_g| \gg R_E$. Assuming

that the source is at the coordinate origin $\mathbf{y} = 0$, we obtain the position of the main image from Eq. (1)

$$
\mathbf{x} = \mathbf{A}^{-1} \frac{R_E^2(\mathbf{x} - \mathbf{x}_g)}{|\mathbf{x} - \mathbf{x}_g|^2} \approx -\mathbf{A}^{-1} \frac{R_E^2 \mathbf{x}_g}{|\mathbf{x}_g|^2}.
\tag{3}
$$

Using elementary geometric considerations, it is easy to verify that for a rectilinear motion of the microlens in the source's rest frame (with position $\mathbf{x}_g$), the vector $R_E^2 \mathbf{x}_g / |\mathbf{x}_g|^2$ describes a circumference. The tangent to the circumference at the point corresponding to the source's unperturbed position (in the limit $\mathbf{x}_g \longrightarrow \infty$) is parallel to the lens velocity. Accordingly, the image of a point source $\mathbf{x}$ moves in an ellipse, to which the circumference deforms under the action of matrix $\mathbf{A}^{-1}$, irrespective of the direction of microlens motion. Thus, the shape of the image trajectory allows γ to be unambiguously determined. Then, if γ is known, we can obtain the original circumference by using an inverse coordinate deformation described by matrix $\mathbf{A}$; the direction of microlens motion can be easily determined using this circumference.

For a nonzero σ_c, Eq. (1) can be rewritten in a normalized form (see, e.g., Schneider *et al.* 1992), which is the same as that for $\sigma_c = 0$ but with modified shear γ_r and microlens optical density σ_{mr}:

$$
\gamma_r = \gamma/(1 - \sigma_c), \quad \sigma_{mr} = \sigma/(1 - \sigma_c).
$$

Here, we have a similar pattern of trajectories, from which the reduced γ_r and, if γ is known (for example, from the lens macromodel), σ_c can be determined.

In the more complex case of strong microlensing [Chang-Refsdal (1979) lens], one should take into account the contributions from all images and the finite size of the source, which can be comparable to R_E. In this case, we calculated the shear of the image BC directly from formula (2). However, here, there is also a portion where the approximation (3) holds ($|\mathbf{x}_g| \gg R_E$), whence it is clear that γ and the direction of motion can be determined in principle from the known BC trajectory. Of course, an efficient algorithm similar to least squares fitting must use the entire trajectory.

We calculated the BC trajectories at $|\mathbf{x}_g| \sim R_E$ for a source with a Gaussian brightness distribution

$$
B(\mathbf{y}) = B_0 \exp(-\mathbf{y}^2 / L^2)
\tag{4}
$$

and inertial lens motion. Examples are shown in Fig. 1 for $L = 0.1 R_E$ and $\sigma_c = 0$; in general, these trajectories have a complex multiloop pattern. The number of self-intersections depends both on the distance between the lens trajectory and the source and on the source size. Note that the brightness distribution changes when the lens is projected onto on the source disk, which affects the BC position and gives rise to loops at $\gamma = 0$ as well (Zhdanov and Salata 1998). The dependence on the direction of lens motion and on shear γ is clearly seen
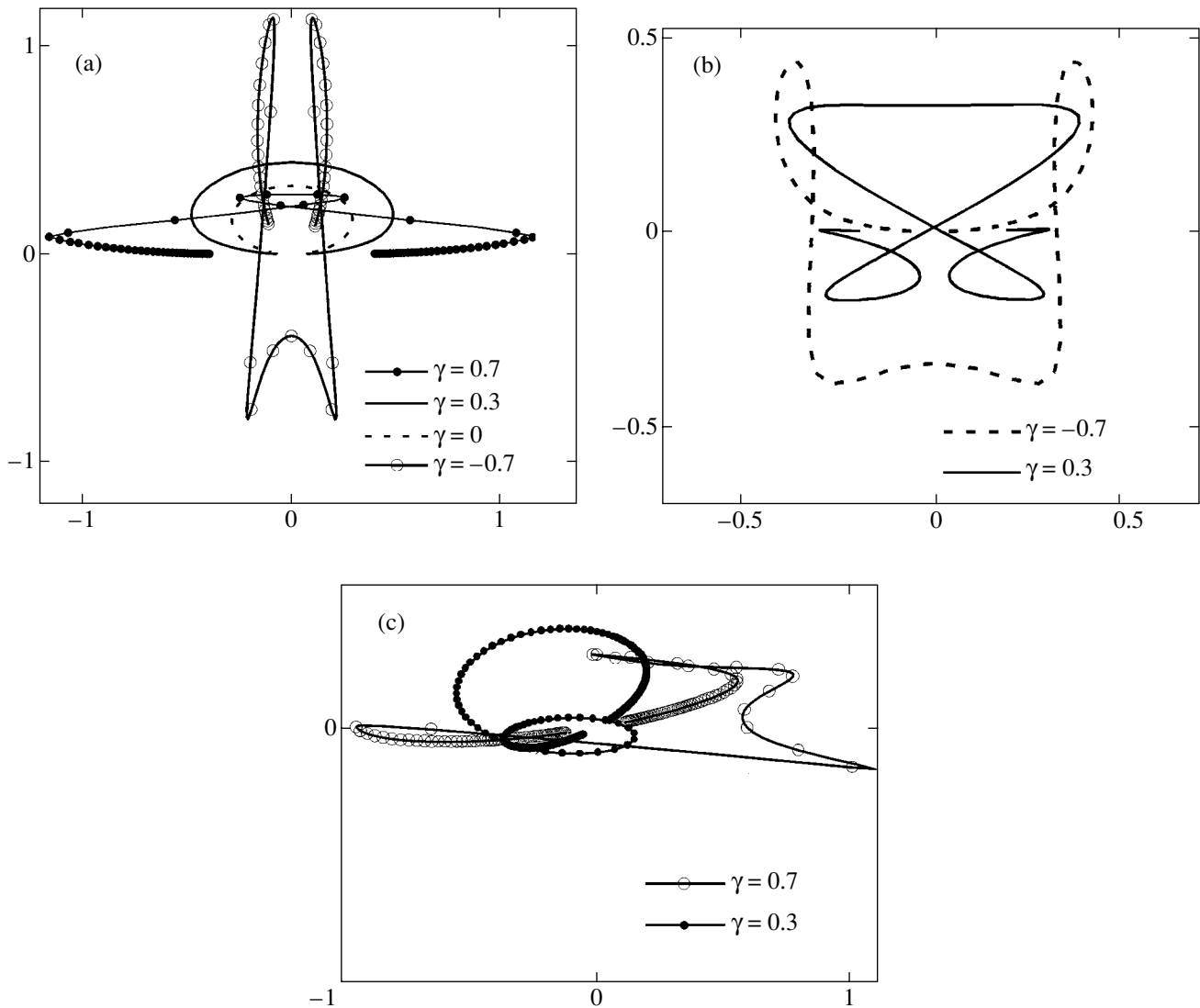
Fig. 1. Examples of the BC trajectories for a source image in a Chang-Refsdal lens for several values of shear γ in the coordinate system corresponding to angular variables $\mathbf{x} = \{x_1, x_2\}$ (x_1 and x_2 are the abscissa and ordinate, respectively; the choice of the scale corresponds to $R_E = 1$). The orientation of the coordinate system corresponds to the principal directions of the shear matrix in Eq. (1). The symbols on the trajectories mark equal time intervals while the microlens moves at constant velocity in a straight line $\mathbf{x}_g = \mathbf{p} + \mathbf{v}_g t$; $(\mathbf{vp}) = 0$, $\mathbf{p} = p_0\{\sin(\alpha), -\cos(\alpha)\}$; for (a) impact parameter $p_0 = 1$, $\alpha = 0$; (b) $p_0 = 0.2$, $\alpha = 0$; and (c) $p_0 = 1$, $\alpha = \pi/4$. The unperturbed BC is at rest at point $(0, 0)$; the brightness distribution is given by formula (4) for $L = 0.1$.

in Fig. 1 even from the qualitative appearance of the trajectories.

Of interest is the large BC displacement velocity as the lens passes at an angular distance of about R_E from the source when the latter is near the caustics produced by a weak external field. This is illustrated in Fig. 2, where the displacement of BC of various sizes is plotted against lens position in the limiting situation when the lens moves along the principal directions of the shear matrix along the x axis (with a zero impact parameter), so that source crosses the caustic kinks. The effect is strongest for a point source; this case can be easily analyzed by explicitly solving the lens equation. Here, if the shear γ is small, the change in BC position remains finite and equal to $\approx 2R_E$, but the caustic-

crossing time is short (proportional to $\sim \gamma R_E$); hence the almost jump-like BC displacement. As we see from Fig. 2, different signs of γ result in different signs of BC displacement. For a small source, as γ decreases, the displacement velocity is proportionally to $1/\gamma$ until the condition $L \ll \gamma R_E$ is violated. The jump is smoothed out with increasing source size. Note that the existence of jumplike motions for a double lens was previously noted by Han *et al.* (1999).

4. IMAGE MOTION FOR A LARGE NUMBER OF MICROLENSES

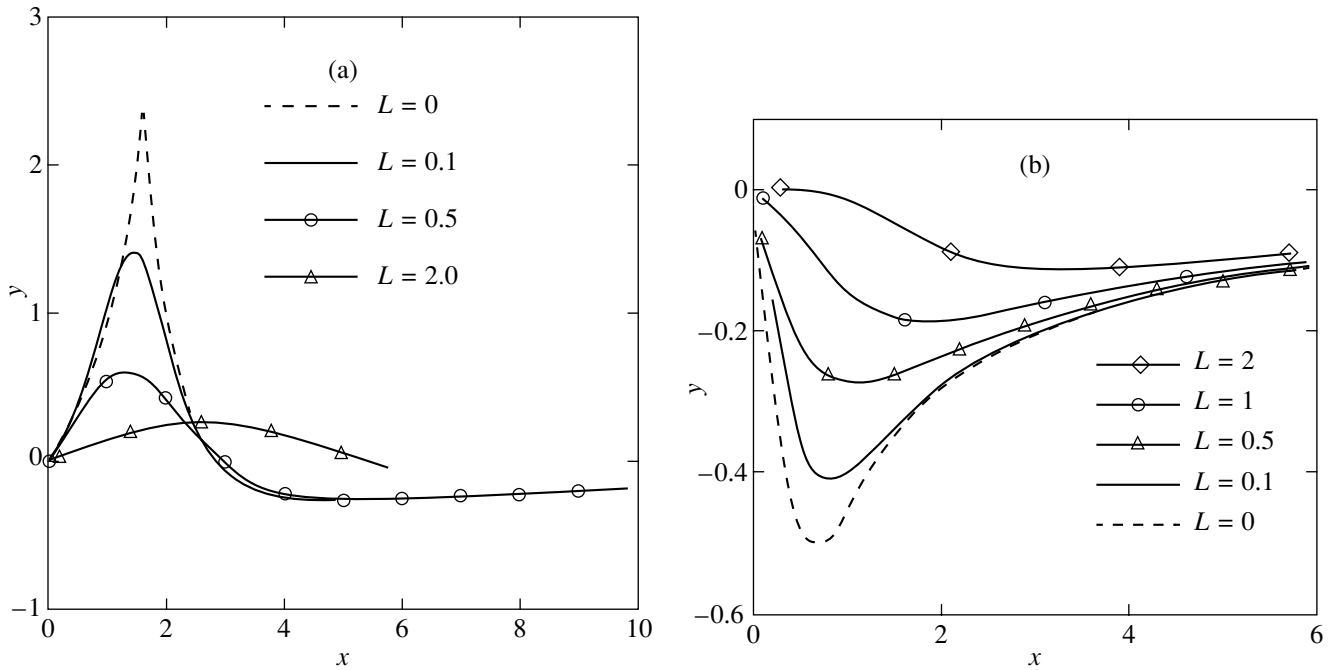For a large number of microlensing masses, the BC trajectory is generally intricate and the statistical esti-

Fig. 2. BC displacement Y versus position X of the source center on the x-axis relative to the lens for various source sizes L. The coordinate system is oriented along the principal directions of the shear matrix [see formula (1)]: (a) $\gamma = 0.5$ and (b) $\gamma = -0.5$.

mates become more appropriate. Below, we present Monte Carlo simulations of BC motions for the source's Gaussian brightness distribution (4) in the case where all lensing masses are equal and have the same velocity vector (motion of the lensing galaxy as a whole).

In these simulations, the long-range and boundary effects, which, in particular, are attributable to the dependence of mean BC displacement and mean velocity on the mass distribution far from the line of sight (Zhdanov and Zhdanova 1995; Zhdanov *et al.* 2000), prove to be significant. Here, we are interested in eliminating such effects in order to separate the contribution of local lens parameters. Therefore, instead of the BC displacements $\mathbf{y}(t)$, we analyzed the variations in velocity $\mathbf{V}(t) = \Delta\mathbf{y}(t)/\Delta t$ for random realizations of an ensemble of microlenses with a fixed microlens velocity:

$$\Delta\mathbf{V} = \mathbf{V} - \langle\mathbf{V}\rangle, \quad W_i = \langle(\Delta V_i)^2\rangle^{-1/2}, \quad (i = 1, 2),$$

where $i = 1,2$ correspond to the velocity projections onto the principal directions of shear matrix $\mathbf{A}$ in Eq. (1). In particular, W_1 is the rms deviation of the longitudinal BC velocity component relative to the shear; the mean velocity $\mathbf{V}$ in each realization was calculated from two values of $\Delta\mathbf{y}$ separated by $\Delta t/V_g$, V_g is the microlens velocity); the angular brackets $\langle...\rangle$ denote averaging over the set of all realizations of microlens positions. Clearly, the result depends on the interval Δt, which must correspond to observing conditions and should not be too long or very short. We restricted our calculations to $\Delta t = 0.3 R_E$.

In contrast to the BC displacements themselves, the rms velocity deviations W_i prove to be insensitive to the distribution of microlenses far from the line of sight. This allowed us to significantly reduce the size of the region where the microlens positions were generated when performing integration in (2) and, along with them, the number of microlenses included in Eq. (1). We chose the above size in such a way as to allow for the scattering of rays in microlensing based on the results of Katz *et al.* (1986) and numerically by checking the convergence. The series of computations contained up to 300 random realizations of microlens positions for parameters sufficiently far from the critical domain ($|\gamma| + \sigma_m + \sigma_c < 0.8$). Since the computational time rapidly increases with decreasing source size, we restricted our analysis to $L = 0.5 R_E$ and considered smaller sizes only for some realizations. For a small source ($L \ll R_E$), the numerical results should be reconsidered, but the main qualitative conclusions remain valid.

Our computations show that when there is no continuous component ($\sigma_c = 0$), W_i increase with microlense optical density $\sigma_m \in [0.1, 0.3]$ and at fixed $\gamma \in [-0.5, 0.5]$. For $\gamma \in [0.,0.5]$, the rms deviation of the velocity projection $W_1(\gamma)$ onto the shear direction increases with γ at $\sigma_m = $ const for all inclinations of the microlens velocity to the shear direction (i.e., to the V_1 axis) from $0°$ to $90°$. The behavior is apparently the same for negative $\gamma \in [-0.5, 0.]$, but here, the increase of $W_1(\gamma)$ is less noticeable, and the number of trials in statistical calculations should be increased for the conclusions to be
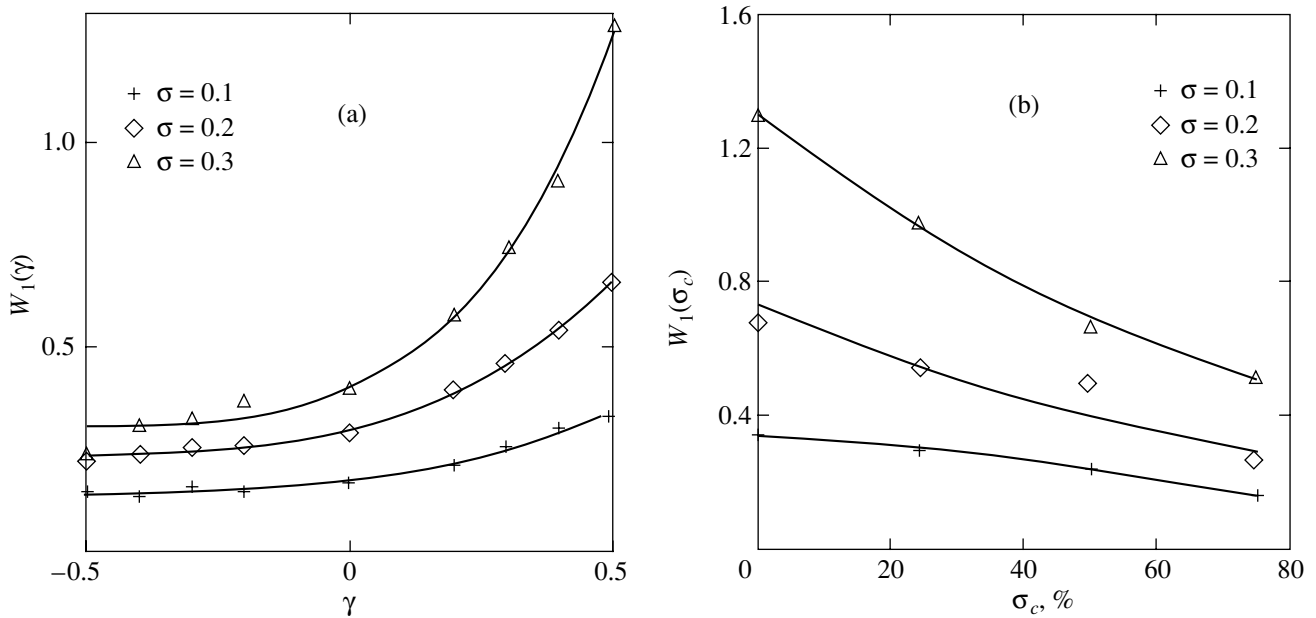
Fig. 3. Dependences $W_1(\gamma)$ for the optical densities $\sigma = \sigma_m = 0.1$, 0.2, and 0.3 ($\sigma_c = 0$); the source size is $L = 0.5$. The velocities are normalized to the microlens velocity, which is directed along the V_1 axis, i.e., along the shear direction (for $\gamma > 0$). The symbols represent the results of Monte Carlo simulations, and the solid curves represent the smoothed dependences. (a) Dependences $W_1(\sigma_c)$ for three total optical densities $\sigma = \sigma_m + \sigma_c$ (σ_c is in % of $\sigma = 0.1$, 0.2, and 0.3); $\gamma = 0.5$ and the source size is $L = 0.5$. The velocity normalization and the directions of microlens motion are similar to those in Figs. 3a, 3b.

completely reliable. Figure 3a shows the dependencies $W_1(\gamma)$ for three values of σ_m when the system of microlenses moves along the V_1 axis. Similar dependencies for the transverse component $W_2(\gamma)$ decrease and behave like $W_1(-\gamma)$, but they do not coincide with these dependencies. For a source with a size of the order of R_E and subcritical lens parameters, W_1 proves to be of the same order of magnitude as the velocity of the lensing galaxy. This situation is qualitatively similar to the shearless case (Zhdanov *et al.* 2000), but a nonzero γ can significantly increase W_1.

For $\sigma_c > 0$, it of interest to elucidate the pattern of variations in observed $W_i(\sigma_c)$ at fixed γ and $\sigma = \sigma_m + \sigma_c$, because it becomes possible to determine σ_c if γ and σ can be estimated independently. Examples of the dependencies are shown in Fig. 3b. Note that the decrease of $W_1(\sigma_c)$ in the plots of Fig. 3b mainly stems from the fact that the microlens density σ_c decreases with increasing σ_m.

5. DISCUSSION

As we see from our results, the background field of a gravitational lens significantly affects the shape of the BC trajectory. This gives hope that astrophysically interesting data can be obtained in the future by observing the BC displacements. When the source's impact parameter relative to one lens is comparable to R_E, the trajectory changes qualitatively with shear γ and lens orientation (see Fig. 1). At a nonzero density of continuous matter σ_c, the dependence of this parameter is

contained in the normalized shear $\gamma_r = \gamma/(1 - \sigma_c)$. If γ is known, for example, from the macroscopic lens model, this relation yields σ_c. An independent estimate of the contribution of continuous matter σ_c is of interest in extragalactic GLSs, where the structure of the matter that provides the line-of-sight optical density is unknown, and dark matter can comprise much of it. Various dark matter variants are discussed in the literature [see, e.g., the review by Bergstorm (2000)], which can correspond to compact or extended objects. The trajectories of microlensed images contain information about the relative fraction of the discrete component of the surface matter density formed by compact objects and the continuous component of this density with a comparatively large spatial scale.

Here, the model of a single lens with a background field is only of qualitative interest. At the same time, we cannot rule out the possibility of GLSs in which continuous matter mainly contributes to the surface mass density and the density of microlenses is low. In this case, the model of a single lens can be justifiably used to describe single microlensing events, which, however, are unlikely here. However, even in such a single event, we can determine the direction of lens motion and the shear (section 3).

In a more general case, the image motion will be simultaneously affected by the fields of many microlenses, and the local parameters of the lens can be determined statistically (section 4). Let us assume, for example, that the orientation and magnitude of the shear γ, the optical density σ of the total mass near each macro-

image, and the source size are known. Then, the unknown quantities to be determined are the galaxy velocity V_{gal}, the optical density σ_c of continuous matter, and the angle between the galaxy velocity and the shear direction. We assume that σ_c changes little for different lens macroimages near the center of the lensing galaxy, which are located usually at a distance of the order of several arcseconds. In this case, by analyzing dependencies similar to those shown in Fig. 3b for two images, we obtain two conditions for the above parameters. An additional relation for V_{gal}, which must be considered together with the above constraints, can be derived by analyzing the frequency of high magnification microlensing events. An analysis of such events allows the product $V_{gal}\sqrt{\sigma_m}$ to be estimated (see, e.g., Wyithe *et al.* 2000b). These three jointly considered relations allow the three sough-for parameters to be determined.

The Einstein cross Q2237+030 seems to be the most promising extragalactic object for analyzing astrometric effects during microlensing. Here, the BC displacements can reach 10^{-5} arcsec, although considerably larger displacements are possible in some situations (Williams and Saha 1995; Lewis and Ibata 1998). For this object, a detailed model of the mass distribution in the macrolens was developed (Schmidt *et al.* 1998), allowing γ and the orientation of the principal axes of the shear matrix to be independently estimated.

In Section 4, we assumed that the stellar velocities in the lensing galaxy could be disregarded; i.e., all stars were assumed to move identically. A more consistent approach must take into account the velocity distribution, whose role can be estimated, for example, by using photometric monitoring (Wyithe *et al.* 2000a). The source size should also be taken into account, which, for example, significantly differs in the quasar continuum and in the region of broad emission lines. The plots in Fig. 3 show that the image BC displacement for a source of small size can be several-fold larger than that for sizes of the order of R_E. Therefore, for specific systems, the results of section 4 should be recalculated with allowance for the source size in different spectral ranges. As we see from the aforesaid, determining the line-of-sight lens parameters from astrometric data seems difficult although possible in principle.

In conclusion, note that the results of section 3 are applicable in part to the microlensing of stars in nearby galaxies by binaries of our Galaxy. Although such events are relatively rare, they have already been recorded (MACHO-98-SMC-1; MACHO 97-BLG-28). The presence of caustics in such systems allows the brightness distribution of the lensed source to be analyzed with a high angular resolution (Bogdanov and Cherepashchuk 2000). The Chang-Refsdal (1979) model is applicable here if one of the binary components is far enough. The characteristic angular displacement during the microlensing of a distant source by a Galactic star of mass M at distance D is described by the parameter $R_E = 0.9 \times 10^{-3}(M/M_\odot)^{1/2}$ $(10\ kpc/D)^{1/2}$ arcsec. The shear produced by mass M_1 (a companion star or a massive star) at distance R from mass M is of the order of $|\gamma| \sim (M_1/M_\odot)\ (10\ AU/R)^2$. In this case, the applicability condition for the background field model is $|\gamma| \ll 1$; it is satisfied either for a low mass M_1 or for a sufficiently large separation between the companions. The jump-like image motion is most pronounced when the source size is considerably smaller than the caustic size. This yields the necessary condition $|\gamma| \gg 10^{-6}$ for the microlensing of stars in nearby galaxies located at a distance of ~1 Mpc. The characteristic BC displacement at small γ remains the same ($\sim R_E$), but the probability that the source falls within the caustic region decreases proportionally to γ^2.

REFERENCES

1. L. Bergstrom, Rep. Prog. Phys. **63**, 793 (2000); hep-ph/0002126.
2. M. B. Bogdanov and A. M. Cherepashchuk, Astron. Zh. **77** (11), 842 (2000) [Astron. Rep. **44**, 745 (2000)].
3. K. Chang and S. Refsdal, Nature **282**, 561 (1979).
4. J.-F. Claeskens and J. Surdej, Astron. Astrophys. Rev. (2001) (in press).
5. C. Han, M.-S. Chun, and K. Chang, Astrophys. J. **526**, 405 (1999).
6. E. Hog, I. D. Novikov, and A. G. Polnarev, Astron. Astrophys. **294**, 287 (1995).
7. N. Katz, S. Balbus, and B. Paczynski, Astrophys. J. **306**, 2 (1986).
8. G. F. Lewis and R. A. Ibata, Astrophys. J. **501**, 478 (1998).
9. B. Paczynski, Astrophys. J. Lett. **494**, L23 (1998).
10. R. Schmidt, R. L. Webster, and G. F. Lewis, Mon. Not. R. Astron. Soc. **295**, 488 (1998).
11. P. Schneider, J. Ehlers, and E. E. Falco, in *Gravitational Lenses* (Springer-Verlag, New York, 1992).
12. J. Wambsganss, *Living Reviews in Relativity* (1998), Vol. 1 (http://www.livingreviews.org/Articles/Volumel/1998-12wamb).
13. L. L. R. Williams and P. Saha, Astron. J. **110**, 1471 (1995).
14. B. Wyithe, R. L. Webster, and E. L. Turner, Mon. Not. R. Astron. Soc. **309**, 261 (2000a).
15. B. Wyithe, R. L. Webster, and E. L. Turner, Mon. Not. R. Astron. Soc. **315**, 337 (2000b).
16. A. F. Zakharov, *Gravitational Lenses and Microlenses* (Yanus, Moscow, 1997).
17. V. I. Zhdanov and S. A. Salata, Kinematika Fiz. Nebesnykh Tel **14**, 203 (1998).
18. V. I. Zhdanov and V. V. Zhdanova, Astron. Astrophys. **299**, 321 (1995).
19. V. I. Zhdanov, A. N. Aleksandrov, and S. A. Salata, Kinematika Fiz. Nebesnykh Tel **16**, 336 (2000).

Translated by A. Dambis

Interaction of a Nonstationary Ionization-Shock Front with an Inhomogeneous Interstellar Medium

K. V. Krasnobaev*

Moscow State University, Vorob'evy gory, Moscow, 119899 Russia
Received March 22, 2001

Abstract—We consider the interaction of an ionization-shock front with isothermal waves in an H I region. Based on a two-front model in the linear approximation, we have detected a significant (approximately by an order of magnitude) periodic amplification of perturbations as they penetrate from the interstellar medium into an H II region. Numerical simulations have revealed that even when the shock- and ionization-front velocities differ and the relative density perturbations in the interstellar medium are $\sim 10^{-1}$, the variations in gas parameters near the ionization front are comparable to those observed at the boundaries of H II regions. © *2001 MAIK "Nauka/Interperiodica".*

Key words: *interstellar medium, shock waves, ionization fronts, instabilities, H II regions*

INTRODUCTION

Among the mechanisms for the enhancement and generation of inhomogeneities in the interstellar medium, those attributable to the instability of radiative shock waves occupy an important place (Langer *et al.* 1981; Chevalier and Imamura 1982; Imamura *et al.* 1984; Wolf *et al.* 1989; Strickland and Blondin 1995; Walder and Follini 1996; Kimoto and Chernoff 1997; Krasnobaev 2001). The growth of instability and the emergence of oscillations in gas parameters are physically caused by a decrease in the cooling rate (per unit mass) at the compression phase, as is the case in a thermally unstable medium (Krasnobaev and Tarev 1987). To a certain degree, there is also an analogy with the behavior of shock waves during thermonuclear supernova explosions (Koldoba *et al.* 1994; Blinnikov 1996; Imshennik *et al.* 1999). For these explosions, the additional energy release in the growing oscillations in the burning zone adjacent to the shock front is clearly inconsistent with the stationary structure of the detonation front.

Apart from the problems associated with an accurate allowance for radiative heating and cooling of the medium, an investigation of the dynamics of radiative shock waves is often complicated by a system of discontinuities of various types. In particular, when H II regions expand, the shock wave is followed by an ionization front (I front), which significantly affects the shock oscillation spectrum and amplitude (Krasnobaev 2001). However, we obtained this result under the assumption of a homogeneous interstellar medium and equal shock- and ionization-front velocities.

However, as an H II region evolves, the shock wave leads the ionization front, and the separation between discontinuities increases with time; i.e., the ionization-shock front (or I-S front) is nonstationary. As a result, the conditions under which the amplification of shock oscillations is largest generally change. Thus, the need for a quantitative analysis of the nonstationarity effect arises.

The influence of small inhomogeneities in the interstellar medium on the propagation of the I-S front is of interest, in particular, for the following reason.

It is well known from observations that the level of density, velocity, and temperature fluctuations in the medium at the boundary of an H II region can be considerably higher than in the neutral gas through which the shock wave preceding the ionization front propagates. Having performed a detailed analysis of this peculiarity for W 33, Keto and Ho (1989) concluded that neither thermal and gravitational instabilities nor Richtmyer-Meshkov instability and shock focusing could explain the origin of the fluctuations. Accordingly, Krasnobaev *et al.* (1994) considered the interaction of a shock-ionization front system with an inhomogeneous interstellar medium. The authors found the I-S front to be capable of significantly amplifying (approximately by an order of magnitude) the perturbations penetrating from the neutral gas into the H II region if their wavelength and the separation between the fronts considerably exceeded the scale size of the postshock temperature relaxation zone. However, estimates show that during the lifetime of the I-S front, the size of the relaxation zone is comparable to the thickness of the neutral-gas layer between the fronts. Thus, the amplifi-

* E-mail address for contacts: vkkaor22@mtu-net.ru

cation of perturbations is still open to question. Below, we, therefore, analyze the effects of inhomogeneity of the interstellar medium and of radiative cooling and nonstationarity of the ionization-shock front. When performing numerical calculations, we take into account radiative cooling explicitly. We also estimate the possible contribution of the motions analyzed to the observed irregular structure of H II regions.

A TWO-FRONT MODEL
FOR THE PROPAGATION
OF AN IONIZATION-SHOCK FRONT

The oscillations of a system of I and S fronts can, of course, be analyzed in detail only by numerical methods. Nevertheless, as we show below, a number of qualitative features of the motion are well predicted in the relatively simple two-front model. According to this model, the ionization-shock front is replaced by a system of discontinuities, one of which is an isothermal shock wave (i.e., the thickness L_c of the cooling zone behind the adiabatic jump is disregarded), and the other is a weak D-type ionization front. The interaction of small perturbations with such a system of fronts was analyzed in general form by Krasnobaev *et al.* (1994). However, these authors did not investigate the pattern of the emerging motion of discontinuities. In order to interpret the results of our numerical simulations (see below), we will, therefore, consider in more detail the amplification of oscillations of the surfaces of an isothermal shock wave and an ionization front.

We restrict our analysis to the linear theory and choose the following motion as the main one.

Let a plane ionization front and the preceding shock wave propagate through a homogeneous medium with time-independent (and, for simplicity, equal) velocities. Passing to a coordinate system where the fronts are at rest, we denote the constant gas density and velocity and the isothermal speed of sound by ρ_n, u_n, and c_n ($n = 0, 1, 2$), respectively. The subscripts n refer, respectively, to the gas parameters in the H I region, in the layer between the I and S fronts, and in the H II region. We assume that in the coordinate system chosen, the x axis is perpendicular to the shock plane and parallel to the velocity of the incoming flow. The coordinates of the I and S fronts are taken to be $x_S = 0$ and $x_I = L$. Of course, when passing through the discontinuities, ρ_n, u_n, and c_n obey the ordinary conservation laws. Since the shock wave is isothermal, it is obvious that $c_1 = c_0$.

Let isothermal perturbations of the form $A \exp[i(\omega t - kx)]$, where A is constant, t is the time, ω is the frequency, and k is the wave number, emerge in the neutral gas. Below, for definiteness, we assume the following: A is the density perturbation amplitude relative to ρ_0, $\omega = (u_0 + c_0)k$, and there are no waves coming from the H II region. The flux of ionizing radiation incident on the I front is assumed to be constant.

Imagine the perturbations in positions of the shock and ionization fronts to be proportional to $\exp(i\omega t)$ with amplitudes $L_0 D$ and $L_0 F$, respectively; the choice of scale L_0 is arbitrary. By linearizing the gas-dynamical equations and conditions at the discontinuities with respect to the above main flow, we then find a relationship between the constants A, D, and F:

$$D = -\frac{ic_0\gamma_S}{\omega L_0}A; \quad F = -\frac{ic_0\gamma_I}{\omega L_0}A;$$

$$\gamma_S = 1 - \frac{q_1}{1 + q_2\exp(iq)};$$

$$\gamma_I = \frac{M_0 + 1}{M_0}\left(q_2 - \frac{M_0 + 1}{M_0 - 1}\right)\frac{\exp\left(\frac{M_0 + 1}{2M_0}iq\right)}{1 + q_2\exp(iq)}; \quad (1)$$

$$q_1 = 2\left(\frac{M_0}{M_0 - 1}\right)^2; \quad q_2 = \frac{M_0 + 1}{M_0 - 1}\frac{1 + M_2 M_0}{1 - M_2 M_0};$$

$$q = \frac{2\omega L}{c_0(1 - M_1^2)}; \quad M_n = \frac{u_n}{c_n}.$$

Relation (1) allows the natural oscillations of the I-S front to be found by assuming that $A = 0$ and by requiring that $|\gamma_S|$ and $|\gamma_I| \longrightarrow \infty$ (Landau and Lifshitz 1986). We then obtain $q = q_r + iq_i$, where $q_r = 2m\pi$ ($m = 0, \pm1, \ldots$) and $q_i = \ln(-q_2)$. Since $q_2 < -1$, $q_i > 0$ and the front is stable against one-dimensional perturbations.

If A $A \neq 0$, then the waves of fixed frequency ω propagating through an H I region have the greatest effect on the oscillation amplitudes of the I and S fronts when the thickness of the shock-compressed neutral-gas layer L is such that $|\gamma_S|$ and $|\gamma_I|$ are at a maximum. Using relation (1), we find that such values of L are reached at $q = 2m\pi$ (i.e., when the perturbation frequency is equal to the natural oscillation frequency), while $q = (2m + 1)\pi$ correspond to the minimum of $|\gamma_S|$ and $|\gamma_I|$. In this case, the ratio of the $|\gamma_S|$ maximum to its minimum is considerably larger than the same ratio for the I front. Indeed, since, generally, $M_0 \gg 1$ and M_2 is not too small, it follows from relation (1) that

$$\frac{|\gamma_I|_{max}}{|\gamma_I|_{min}} = \left|\frac{1 - q_2}{1 + q_2}\right|,$$

$$\frac{|\gamma_S|_{max}}{|\gamma_S|_{min}} = \left|\frac{1 - q_1 + q_2}{1 - q_1 - q_2}\right|\left|\frac{1 - q_2}{1 + q_2}\right| \gg \frac{|\gamma_I|_{max}}{|\gamma_I|_{min}}. \quad (2)$$

Thus, the wave interference [which is responsible for the periodic (in L) variations of γ_S and γ_I] is more pronounced for the shock wave than for the ionization front.

Clearly, the above results can also be used to describe a nonstationary I-S front if L increases with time slowly enough. In that case, the system of fronts

passes through a sequence of states that roughly satisfy relations (1). This, in particular, means that as L increases, the front oscillation amplitudes will vary with γ_S and γ_I.

However, since our conclusions are based on the linear theory and on neglect of the thickness of the temperature relaxation zone, we consider below direct numerical simulations of the dynamics of a nonstationary I-S front.

OSCILLATIONS OF A NONSTATIONARY IONIZATION-SHOCK FRONT

Numerical simulations allow the above results to be generalized. First, there is now no need to use the linear approximation in the two-front model. Second, it proves to be possible to explicitly take into account radiative cooling and the front-velocity difference. The first of these generalizations is not analyzed below, because our calculations of the interaction between small perturbations and the I-S front agree well with predictions of the linear theory. Therefore, we immediately turn to a more comprehensive description of the motion of a nonstationary ionization-shock front by taking into consideration the cooling efficiency and the S- and I-front parameters typical of the interstellar medium.

As our previous calculations show (Krasnobaev 2001), the propagation of a stationary I-S front through the interstellar medium can be accompanied by oscillations in gas parameters if the postshock cooling rate does not increase too rapidly with temperature. The oscillation amplitude in saturation is determined by separation L between the shock and ionization fronts, and it significantly increases for those q that correspond to natural oscillations with a period of $\sim 21 L_c/u_0$. It is then clear that the t dependence of L can strongly affect the oscillation amplitude if saturation is reached in a sufficiently long time interval that exceeds the interval during which $q \approx 2m\pi$. In other words, the oscillations can be significantly damped if the difference between the front velocities is large.

In order to analyze the nonstationarity of the I-S front quantitatively, let us consider a plane one-dimensional unsteady motion of gas with volume heat losses through radiative cooling. This motion is described by the system of equations

$$\frac{\partial \rho}{\partial t} + \frac{\partial \rho u}{\partial x} = 0,$$

$$\frac{\partial u}{\partial t} + u\frac{\partial u}{\partial x} + \frac{1}{\rho}\frac{\partial p}{\partial x} = 0,$$

$$\frac{\partial}{\partial t}\left(\frac{1}{\gamma-1}\frac{p}{\rho}\right) + u\frac{\partial}{\partial x}\left(\frac{1}{\gamma-1}\frac{p}{\rho}\right) + \frac{p}{\rho}\frac{\partial u}{\partial x} = -\frac{\Lambda}{\rho}, \quad (3)$$

$$p = \frac{\rho k_B T}{\mu m_H},$$

where p and T are the pressure and temperature, respectively; $\gamma = 5/3$ is the adiabatic index; Λ is the amount of energy lost per unit gas volume per unit time through radiative processes; k_B is the Boltzmann constant; μ is the mean molecular weight of the gas particles, which is taken to be 1 in a neutral gas and 1/2 in an ionized gas; and m_H is the mass of the hydrogen atom. Below, we assume that $\Lambda = \rho^2\varphi(T)$ and the degree of ionization of the interstellar medium is 10^{-2}. The function $\varphi(T)$ was chosen from the monograph of Spitzer (1981) and interpolated using a Lagrange polynomial.

We assume that $x_s = 0$ in the main flow and that the gas parameters at $x < 0$ are ρ_0, u_0, T_0, and $M_0^2 = \gamma M_\infty^2 = \rho_0 u_0^2/p_0$. We determine the distributions of ρ, u, and T at $x > 0$ from Eqs. (3) with the condition $\partial/\partial t = 0$ and take the coordinate of the I front to vary as $x_I(t) = x_{I0} + v_I t$, $v_I = \text{const}$. It is easy to see that, being generally unsteady, this motion nevertheless satisfies the gas-dynamical equations if $x_{I0} > L_c$, where

$$L_c = \frac{k_B T_s}{m_H}\frac{\rho_s u_s}{\Lambda(\rho_s, T_s)} \quad (4)$$

and ρ_s, u_s, and T_s are the gas parameters immediately behind the adiabatic jump. The structure of a cooling zone with scale length L_c has been discussed in detail previously (Krasnobaev 2001). Below, the same computational procedure and the same conditions at the boundaries of the region occupied by ionized gas as in the above paper are used to simulate a perturbed flow. In order to allow for the inhomogeneity of the interstellar medium, we specify time-dependent perturbations in ρ, u, and T at the left boundary of the computed region (in the preshock supersonic flow of neutral gas). When analyzing only the nonstationarity effects of the ionization-shock front (i.e., disregarding inhomogeneities in the H I region), we specified the initial perturbation by contracting in spatial coordinate (with a coefficient of 0.95) the distributions of ρ, u, and T corresponding to the stationary structure of the relaxation zone. For an inhomogeneous interstellar medium, there is clearly no need to specially introduce such perturbations, because the H I region now directly serves as their source. Therefore, the x dependence of ρ, u, and T at time $t = 0$ in the entire computed region was assumed to be the same as that in the main flow. Accordingly, the perturbations at $t > 0$ were caused only by the variations in ρ, u, and T specified at the left boundary.

Before analyzing the results of our calculations, let us also estimate the difference between the front velocities v_I. For this purpose, we use the standard approximate solution to the problem of spherically symmetric expansion of an H II region (Spitzer 1981). Then, $v_I \sim u_0/2M_0^2$ if the gas densities in the H I and H II regions are approximately equal. Accordingly, when passing through the ionization front, the ratio of neutral-gas
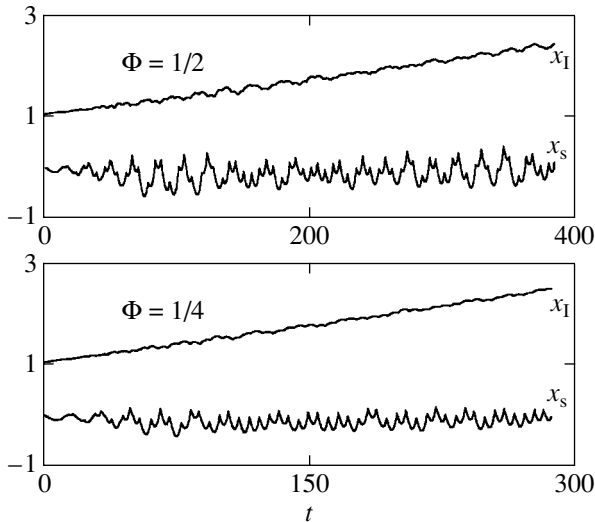
Fig. 1. Oscillations of a nonstationary ionization-shock front in the absence of perturbations in an H I region.
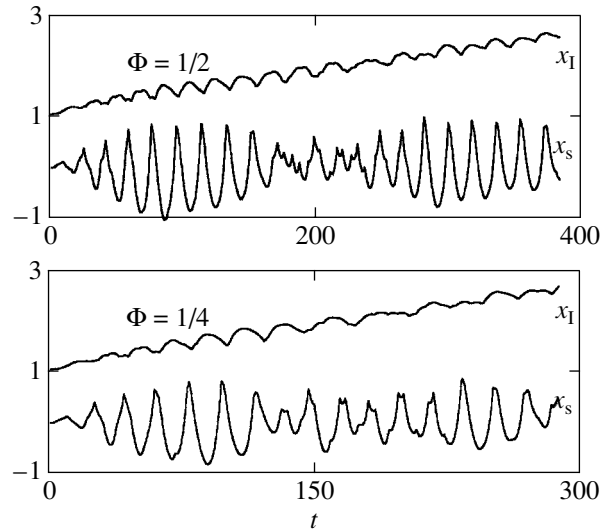

Fig. 2. Trajectories of the shock and ionization fronts in an inhomogeneous medium.

density to plasma density is $\lambda \sim M_0^2$. Of course, these values of v_I and λ should be considered only as characteristic, because ionization fronts emerge not only during the expansion of H II regions in a stationary medium but also during the motion of stars, during the flow around globules, during the ionization of individual clouds by radiation from a group of stars, etc. Therefore, in our calculations, v_I and λ were the parameters that could change; it is convenient to introduce the flux density of ionized radiation $\Phi = 1 - v_I M_0^2 / u_0$ relative to $\rho_0 u_0 / m_H$. Clearly, $\Phi = 1$ for a stationary I front, and Φ decreases with increasing v_I.

Figure 1 gives an idea of the v_I effect on x_s and x_I variations in the absence of perturbations in the H I region (i.e., for $A = 0$), where $u_0 = 17$ km s^{-1}, $\lambda = M_0^2$, and the adiabatic Mach number is $M_\infty = 10$ (the same u_0 and M_∞ also refer to the other results of our calculations presented below). In Fig. 1 and below, x_s and x_I are expressed in terms of L_c, and t is expressed in terms of L_c / u_0.

We can see that because of the front-velocity difference, the maximum shock oscillation amplitude $(x_s)_{max}$ becomes appreciably smaller than its value for a stationary I-S front, which is $2L_c$ (Krasnobaev 2001). The successive increase and decrease in oscillation amplitude predicted in terms of the two-front model manifests itself weakly as well (we emphasize that the cooling zone directly serves as the perturbation source here).

Isothermal waves of even very small amplitude in the interstellar medium cause a sharp amplification of oscillations. Thus, for example, even at $A = 0.1$ and $\tau_w = 2\pi/\omega = 17 L_c / u_0$, $(x_s)_{max}$ differs little from its value that corresponds to a stationary I-S front (here, τ_w was cho-

sen to be sufficiently close to the period of oscillations in an unperturbed interstellar medium). This is evidenced by $x_s(t)$ and $x_I(t)$ shown in Fig. 2; periodic (in time) variations of ρ and u were specified at the left boundary of the computed region when calculating these dependencies (λ is the same as in Fig. 1). Initially, the distributions of ρ, u, and T corresponded to the main flow.

It also follows from the plots in Fig. 2 that there is a distinct alternation of the maximum and minimum front displacement amplitudes, although, according to (2), it is less distinct for the I front than for the shock wave. A difference from a stationary ionization-shock front is that $(x_s)_{max}$ is now reached earlier than the maximum oscillation amplitude of the ionization front $(x_I)_{max}$. This effect can be naturally explained (but only qualitatively because of strong nonlinearity) as follows. At $v_I \neq 0$, the I front interacts with perturbations whose frequency is lower than the frequency of the waves propagating through the H I region due to the Doppler shift. Hence, according to (1), the condition $q = 2\pi m$ for the I front is satisfied at higher values of L (i.e., later in time) than for the shock wave.

The influence of amplitude A on $(x_s)_{max}$ and $(x_I)_{max}$ is illustrated in Fig. 3 for $\Phi = 1/2$ and $\lambda = 80$ for waves with the same period τ_w as in Fig. 2.

We can see that a change in A affects x_s and x_I mainly by increasing the period-averaged oscillation of the front displacement in a positive direction. This effect (it also shows up in calculations based on the two-front model) is qualitatively similar to the generation of acoustic pressure, which affects the interface between the two media.

A comparison of the plots in Figs. 2 and 3 with the same Φ and A reveals a weak dependence of $(x_s)_{max}$ and $(x_I)_{max}$ on λ. This behavior of $(x_s)_{max}$ and $(x_I)_{max}$ comes
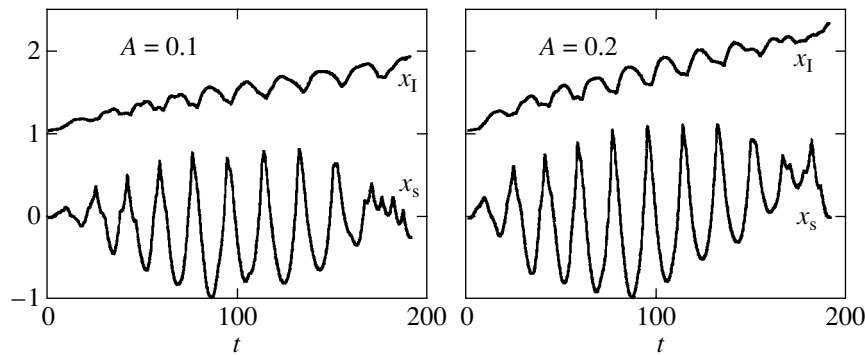
Fig. 3. Effects of the density perturbation amplitude in an H I region on the front positions.
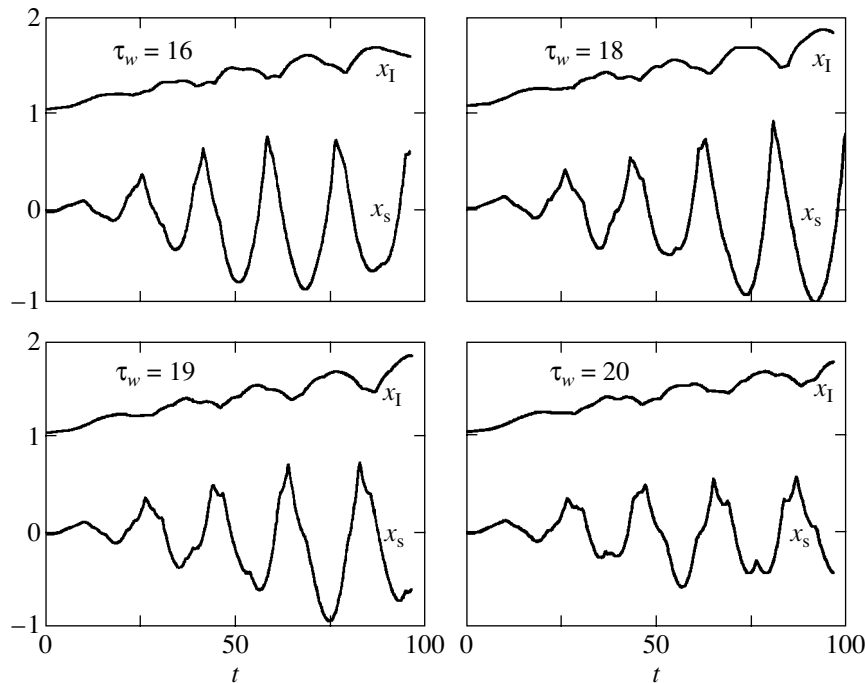

Fig. 4. Front coordinates versus wave period τ_w.

as no surprise. Indeed, Krasnobaev *et al.* (1994) showed that the parameters of the interaction between perturbations and a weak D-type I front (such as the amplitudes of the reflected and refracted waves and the reflection coefficient) for $\lambda \gg 1$ depended on λ only slightly and were close to those for the normal incidence of acoustic waves on a contact discontinuity (Landau and Lifshitz 1986).

A fixed period τ_w corresponds to the curves in Figs. 2 and 3. However, perturbations of various scales can clearly be present in the H I region; therefore, it is of interest to vary τ_w. As Fig. 4 shows, the oscillation amplitude of x_s and x_I remains fairly high when τ_w varies over the range $(16–20)L_c/u_0$ ($\Phi = 1/4$, $\lambda = M_0^2$, and $A = 0.1$ in the figure). If, alternatively, τ_w corresponds to higher frequency ($\tau_w \sim 6$ or less) natural oscillations of

the fronts, then the wave amplification is modest, as follows from (1) (see the relations between constants A, D, and F).

CONCLUSION

The results of our calculations allow the effects of nonstationarity of the ionization-shock front and inhomogeneity of the interstellar medium on the oscillation characteristics of gas parameters to be estimated quantitatively, as applied to expanding H II regions.

If, as above, we assume that $v_I \geq u_0/2M_0^2$ and use expression (4) for L_c, then we can easily find that the thickness L of the dense neutral-gas envelope between the ionization and shock fronts will exceed L_c in time $t_m \leq 7.5 \times 10^5$ years for $\rho_0/m_H = 10$ cm^{-3}. However, the evolutionary time scale of H II regions is typically

10^6 years or slightly longer (Bochkarev 1992); i.e., it is at least of the order of t_m or longer. Consequently, according to our calculations, the nonstationarity effects of the ionization-shock front are important for the growth of instability at the hydrodynamic expansion phase of H II regions.

In particular, the variations of x_s and x_I in a homogeneous interstellar medium can decrease by more than a factor of 2 compared to their maximum values for an envelope of constant thickness.

Nevertheless, even very small density inhomogeneities of the order of $(0.1-0.2)\rho_0$ in an H I region increase the front displacement amplitudes to the values that correspond to the propagation of the shock wave and the ionization front with equal velocities. The corresponding perturbations in neutral- and ionized-gas velocities lie in the range 1–3 km s^{-1}. Thus, the instability of a nonstationary ionization-shock front can be one of the mechanisms for the enhancement of weak inhomogeneities in the interstellar medium, which facilitate the formation of turbulent motions observed in H II regions.

Of course, our estimates depend on the assumed form of the cooling efficiency. Thus, for example, if the degree of ionization of the interstellar medium is higher than that used in our calculations, then the behavior of $\varphi(T)$ does not change qualitatively, while L_c and t_m decrease. However, the relative fluctuations in gas density, temperature, and velocity clearly change only slightly.

REFERENCES

1. S. I. Blinnikov, in *Proceedings of 8th Workshop on Nuclear Astrophysics*, Ed. by W. Hillebrandt and E. Muller (MPA, Garching, 1996), p. 25.

2. N. G. Bochkarev, in *Foundations of the Physics of Interstellar Medium* (Mosk. Gos. Univ., Moscow, 1992).

3. R. A. Chevalier and J. N. Imamura, Astrophys. J. **261**, 543 (1982).

4. J. N. Imamura, M. T. Wolf, and R. H. Durisen, Astrophys. J. **276**, 667 (1984).

5. V. S. Imshennik, N. L. Kal'yanova, A. V. Koldoba, and V. M. Chechetkin, Pis'ma Astron. Zh. **25**, 250 (1999) [Astron. Lett. **25**, 206 (1999)].

6. E. R. Keto and P. T. P. Ho, Astrophys. J. **347**, 349 (1989).

7. P. A. Kimoto and D. F. Chernoff, Astrophys. J. **487**, 728 (1997).

8. A. V. Koldoba, E. V. Tarasova, and V. M. Chechetkin, Pis'ma Astron. Zh. **20**, 445 (1994) [Astron. Lett. **20**, 377 (1994)].

9. K. V. Krasnobaev, Pis'ma Astron. Zh. **27**, 112 (2001) [Astron. Lett. **27**, 91 (2001)].

10. K. V. Krasnobaev and V. Yu. Tarev, Astron. Zh. **64**, 1210 (1987) [Sov. Astron. **31**, 635 (1987)].

11. K. V. Krasnobaev, N. E. Sysoev, and V. Yu. Tarev, in *Nuclear Physics, Cosmic Radiation Physics, Astronomy* (Mosk. Gos. Univ., Moscow, 1994), p. 222.

12. L. D. Landau and E. M. Lifshitz, *Course of Theoretical Physics*, Vol. 6: *Fluid Mechanics* (Nauka, Moscow, 1986; Pergamon, New York, 1987).

13. S. H. Langer, G. Chanmugam, and G. Shaviv, J. Astrophys. Lett. **245**, L23 (1981).

14. L. Spitzer, Jr., *Physical Processes in Interstellar Medium* (Wiley, New York, 1978; Mir, Moscow, 1981).

15. R. Strickland and J. M. Blondin, Astrophys. J. **449**, 727 (1995).

16. R. Walder and D. Follini, Astron. Astrophys. **315**, 265 (1996).

17. M. T. Wolf, J. H. Gardner, and K. S. Wood, Astrophys. J. **346**, 833 (1989).

Translated by V. Astakhov

A Spectroscopic Study of the Envelope
of the Recurrent Nova CI Aquilae

M. A. Burlak* and V. F. Esipov

Sternberg Astronomical Institute, Universitetskiĭ pr. 13, Moscow, 119899 Russia
Received April 5, 2001

Abstract—Spectroscopic observations of the recurrent Nova CI Aql in the wavelength range 4000–11 000 Å are presented. Its evolution is traced from maximum light to the disappearance of nebular lines. $\langle E_{B-V} \rangle = 0.91 \pm 0.11$, as inferred from the Balmer decrement. The mean expansion velocity of the envelope measured near maximum light is 2800 km s^{-1}. The helium abundance in the Nova envelope has been found to be enhanced, $\langle \mathrm{He/H} \rangle = 0.22$. CI Aql is similar in spectral evolution, in change of the envelope expansion velocity, and in helium abundance to other recurrent novae. © *2001 MAIK "Nauka/Interperiodica"*.

Key words: *recurrent novae, spectroscopic observations, envelopes, chemical composition*

GENERAL INFORMATION

The first outburst of CI Aql was observed in 1917. The star had magnitudes of 11^m and $15\overset{m}{.}5$ at maximum and minimum brightness, respectively (General Catalog of Variable Stars, GCVS). These data were not enough to estimate the time scales for the Nova.

A recurrent outburst of CI Aql was discovered on April 28, 2000, when the star was on the ascending branch of its light curve and had $m_V = 10^m$. Its coordinates are $\alpha = 18^h52^m03^s55$ and $\delta = -1°28'38''9$ (2000). Based on visual and photoelectric *V*-band estimates from IAU Circulars (2000), we plotted the light curve for CI Aql (Fig. 1). The circles indicate the monochromatic magnitudes at $\lambda = 5450$ Å determined from the available spectra. We estimated the following parameters of the Nova from its light curve:

$$m_{V\max} = 8\overset{m}{.}8; \quad \mathrm{JD}_{\max} \cong 2\,451\,666;$$

$$t_{2V} = 30^d; \quad \log 100^d = 0.8;$$

$$t_{3V} = 50^d.$$

The color index of the Nova at maximum brightness was $B-V = 0.67$ (Hanzl 2000). Judging by the available data, the star had a prolonged maximum ($\sim 7^d$); therefore, we took the point of maximum brightness as the time of the maximum. Using a statistical relation between the absolute magnitude at maximum brightness and the brightness decline rate after the maximum (Cohen 1985), we derived the absolute magnitude at

maximum, $M_V = -7\overset{m}{.}1$. By its decline rate, CI Aql belongs to the mF (moderate fast) type (Payne-Gaposchkin 1957).

SPECTROSCOPIC OBSERVATIONS

The spectra of CI Aqr were taken at the Crimean Station of the Sternberg Astronomical Institute with a fast spectrograph attached to the 125-cm reflector. The detector was a SBIG-6I CCD camera with 375×242 pixels in ordinary mode and with 750×242 pixels in spectral mode. The spectral resolution with a 600 lines mm^{-1} diffraction grating was ~6 Å per pixel and, in spectroscopic mode, ~3 Å per pixel. The observed range was 4000 to 11 000 Å. The total spectrum of the Nova consisted of two, occasionally of three or four, partially overlapping frames corresponding to different tilts of the grating. The spectral range of each frame was ~2000 Å. We took several frames with different exposures and chose the best from them, usually with the longest exposure time, during reduction.

The spectroscopic observations of CI Aql in 2000 were carried out from May until October. A log of our observations is given in Table 1. In the spectral-range columns, the numbers denote the following wavelength ranges: 4000–5800 Å (1), 5700–7600 Å (2), 7500–9400 Å (3), and 9300–11000 Å (4). The third column lists the magnitudes of CI Aql: visual magnitudes in May and monochromatic magnitudes on the remaining dates. In addition to CI Aql, we observed the spectra of standard stars used for calibration: 50 Boo, 3 Vul, 4 Aql, 24 Vul, 57 Cyg, and 40 Cyg. Their spectral energy distributions, in units of erg cm^{-2} s^{-1} A^{-1}, were taken from Glushneva (1982).

The initial frame reduction was performed using the ST6 code supplied with the CCD array. We made cor-

---

* E-mail address for contacts: mburlak@sai.msu.su

rections for the spectral response and corrected magnitudes for the atmosphere by using the standard stars. No correction was made for the airmass difference (however, $\Delta F(z)$ did not exceed 0.1). The spectra were calibrated with the ESIP.EXE and KOEFF.EXE programs written by A.M. Tatarnikov. The SPE code written by S. Sergeev at Crimean Astrophysical Observatory was used for the subsequent reduction of the spectra. Line intensities were determined using the SPE code. The accuracy of measuring the intensities of most weak lines is estimated to be 30%.

DESCRIPTION
OF THE SPECTRAL EVOLUTION

The first observations ($\Delta t \cong 5-8^d$) were performed when CI Aql was still at maximum brightness, which lasted several days. At this time, the spectrum exhibited the Balmer Hα, Hβ, Hγ, and Hδ lines with P Cyg profiles. Apart from the hydrogen lines, the Fe II $\lambda5018$, $\lambda5169$, and $\lambda6149$ Å lines, as well the He I $\lambda5876$ and N II $\lambda5680$ Å lines, had similar profiles. The He I $\lambda4471$, $\lambda6678$, $\lambda7065$, N III $\lambda4640$, Fe II $\lambda4924$, $\lambda5317$ Å lines were observed without absorption components. Examples of the spectra for this observing period are shown in Figs. 2 and 3.

By the next series of observations ($\Delta t \cong 60^d$ and 62^d), CI Aql was already at the nebular stage. The spectrum changed significantly. The absorption components disappeared in all lines. The Hα line split up into two peaks. The iron lines in the range 4900–5200 Å vanished, and nebular lines appeared instead. The neutral helium lines became much weaker. The blend of N III $\lambda4640$ Å, $\lambda4515$ Å, $\lambda4518$ Å and He II $\lambda4686$ Å became the strongest feature in the spectrum. The He II $\lambda5411$ Å line and the blend of [Fe VI] $\lambda5146$ Å and

Table 1. A log of spectroscopic observations for CI Aql

Date, 2000	Δt, days	V	Camera		Spectroscopic mode	
			spectral range	exposure, min	spectral range	exposure, min
May 6	5	$\sim9^m$	1	1	1	0.5
			2	1	2	0.5
May 7	6	~9	1	1		
			2	1		
			3	1; 1	3	1
			4	1	4	1
May 9	8	~9	1	3		
			2	1; 3	2	0.5
			3	5		
			4	10		
June 30	60	13.2	1	20		
			2	20	2	0.5; 1
July 2	62	13.3	1	30		
			2	15		
July 24	84	13.7	1	30		
			2	30	2	1
Sept. 3	125	13.9	1	30		
			2	30		
Oct. 1	153	14.3	1	30		
			2	30		
Oct. 24	176	14.6	1	30		
			2	30	2	1

$\lambda5176$ Å appeared. Examples of the spectra for this observing period are shown in Figs. 4 and 5.

Twenty days later ($\Delta t \cong 84^d$), the neutral helium virtually disappeared from the spectrum. The nebular lines essentially faded away. At the same time, the ionized helium lines strengthened, and the [Fe VII] $\lambda6087$ Å
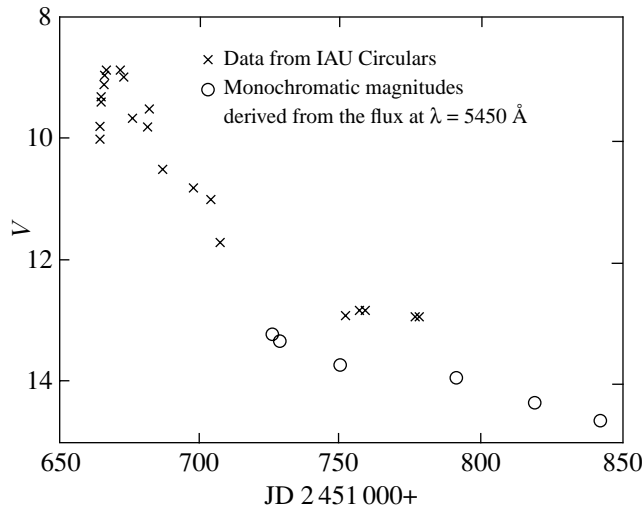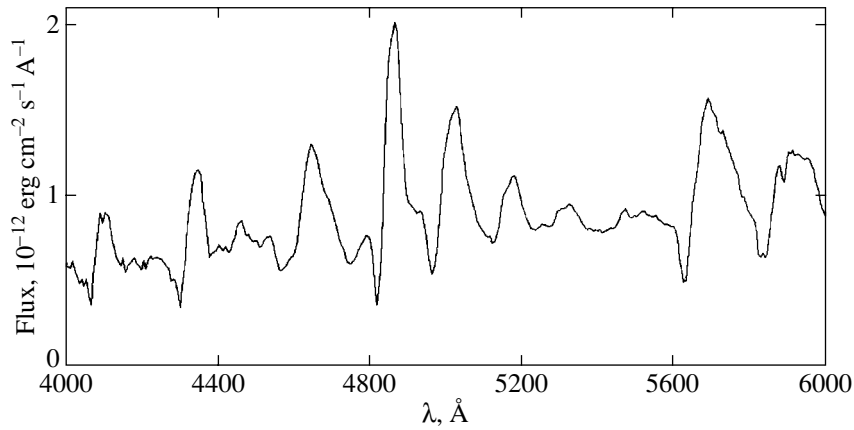

Fig. 1. The light curve for CI Aql.

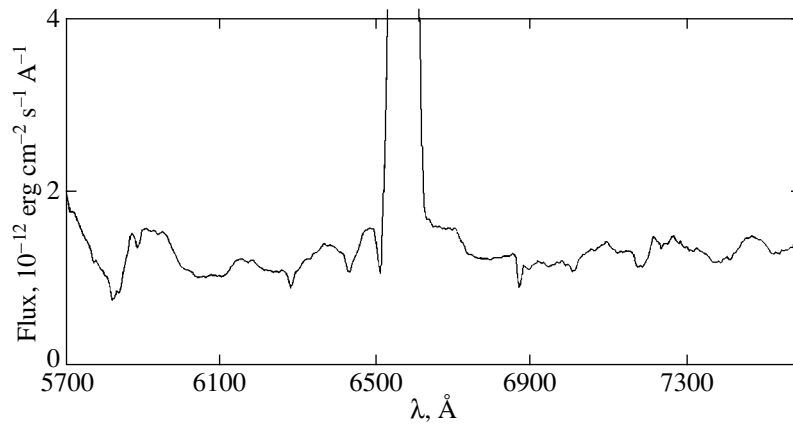**Fig. 2.** The 4000–6000 A spectrum of CI Aql taken on May 9, 2000.

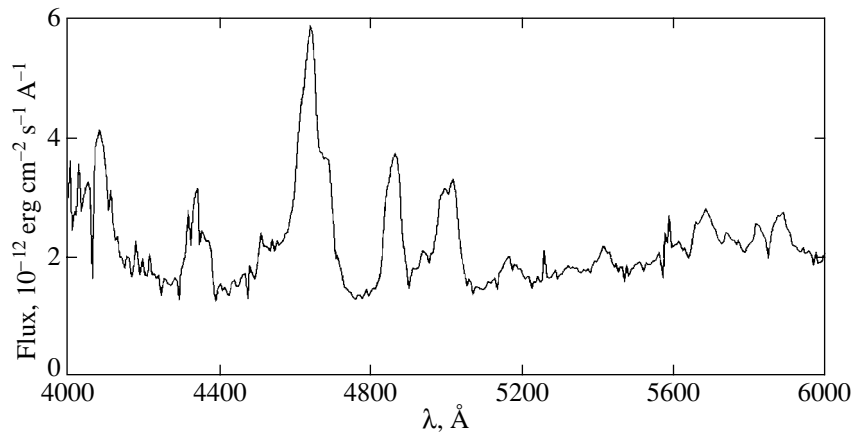**Fig. 3.** The 5700–7600 Å spectrum of CI Aql taken on May 9, 2000.

Fig. 4. The 4000–6000 Å spectrum of CI Aql taken on July 2, 2000.

line appeared. Subsequently, the He II and [Fe VII] lines continued to strengthen. By the last observation ($\Delta t \cong 176^d$), the ionized helium had been enhanced so that the He II $\lambda 5411$ Å line became comparable in intensity to Hβ. The spectrum of CI Aql on the last date of our observations is shown in Figs. 6 and 7.

The visibility phase of the [O III] lines in CI Aql was very short. By $\Delta t \cong 84^d$, the nebular lines had virtually

Table 2. Expansion velocities of the CI Aql envelope from the absorption components of P Cyg profiles (km s^{-1})

	Hδ	Hγ	Hβ	λ5018 Å Fe II	λ5169 Å Fe II	λ5680 Å N II	Hα
May 6	2630	2910	2900	2080	2670	2680	2600
May 7	2630	2500	2530	3460	3000	2990	2330
May 9	2630	3320	2890	3460	3000	3280	2330;
(two peaks in Hα)							3110

Table 3. Expansion velocities of the CI Aql envelope from the line FWHM (km s^{-1}). The last column gives the separation between the Hα components (km s^{-1})

	Hδ	Hγ	Hβ	λ5018 Å Fe II	λ5169 Å Fe II	Hα	Hα (Δλ)
May 5	2300	2840	2320	3190	2820	2510	–
May 7	2500	3000	2240	3580	2940	2640	–
May 9	2810	2900	2760	3500	3170	2920	–
June 30	–	–	3870	–	–	2890	2060
July 2	–	–	2890	–	–	2800	2100
July 24	–	–	3310	–	–	2900	1830
Sept. 3	–	–	2700	–	–	3230	1280
Oct. 1	–	–	1740	–	–	2100	780
Oct. 24	–	–	1430	–	–	1730	–

Table 4. Color excess from the Balmer decrement

	June 30	July 2	July 24	Sept. 3	Oct. 1	Oct. 24
E_{B-V}	0.78	0.93	0.93	1.05	0.79	1.00

disappeared. Such behavior is characteristic of recurrent novae.

EXPANSION VELOCITIES OF THE CI AQL ENVELOPE

On May 6, 7, and 9, the lines of hydrogen, iron, and other elements exhibited P Cyg profiles. After June 30, the Balmer lines and [O III] λ5007 Å split into two components. Figures 8 and 9 show the Hα profiles for the above periods. The velocities measured from the Fe II λ5018 Å and λ5169 Å lines are, on average, higher than the velocities determined from the hydrogen lines. As the brightness declined, the envelope expansion velocities decreased, which is particularly characteristic of recurrent novae. Tables 2 and 3 give the expansion velocities of the CI Aql envelope derived from absorption components of the P Cyg profiles of hydrogen, ionized iron, and N II lines, as well as from the FWHMs of emission lines. The last column of Table 3 gives the separation between the peaks of the Hα pro-

file, in km s^{-1}. The mean expansion velocity in May was ~ 2800 km s^{-1}.

THE COLOR EXCESS OF CI Aql

After June 30, when the absorption components of emission lines disappeared from the spectrum of CI Aql, it became possible to measure the hydrogen-line intensities to determine the interstellar reddening from the Balmer decrement. Theoretical decrements were taken from Aller (1984). The results are presented in Table 4. The mean color excess was taken to be $\langle E_{B-V} \rangle = 0.91 \pm 0.11$.

DETERMINING THE HELIUM ABUNDANCE IN THE ENVELOPE OF CI AQL

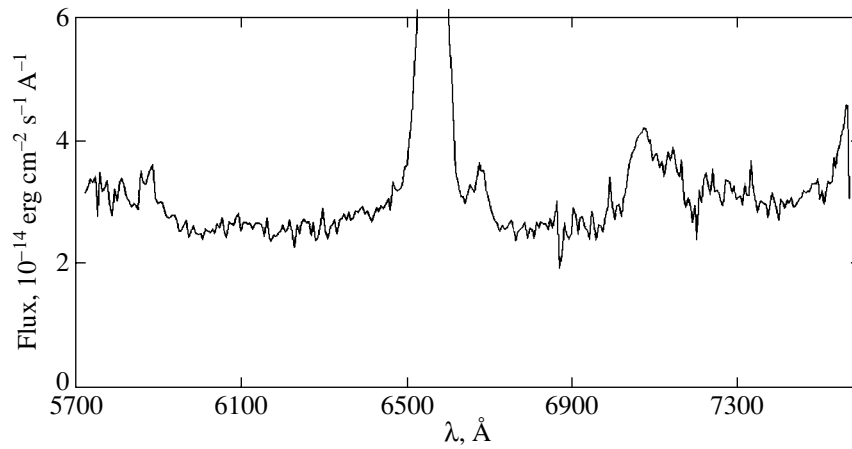Chemical-composition measurements revealed a helium overabundance in recurrent novae (Pottasch 1959):

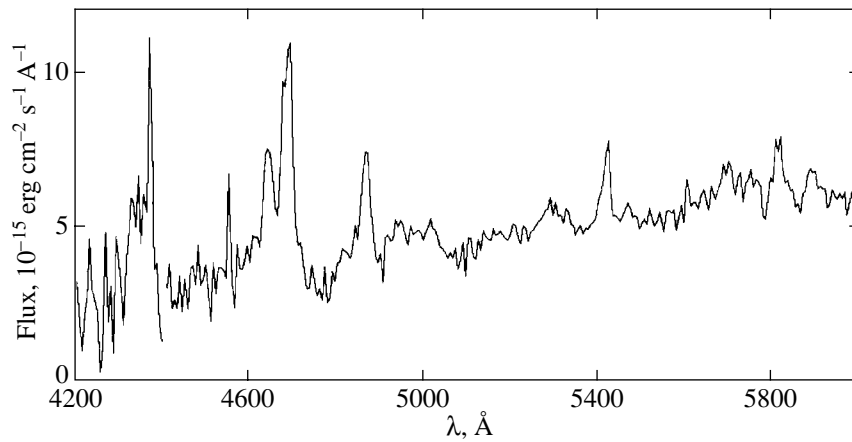**Fig. 5.** The 5700–7600 Å spectrum of CI Aql taken on July 2, 2000.

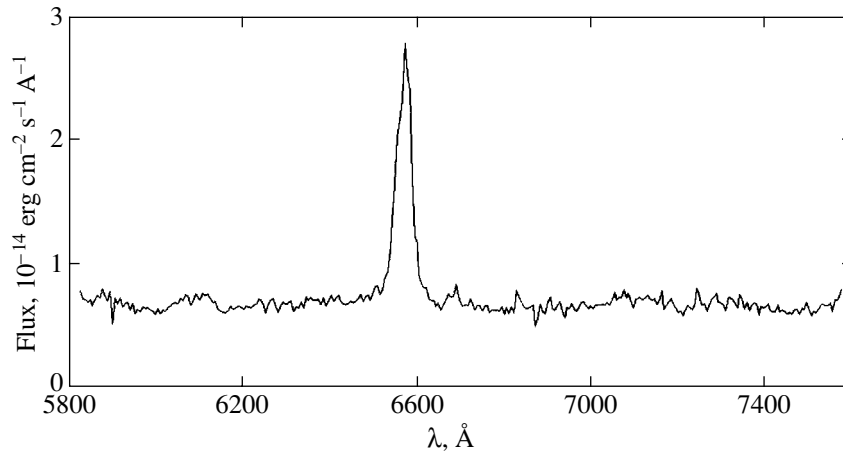**Fig. 6.** The 4200–6000 Å spectrum of CI Aql taken on October 24, 2000.

Fig. 7. The 5800–7600 Å spectrum of CI Aql taken on October 24, 2000.

GK Per – He/H = 0.18;
RS Oph – He/H = 0.43;
V603 Aql – He/H = 0.32.

It is, therefore, of interest to estimate the helium abundance in CI Aql. Unfortunately, we could not determine individual plasma parameters in the Nova envelope, so we took the mean temperature and elec-
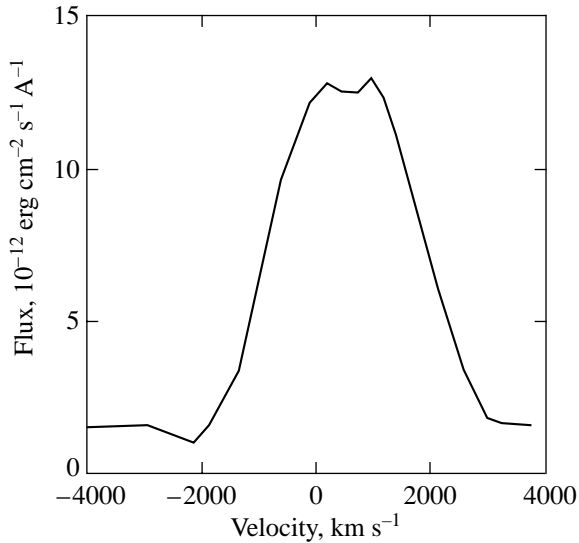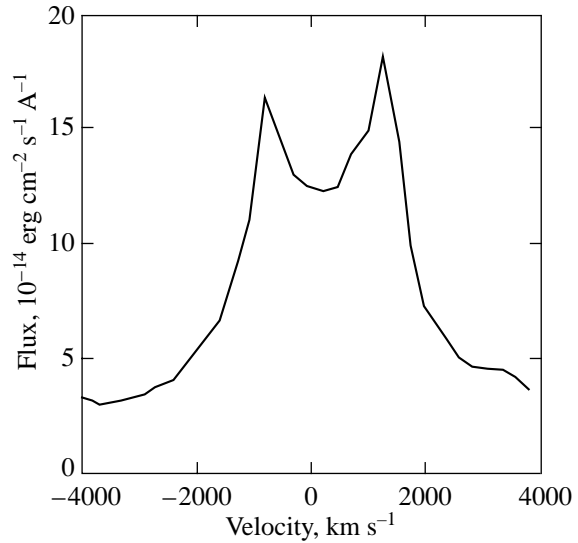
Fig. 8. The Hα profile on May 9, 2000.

Fig. 9. The Hα profile on June 30, 2000.

tron density for novae at the nebular phase: $T_e = 11\,000$ K, $N_e = 10^7$ cm^{-3} (Snijders 1990). We mainly estimated the He^{++} abundance, because the He I lines were very weak. All formulas for our calculations were taken from Aller (1984) and Clegg (1987).

The total helium abundance is the sum of the He^0, He$^+$, and He^{++} abundances. The unobservable ionization state He^0 was disregarded, because all helium in the Nova envelope is believed to be ionized. We determined the He$^+$ abundance from the He I $\lambda 5876$ Å line. The relation for this line is (Aller 1984)

$$\log \frac{N(\text{He}^+)}{N(\text{H}^+)} = -0.133 + 0.235 \times \log t_e + \log \frac{I(\lambda 5876)}{I(\text{H}\beta)},$$

where $t_e = T_e/10^4$ K.

The He^{++} abundance was derived from the $\lambda 4686$ Å line. The corresponding formula is (Aller 1984)

$$\log \frac{N(\text{He}^{++})}{N(\text{H}^+)} = -1.077 + 0.135 \times \log t_e$$
$$+ \frac{0.135}{t} + \log \frac{I(\lambda 4686)}{I(\text{H}\beta)}.$$

For the true He$^+$ abundance to be determined, we must take into account the collisional excitation of the metastable He I $2s^2\ ^3S$ level, whose contribution increases with gas electron density. The method of allowance and the correction factors C/R as a function of temperature and density are given in Clegg (1987).

The mean helium abundance in the envelope of the recurrent Nova CI Aql was found to be $\langle \text{He/H} \rangle = 0.22$. Our results are presented in Table 5. Thus, as in other recurrent novae, the helium abundance in the envelope of CI Aql proved to be appreciably higher than its solar value.

Table 5. Relative intensities of the helium lines uncorrected for interstellar reddening and the helium abundance in the CI Aql envelope

Date	$I(\lambda 5876)/I(\text{H}\beta)$	He$^+$/H	$I(\lambda 4686)/I(\text{H}\beta)$	He^{++}/H$^+$	He/H
June 30	0.143	0.070	0.133	0.152	0.222
July 2	0.105	0.052	0.082	0.094	0.146
July 24	–	–	0.108	0.123	>0.123
Sept. 3	–	–	0.208	0.237	0.237
Oct. 1	–	–	0.242	0.276	0.276
Oct. 24	–	–	0.267	0.305	0.305

CONCLUSION

We have investigated the recurrent Nova CI Aql constructed its complete *V* light curve, determined the characteristic photometric parameters, identified spectral lines, traced the spectral evolution until the disappearance of nebular lines, measured the envelope expansion velocities, and determined the color excess and the helium abundance. The spectral evolution of CI Aql was characterized by a short nebular phase, which began between days 8 and 60 after the maximum and ended by day 84.

The plasma parameters should also be considered. In general, the correct choice of the electron density and especially the electron temperature is of great importance in determining the envelope chemical composition. Apart from the errors associated with line intensity measurements, a large uncertainty stems from the fact that many collisionally excited lines are very sensitive to the assumed temperature and density. In our case, the plasma parameters have virtually no effect on the result, because the recombination lines used in our analysis are not very sensitive to temperature, while knowledge of the density is necessary only to allow for the collisional excitation of He I lines. Thus, the error in the helium abundance is mainly determined by the accuracy of measuring line intensities and does not exceed 30%. We found an enhanced helium abundance for CI Aql, characteristic of recurrent novae. A large helium overabundance in recurrent novae may suggest that there is an evolved cool component rather than a main-sequence star in the binary system.

REFERENCES

1. L. H. Aller, *Physics of Thermal Gaseous Nebulae* (D. Reidel, Dordrecht, 1984).
2. R. E. S. Clegg, Mon. Not. R. Astron. Soc. **229**, 31 (1987).
3. J. G. Cohen, Astrophys. J. **292**, 90 (1985).
4. D. Hanzl, IAU Circ., No. 7411 (2000).
5. IAU Circ., Nos. 7409, 7411, 7426, 7436, 7444, 7482 (2000).
6. C. Payne-Gaposchkin, *The Galactic Novae* (North-Holland, Amsterdam, 1957).
7. S. R. Pottasch, Ann. Astrophys. **22**, 412 (1959).
8. M. A. J. Snijders, *Physics of Classical Novae: Proceedings of Colloquium No. 122 of the International Astronomical Union, Madrod, 1989*, Ed. by A. Cassatella and R. Viotti (Springer-Verlag, New York, 1990), p. 188.
9. *Spectrophotometry of Bright Stars*, Ed. by I. N. Glushneva (Nauka, Moscow, 1982).

Translated by N. Samus'

Masses and Radii of the Components of V1016 Ori

É. A. Vitrichenko[1]* and S. I. Plachinda[2]

[1] *Space Research Institute, Russian Academy of Sciences, ul. Profsoyuznaya 84/32, Moscow, 117810 Russia*
[2] *Crimean Astrophysical Observatory, National Academy of Sciences of Ukraine, p/o Nauchnyĭ, Crimea, 334413 Ukraine*
Received February 15, 2001; in final form, April 11, 2001

Abstract—On January 2/3, 2001, eight spectra of the star V1016 Ori were taken with the 2.6-m Crimean Astrophysical Observatory telescope on the descending branch of its eclipse. The spectral range $\lambda\lambda 5299$–5365 ÅÅ was chosen to be without strong lines of the primary B0 star, emission lines of the Orion Nebula, and telluric lines. Adding up the spectra and optimum filtering yielded a signal-to-noise (S/N) ratio of ~600. We managed to identify thirteen lines of an A star that belong to the secondary component and seven lines of an M star that presumably belong to θ^1 Ori B1 (third star); the latter lies $0\overset{''}{.}2$ north of the binary system and was discovered by speckle interferometry. One of the lines is in emission. The radial velocities of both stars were measured. We calculated the components' mass ratio, $q = 0.19$. We also determined the semiamplitude of the secondary's radial-velocity curve, $K^{\mathrm{a}} = 172$ km s^{-1}, the components' masses, $M^{\mathrm{a}} = 21 M_\odot$ and $M^{\mathrm{b}} = 3.9 M_\odot$, and radii, $R^{\mathrm{a}} = 3.7 R_\odot$ and $R^{\mathrm{b}} = 3.6 R_\odot$. The measured radial velocity $V_r^{\mathrm{c}} = 33$ km s^{-1} of θ^1 Ori B1 matches the binary's γ velocity, within the error limits, which argues for the assumption that θ^1 Ori B1 is physically associated with the eclipsing system. The superscripts a, b, and c imply that a quantity belongs to the primary star, the secondary star, and θ^1 Ori B1, respectively. We estimated an upper limit on the projected rotational velocity for the secondary component and the third star, $V \sin i < 30$ km s^{-1}. © *2001 MAIK "Nauka/Interperiodica".*

Key words: *eclipsing binaries, component mass and radius determination*

INTRODUCTION

V1016 Ori (=HD 37 020) is one of the four brightest stars in the Orion Trapezium. This is an eclipsing star (Lohsen 1975); its radial-velocity curve was constructed by Lohsen (1976) and Vitrichenko *et al.* (1998). The system's period is $65\overset{\mathrm{d}}{.}4$, its magnitude outside eclipse is $V = 6\overset{m}{.}75$, and the spectral type of the primary star is B0 V (Vitrichenko 1998). *UBVR* and *UBVRI* observations were obtained by Zakirov (1979) and Bondar' *et al.* (2000), respectively. The stellar spectrum was studied by Ismailov (1988), Bossi *et al.* (1989), Cunha and Lambert (1992, 1994), and Vitrichenko and Klochkova (2000).

The star's continuum was studied over a wide ($\lambda\lambda 0.36$–4.7 μm) spectral range (Vitrichenko 1999). The observed flux was shown to be represented as the sum of the fluxes from four radiation sources: (1) a B0 V primary of the eclipsing system; (2) an A0 V secondary of the eclipsing system; (3) a dust envelope around the secondary component with the temperature $T_{\mathrm{d}} = 1600$ K; and (4) an infrared object with a temperature $T \sim 3000$ K. The age of the Orion Trapezium stars is estimated to be 10^4–10^5 years. Since the early evolutionary stages of

massive stars have not been studied adequately, investigating V1016 Ori can give valuable information.

The components' masses and radii can be determined from their light and radial-velocity curves. Unfortunately, no secondary lines have been detected so far, which complicates the problem but still allows these parameters to be estimated under certain assumptions (Vitrichenko *et al.* 1998). It follows from the light curve that the two components are comparable in brightness (Zakirov 1979), but the spectrum of only one component is observed (Vitrichenko *et al.* 1998). The contradiction can be explained by the fact that a semi-transparent dust envelope around the secondary star rather than the secondary itself produces an eclipse (Vitrichenko 1998). The light-curve solution obtained by Zakirov (1979) is based on the assumptions of a circular orbit and a total eclipse. Both assumptions are wrong. A more accurate solution was obtained by Bondar' *et al.* (2000), who showed the secondary to be a factor of ~10 fainter than the primary in *V*.

Bossi *et al.* (1989) pointed out that the radius of the primary star determined from the light and radial-velocity curves was half the radius derived from the luminosity and temperature. The authors failed to explain this paradox. The paradox was resolved by Bondar' *et al.* (2000). The authors found yet another solution of the light curve, which satisfied the observations. Previously, a solution has been sought for the

---

* E-mail address for contacts: vitrich@nserv.iki.rssi.ru

Table 1. Information on the spectra

No.	JD 2 451 912+	Phase	ΔV
59 686	0.290	0.9945	$0\overset{m}{.}07$
59 687	0.311	0.9948	0.10
59 689	0.346	0.9953	0.17
59 690	0.367	0.9957	0.23
59 691	0.389	0.9960	0.27
59 692	0.410	0.9963	0.33
59 693	0.431	0.9966	0.38
59 694	0.452	0.9970	0.47

"giant star in front of small star" (GS) hypothesis, where the secondary is cooler and larger in diameter than the primary and lies in front of the primary during an eclipse. We managed to obtain a new solution for the "small star in front of giant star" (SG) hypothesis. For the SG hypothesis, the components' radii turn out to be virtually the same, with the primary's radius being a factor of ~1.3 larger than that for the GS hypothesis.

Felli *et al.* (1989) detected radio emission from the star at a wavelength of 6 cm. The other Orion Trapezium stars exhibit no such emission. A flare was reliably detected at this wavelength (Felli *et al.* 1991). The authors concluded that the secondary was an active T Tau star.

Several cases of the star's optical and infrared brightness instability are known. For example, Bondar' *et al.* (2000) noted that during the observations of Lohsen (1975), the star was by $0\overset{m}{.}26$ brighter in *U* near its primary minimum than observed by all the other authors. In another case, during Zakirov's observations during 1991–1992, the star was brighter by $0\overset{m}{.}35$ in *R* than observed by other authors. Vitrichenko (1999) discovered that the star was brighter in infrared bands than observed by other authors; in addition, one of the observations revealed a flare.

The companion θ^1 Ori B, which coincides in sky position with the radio source, was discovered in V1016 Ori by speckle interferometry. The eclipsing system does not coincide in position with the radio source (Petr *et al.* 1998). Thus, the hypothesis of Felli *et al.* (1991) about the nature of the binary's secondary component is called into question, because θ^1 Ori B1 is more likely to be a T Tau star. The star (below referred to as the third star) lies $0\overset{''}{.}2$ north of the binary. Its magnitudes are $K^c = 7\overset{m}{.}65$ and $H^c = 7\overset{m}{.}75$ (Petr *et al.* 1998).

Our main objective is to detect secondary lines of the binary system, which will allow the components' masses and radii to be determined. We know in advance that the problem is complex, because it follows from

light-curve solution that the secondary is a factor of ~10 fainter in *V* than the primary. In addition, there is a third star in the system, which is several times brighter than the secondary in *HK*. The *V* brightness of this star is not known.

OBSERVATIONAL DATA AND THEIR REDUCTION

The observations were obtained with the 2.6-m telescope at Crimean Astrophysical Observatory (CrAO). The detector was a CCD array. The wavelength range $\lambda\lambda 5299$–5365 ÅÅ was investigated. This range was chosen, because it did not contain any strong primary lines, intense nebular emission lines, and noticeable telluric lines.

Information on the observed spectra is given in Table 1. The first column lists spectrum numbers by CrAO nomenclature. The second column gives mid-exposure Julian dates (reduced to the Sun). In all cases, the exposure time was 30 min. The last two columns give, respectively, the photometric phases calculated with the elements

$$\text{Min I} = \text{HJD } 2\,441\,966.820 + 65.4331 \cdot E, \qquad (1)$$

from Bondar' *et al.* (2000) and the brightness losses calculated with the photometric elements from the same paper.

We formulated the observational problem as follows: to take spectra near the maximum eclipse phase. In that case, secondary lines must be a factor of ~3 deeper than those outside eclipse. Because of orbital ellipticity, the radial velocities of the stars at conjunction differ by ~100 km s^{-1}, which allows us to determine their velocity ratio and, hence, their mass ratio and the masses themselves.

In addition, it is necessary to ensure the maximum possible S/N ratio. To this end, we must take several spectra, add them up, and perform optimum filtering.

During the 2000/2001 observing season, the problem in the formulated form proved to be impossible to solve. The point is that the phases are repeated in 131 days at the same time of the day. Therefore, the minimum does not occur at culmination of the star in the midnight during each season. There was no such a minimum during the above season. Moreover, there is no such a minimum in the next 2001/2002 season either. The best observing conditions were on January 2/3, 2001, when the spectra were obtained. However, all spectra were taken not at the maximum eclipse phase but on the descending branch of the light curve. The last and eighth spectrum was obtained when the star set; subsequently, it was impossible to continue the observations.

Figure 1 shows the portion of the light curve that was calculated from the photometric elements taken from Bondar' *et al.* (2000) for the SG hypothesis. On this curve, the times when the spectra were taken are marked by asterisks. We see from the figure that the

spectroscopic observations were obtained at the beginning of the descending branch of the light curve.

The key question in searching for secondary lines is to achieve a sufficiently high S/N ratio. A preliminary analysis of the spectroscopic data shows that the first seven spectra are considerably better in quality than the eighth spectrum. Therefore, the first seven spectra were added up and filtered with a 0.6-Å-wide rectangular window. As a result, the S/N ratio was

$$S/N = (N_1 N_2 N_3)^{1/2} = 600, \qquad (2)$$

where $N_1 = 5600$ is the mean number of measured points per pixel, $N_2 = 7$ is the number of spectra, and $N_3 = 10$ is the number of averaged pixels. The S/N ratio in formula (2) is a factor of ~1.5 higher than that in Vitrichenko and Klochkova (2000), who failed to find any secondary lines.

The above S/N ratio is expressed in fractions of the continuum. To estimate the chance of success in searching for weak lines, it is better to express the S/N ratio in terms of the line depth. As we will see from the subsequent analysis, the mean depth of secondary lines is $r_0 \sim 0.005$, in fractions of the continuum; therefore, by the new definition,

$$(S/N)_1 \sim r_0(S/N) = 3. \qquad (3)$$

The notion of S/N ratio was introduced to estimate the significance of a pulse response. A spectral line is not a pulse; its profile is described by several points. Let us estimate this effect by using the simplified model of a rectangular line. We assume the width of this rectangle to be $2\sigma = 1.6$ Å, where $\sigma = 0.8$ Å is the mean parameter of the Gaussian fit to the line profile. In that case, the central part of the line is described by $N_4 = 2\sigma/\Delta = 2.7$ independent points, where $\Delta = 0.6$ Å is the filter width. In reality, the number of points is twice as large, because the filter is displaced by half of its width, but half of these points are independent.

Finally, we obtain the following estimate for the S/N ratio:

$$(S/N)_2 = (S/N)_1 N_4^{1/2} = 5. \qquad (4)$$

The required S/N ratio is a matter of convention, but the condition S/N > 3 is used most commonly. In our case, the condition is satisfied with a margin, which leads us to conclude that the results of our search for secondary lines are statistically significant. The fact that the spectra were obtained on the descending branch of the light curve increases the depths of secondary lines r_0 on average, by a factor of 1.2 (the desired signal increases).

Each of the spectra before the averaging procedure was subjected to the standard reduction adopted at CrAO: dark-current subtraction, flat fielding, the removal of hot and cold pixels, sky background subtraction, wave-
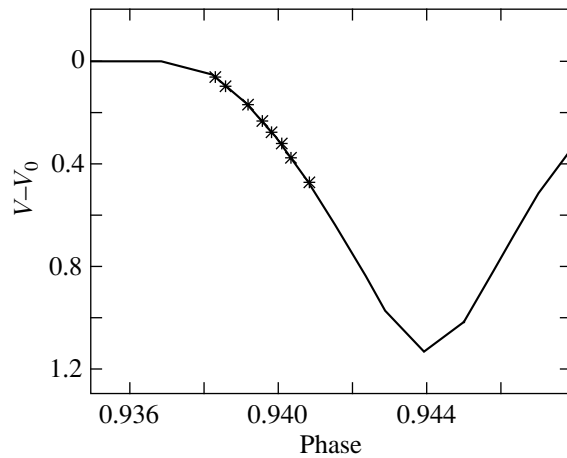

Fig. 1. Part of a theoretical light curve for V1016 Ori near its primary minimum (solid line). The asterisks mark the times when the spectra were taken. The phase is measured from periastron passage by the stars.

length calibration, and correction for the Earth's motion around the Sun, which was $\Delta V_r = -8.8$ km s^{-1}.

The spectra were calibrated in wavelength by using a comparison spectrum whose light source was an argon-filled lamp with a hollow thorium cathode. The instrumental profile was determined from lines of this lamp. Its Gaussian parameter was found to be $\sigma = 0.2$ Å, which is a factor of 4 smaller than the measured line width in the average spectrum. When the radial velocities are determined, the error attributable to a difference between the dispersion curves obtained from the two comparison spectra on both sides of the observed spectrum is introduced (Vitrichenko and Plachinda 2000). This error is systematic in nature, and its maximum value is ~1 pixel = 0.066 Å = 4 km s^{-1}. However, since we used the mean parameters of the dispersion curve, the systematic error cannot exceed 2 km s^{-1}.

THE SPECTRUM OF V1016 ORI

A visual examination of the eight spectra and the average spectrum clearly revealed reproducible features in them. However, an attempt to identify these features with a particular set of spectral lines for a star of a particular spectral type failed.

As a way out, we computed a grid of synthetic spectra with different stellar model parameters and calculated the cross-correlation function between the observed and synthetic spectra. This function is exemplified in Fig. 2.

Parameters of the model that was used to construct the synthetic spectrum are given in the figure caption. All these parameters were varied, and an example of one of the most suitable functions is shown in Fig. 2.

All cross-correlation functions shared a common property: they were bimodal. This forced us to consider the hypothesis that the spectrum consisted of three superimposed spectra: the spectrum of a B0 primary
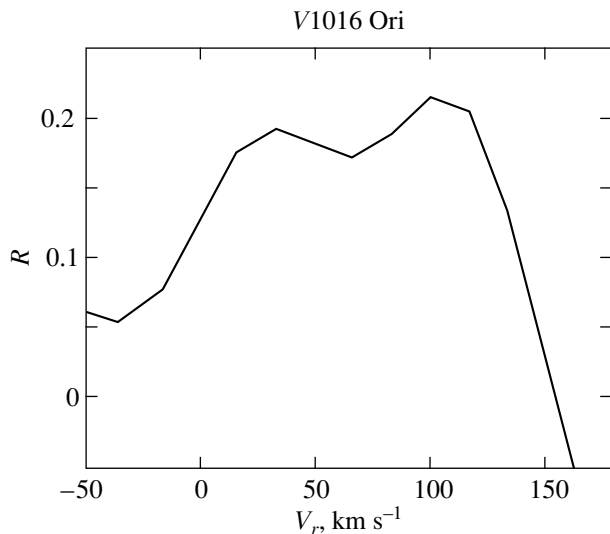
V1016 Ori

star with unidentified lines (the spectral range was chosen so), the spectrum of an A star (presumably the binary's secondary component), and the spectrum of an M star (presumably the star θ^1 Ori B1). Only in terms

of this hypothesis did we manage to make sense of the observed spectrum. Figure 2 reveals the following important fact: the lines of the A and M stars have radial velocities of ~120 and ~20 km s^{-1}, respectively, which gives a criterion for separating two sets of lines. In addition, the lines of the M star are slightly narrower and belong to neutral species in all cases, while some of the lines in the spectrum of the A star belong to ions.

Figure 3 shows the observed spectrum of V1016 Ori (the solid line in the middle) and two synthetic spectra computed with the ATLAS9 code from the STARSP software package (Tsymbal 1995). The synthetic spectrum computed with the following atmospheric parameters: effective temperature T_{eff} = 8000 K, surface gravity $\log g$ = 4.5, projected rotational velocity $V\sin i$ = 30 km s^{-1}, microturbulence ξ_t = 2 km s^{-1}, and departure from solar metallicity [M/H] = 0, is shown at the top. The spectrum was arbitrarily displaced upward by 0.016, in fractions of the continuum. Another synthetic spectrum computed with the atmospheric parameters T_{eff} = 3500 K, $\log g$ = 3.5, $V\sin i$ = 30 km s^{-1}, ξ_t = 2 km s^{-1}, and [M/H] = 0 is shown at the bottom. The spectrum was arbitrarily displaced downward by 0.016, in fractions of the continuum. According to tables from Straizis and Kuriliene (1981), the upper and lower
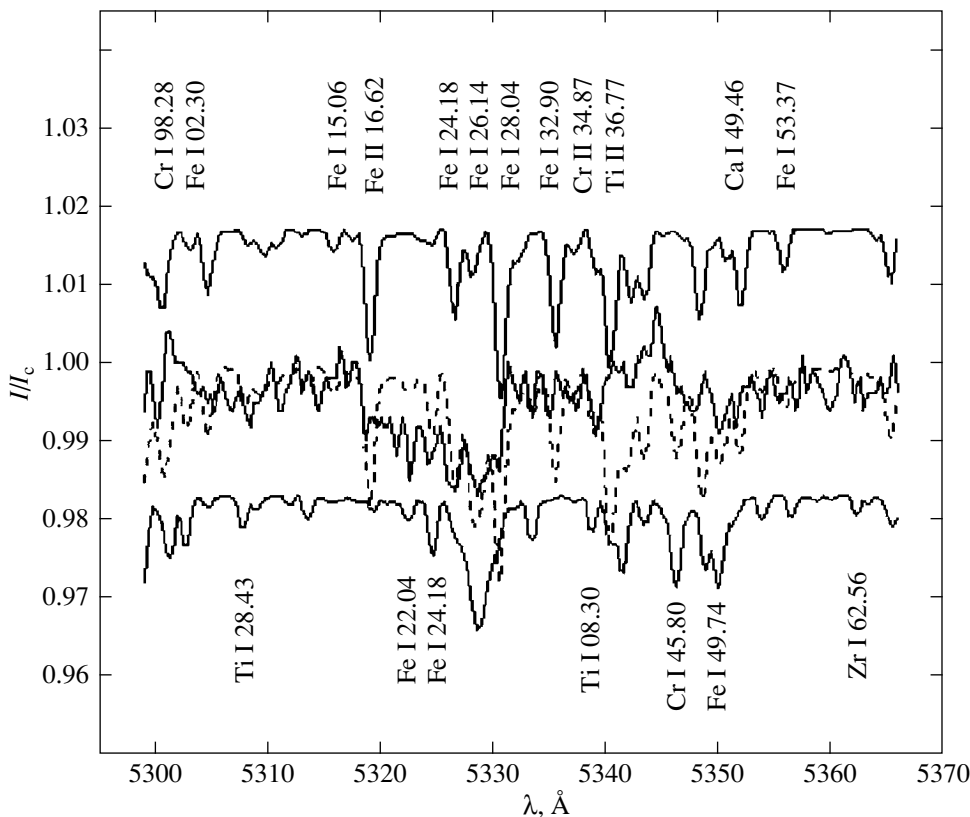

Fig. 3. Comparison of the observed spectrum for V1016 Ori (middle) with two synthetic spectra: for A7 V (upper) and M2 IV (lower) stars. Wavelengths (in Å) and intensities (in fractions of the continuum) are plotted along the horizontal and vertical axes, respectively. The dotted line represents the total spectrum (for details on its construction, see the text).

Table 2. Information on lines of the A star

Species	λ, Å	V_r, km s^{-1}	W_λ, mÅ	Blend	$O{-}C$
Cr I	5298.28	127	7	Cr I 8.46	-2
Fe I	5302.30	130	2	Fe II 2.66	-1
Fe I	5315.06	123	3		-6
Fe II	5316.62	136	14	Fe II 6.78	7
Fe I	5324.18	139	27	M star	10
Fe I	5326.14	130	7		1
Fe I	5328.04	127	26	Cr I 8.38	2
Fe I	5332.90	123	8	Si I 3.24	-6
Cr II	5334.87	123	6	M star	-6
Ti II	5336.77	134	12		5
Fe I	5339.93	123	2		-6
Ca I	5349.46	125	3	FeII 9.18	-4
Fe I	5353.37	134	10		5

spectra correspond to A7 V and M2 IV stars, respectively. The lines of the A and M stars identified in the observed spectrum are indicated at the top and at the bottom of the figure, respectively. The first two digits in the wavelengths were omitted.

Below, the spectral types of the stars are quite arbitrary. The available data are clearly insufficient for their two-dimensional classification.

When constructing Fig. 3, we displaced each of the synthetic spectra along the wavelength axis by a value corresponding to the radial velocity for a given set of lines. The radial velocities for the A7 V and M2 IV stars were found to be $V_r^{\mathrm{b}} = 129(2)$ and $V_r^{\mathrm{c}} = 33(5)$ km s^{-1}, respectively. The errors, in units of the last digit, are given in parentheses. Each of the synthetic spectra was scaled by using the relation

$$I = 1 - (1 - I_1)L, \qquad (5)$$

where L is the components' relative luminosity, which was chosen in such a way that the line depths of the observed and synthetic spectra roughly coincided. In Eq. (5), I is the scaled spectrum and I_1 is the computed synthetic spectrum. $L^{\mathrm{b}} = 0.07$ and $L^{\mathrm{c}} = 0.02$ for the spectra of the A and M stars, respectively.

The dotted line in Fig. 3 indicates the sum of the spectra I calculated from

$$I = 0.91 + I^{\mathrm{b}}L^{\mathrm{b}} + I^{\mathrm{c}}L^{\mathrm{c}},$$

where the first term is the weighting factor for the primary star (without lines), and the other two terms represent the synthetic spectra multiplied by their weighting factors.

The sum of the spectra indicated by the dotted line is in satisfactory agreement with the observed spectrum. It would be unreasonable to expect better agree-

ment, because the atmospheric parameters of the secondary component and the third star are unknown and because there is no information about their chemical composition.

Information on the measured lines is given in Tables 2 and 3. The first five columns list, respectively, species, VALD wavelengths (Kupka *et al.* 1999), measured radial velocities, equivalent widths, and the strongest blending lines. The wavelengths for these lines are given without the first three digits. There are generally no lines of the third star in the secondary spectrum, but in two cases, they can belong both to the secondary and to the third star (marked in the tables). The last column gives radial-velocity deviations from the mean.

The mean central line depth is $r_0 = 0.005$, in fractions of the continuum.

Figure 3 reveals two peculiar features: first, an almost rectangular dip in the wavelength range 5318–5332 ÅÅ and, second, an emission line near $\lambda = 5345$ Å.

The dip is attributable to the superposition of lines from the A and M stars. The right and left boundaries form the two strongest lines of the A star: Fe II 5316.62

Table 3. Information on lines of the M star

Species	λ, Å	V_r, km s^{-1}	W_λ, mÅ	Blend	$O{-}C$
Ti I	5308.43	21	4		-12
Fe I	5322.04	48	6	A star	15
Fe I	5324.18	21	8		-12
Ti I	5338.30	47	14	A star	14
Cr I	5345.80	40	6		7
Fe I	5349.74	30	6		-3
Zr I	5362.56	27	2		-6

and Fe I 5328.04. These two lines are an important criterion that allows the secondary's atmospheric parameters to be roughly estimated. They are strongest in the spectral range under consideration for $T_{eff} \sim 8000$ K and $\log g \sim 4.5$. At different atmospheric parameters, different strong lines that are unobservable in the spectrum emerge.

We can only speculate about the emission line. There are no emission lines of the Orion Nebula in this spectral range (Kaler 1976). The line most likely belongs to the third star. Its measured wavelength is 5344.7(1) Å. Given the radial velocity of the third star, it can be the Fe II 5344.09 line excited by the fluorescence mechanism (Shevchenko 1989). The rapid variability of this line also argues for this suggestion. Over the observing period, its intensity initially increased by tens of times and subsequently decreased by several times.

The most convincing evidence for the existence of the third star's spectrum is the blend near 5329 Å. There are no strong lines in the A star here, while in the M star, six strong lines (Fe I 5328.04, Cr I 5328.38, Fe I 5328.53, Ti I 5328.73, Cr I 5329.14, and Cr I 5329.74) are concentrated. These lines are unresolvable but contribute significantly to the formation of the rectangular dip.

STELLAR MASSES AND RADII

The components' mass ratio was derived from the formula

$$q = (\gamma - V_r^a)/(V_r^b - \gamma) = 0.19(1), \qquad (6)$$

where $V_r^a = 9.5$ km s^{-1} is the radial velocity of the primary star calculated from the spectroscopic elements (Vitrichenko *et al.* 1998), $V_r^b = 129(2)$ km s^{-1} is the radial velocity of the secondary star determined above, and $\gamma = 28.3(10)$ km s^{-1} is the radial velocity of the binary's center of mass. The error in q was calculated from the error in γ.

The secondary's radial-velocity semiamplitude is given by

$$K^b = K^a/q = 172(10) \text{ km s}^{-1}, \qquad (7)$$

$K^a = 32.7(15)$ km s^{-1} is the primary's radial-velocity semiamplitude (Vitrichenko *et al.* 1998).

The stellar masses can easily be determined from the above data:

$$M^a = 21(2)M_\odot, \quad M^b = 3.9(4)M_\odot. \qquad (8)$$

The masses turned out to be a factor of ~2 larger than those obtained previously by invoking certain assumptions (Vitrichenko *et al.* 1998), but they are in good agreement with the masses typical of zero-age

main-sequence (ZAMS) stars, $M^a = 16(4)M_\odot$ and $M^b = 3(1)M_\odot$ (Straizis and Kuriliene 1981).

The orbital semimajor axis a and the stellar radii R^a and R^b were found to be

$$a = 200(14)R_\odot, \quad R^a = 3.7(3)R_\odot, \quad R^b = 3.6(3)R_\odot. \quad (9)$$

When calculating the masses and radii, it may be assumed, with a sufficient accuracy, that $\sin i = 1$. The radii were calculated for the SG hypothesis.

The discrepancy between the masses and radii estimated here and those determined previously proves to be significant. It should be borne in mind, however, that we have managed to measure secondary lines for the first time, which allowed the parameters of the system's components to be determined without any assumptions. Previously, the fourth-power law has been assumed to hold for the mass-luminosity relation. It may well be that this assumption breaks down for the stars in question. A sharp kink in the mass-luminosity relation is known to be near $10M_\odot$. This can account for the discrepancy in the mass estimates.

In any case, it becomes necessary to perform again such a work using new spectra. Recommendations on how to obtain them are discussed below.

PROJECTED ROTATIONAL VELOCITY

Strong single lines are commonly used to determine the projected rotational velocity. Unfortunately, there are no such lines in the observed spectral range. We, therefore, estimated the projected rotational velocity from the strongest and least distorted (by blends) lines. The Ca I 5349.46 and Fe I 5349.74 lines were used for the A and M stars, respectively.

The spectral range with the above lines is shown in Fig. 4. The solid line represents the observed average spectrum. The circles and asterisks indicate synthetic Fe I 5349.74 and Ca I 5349.46 profiles, respectively. The two synthetic profiles were computed with $V\sin i = 30$ km s^{-1}.

An examination of Fig. 4 shows that the observed and synthetic line profiles are in satisfactory agreement.

The Gaussian parameters for the observed line profiles were estimated from the average spectrum to be 0.5 and 0.6 Å for Fe I and Ca I, respectively. These values are close to the filter width. Therefore, the stars' projected rotational velocities cannot be determined, $V\sin i < 30$ km s^{-1} may be taken as an upper limit.

A ROUGH ESTIMATE OF THE SPECTRAL TYPE FOR THE THIRD STAR

The third star was first discovered by Petr *et al.* (1998). Its radiation was found when analyzing the continuum of V1016 Ori (Vitrichenko 1999). Weigelt *et al.* (1999) confirmed the existence of the third star in the system.
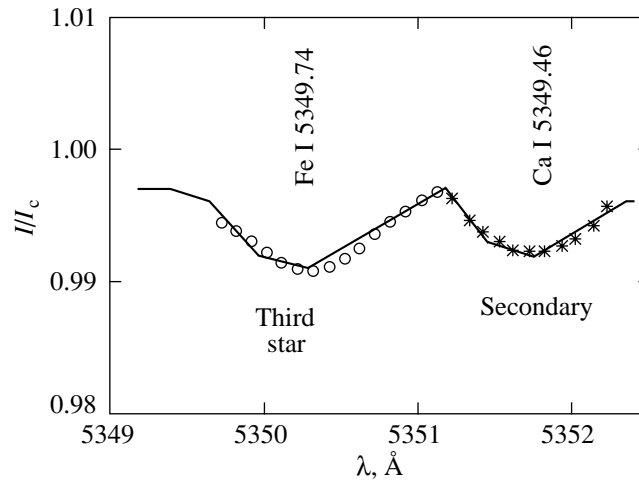
Fig. 4. The spectral range with Ca I 5349.46 belonging to the secondary component and with Fe I 5349.74 belonging to the third star. The solid line represents the observed spectrum. The circles and asterisks indicate computed synthetic line profiles for $V\sin i = 30$ km s^{-1}.

The first attempt to determine the star's spectral type was made by Vitrichenko (1999). The author estimated its effective temperature, $T_{\rm eff} \sim 3000(500)$ K and bolometric luminosity, $L \sim 150 L_{\odot}$. According to Straizis and Kuriliene (1981), these parameters correspond to the spectral type M4(2) IV.

Let us attempt to estimate the spectral type of the third star by using the $V–K$ color index. We use $L^{\rm c}$ derived here to determine the V magnitude and the measurements of Weigelt *et al.* (1999), Ney *et al.* (1973), and Petr *et al.* (1998) as well as our analysis of the continuum (Vitrichenko 1999) to determine the K magnitude.

We took $L^{\rm c} = 0.02$ for the V band, which yields $V^{\rm c} = 6\overset{m}{.}75 - 2.5 \log L^{\rm c} = 11\overset{m}{.}0$. The magnitude corrected for interstellar extinction is $(V^{\rm c})_0 = 10\overset{m}{.}2$. According to Weigelt *et al.* (1999), the ratio of K fluxes from the third star and the eclipsing system is 0.25(1); hence $L^{\rm c} = 0.25/(1 + 0.25) = 0.20(1)$. We obtain $(K^{\rm c})_0 = 6\overset{m}{.}28 - 2.5 \log L^{\rm c} = 8\overset{m}{.}0(1)$. Petr *et al.* (1998) derived $K = 7\overset{m}{.}65(5)$ for the third star, which is in satisfactory agreement with the previous value. The mean is $K = 7\overset{m}{.}8(2)$. The color index is $(V^{\rm c} - K^{\rm c})_0 = 2\overset{m}{.}4(2)$. This color is typical of a K1(1) III star (Straizis 1977).

Here, we assumed the spectral type of the secondary component to be M2. This estimate agrees well with the estimate obtained by analyzing the continuum, but disagrees with the last result. However, two factors should be taken into account. First, the above estimates are highly inaccurate. Second, there is every reason to believe that the third star is variable photometrically and, hence, spectroscopically.

The assumption that the third star is embedded deep into a dust cloud and, hence, has reddened must be rejected. This assumption is in conflict with the satisfactory agreement between the radial velocities of the binary's center of mass and the third star, suggesting their physical association. We may, therefore, draw a definitive conclusion that the third star is a cool giant.

DISCUSSION

In our discussion, we raise the following questions: (1) What are the requirements for spectroscopic observations of V1016 Ori that would provide more comprehensive information about the secondary component? (2) What can cause instability of the light curve? (3) Can the paradox concerning the radius of the primary star be resolved? (4) How good is the agreement between different determinations of the secondary's relative V luminosity?

Experience in reducing the spectra allows us to formulate recommendations on a further study of the star. First, spectra should be taken near the maximum eclipse phase, which causes an increase in the depth of secondary lines by a factor of ~ 3 (an increase in signal). Second, the total exposure time should be ~ 4 h (spectrum addition, noise reduction). Third, observations must cover a wide spectral range. Such observations will make it possible to find and measure many secondary lines, to determine the secondary's atmospheric parameters, and to estimate its chemical composition.

We know four cases of occasional changes in stellar flux. Two of them were noted by Bondar' *et al.* (2000). During the observations of Lohsen (1975), the star was by $0\overset{m}{.}26$ in V brighter near the primary minimum than observed by all the other authors. During Zakirov's observations in 1991–1992, the star brightened by $0\overset{m}{.}35$ in R. The third case was noted by Vitrichenko (1999): the star was brighter in infrared bands than observed by other authors; in addition, a flare was

Table 4. Radius of the primary star

Method of determination	R^a, $R_\odot$
Light and radial-velocity curves	3.7(3)
Luminosity and temperature	3.6(3)
Surface gravity and mass	5(1)

observed against this brightening. Finally, radio emission was detected from the star, which cannot be in a normal star. This anomalous emission exhibited a flare (Felli *et al.* 1989, 1991).

The variability cases noted above cannot be explained by observational errors, as they are reliable. We may assume the following. Both components of the eclipsing system are photometrically stable. All instability manifestations are coupled with the third star, which shows evidence of T Tau stars. Such stars are characterized by ultraviolet flares attributable to hot-gas radiation and by flares and brightenings in the infrared and radio ranges attributable to an increase in dust-envelope temperature. Both types of flares are maintained by the accretion mechanism. The spectra of T Tau stars exhibit emission lines of neutral and singly ionized species, which are excited by the fluorescence mechanism (Shevchenko 1989).

The paradox concerning the primary's radius lies in the fact that this radius determined from the light and radial-velocity curves is half the radius determined from the temperature and luminosity (Bossi *et al.* 1989). By now, three new results have been obtained, which allow the problem to be reconsidered. First, a new light-curve solution (SG hypothesis) was found, in which the relative radius of the primary star is a factor of ~1.3 larger than that for the GS hypothesis used previously. Second, we found the orbital semimajor axis to be a factor of ~1.25 larger than its previous estimates, causing the components' radii to increase. Third, $\log g$ was determined spectroscopically (Vitrichenko and Klochkova 2000), which, together with the mass deduced here, allows a third independent estimate to be obtained for the radius.

The R^a determinations are summarized in Table 4.

R^a determined from the light and radial-velocity curves is given in formula (9). The error in R^a is attributable to the error in semimajor axis a.

The standard relation between luminosity, radius, and temperature yields $R^a = 3.6(3)R_\odot$. We took $T_{\text{eff}} = 29\,700(700)$ K (Vitrichenko and Klochkova 2000), $M_V = -2^{m}_{.}21(5)$ (Bondar' *et al.* 2000), and BC $= -2^{m}_{.}9$ (Straizis and Kuriliene 1981). The error in the bolometric correction introduces the largest uncertainty.

By comparing the first two R^a determinations, we may conclude that the paradox noted by Bossi *et al.*

(1989) has been resolved. The radii coincide, within the error limits.

Using the surface gravity $\log g = 4.4(2)$ derived by Vitrichenko and Klochkova (2000) from a spectroscopic analysis and the primary's mass determined here, we made a third determination of the primary's radius (see the last row in Table 4). It is consistent with the other two radius determinations, but the error is comparatively large. The error in R^a is attributable to the error in $\log g$.

We drew the following general conclusion from the above analysis: the primary's radii determined by three independent methods based on observations alone coincide, within the error limits. This conclusion is also important because it confirms that the estimates of all the other observed parameters used to calculate the radius are correct.

Let us consider the question of whether the secondary's relative luminosity L^b roughly estimated here agrees with its three other values determined previously by different methods.

The wavelength range under consideration is fairly close to the effective wavelength of the V band, suggesting that our estimate $L^b = 0.07$ refers to this band. The error is difficult to estimate, because the brightness was determined by fitting. The primary star was dimmed by a factor of 1.2 (for the average spectrum); in that case, $L^b = 0.06$ outside eclipse.

There are three more determinations of this quantity made by independent methods. An analysis of the continuum energy distribution for the V band yielded $L^b = 0.10$ (2) (Vitrichenko 1999). The secondary's spectral type was assumed to be A0 V. Light-curve solution in terms of the GS and SG hypotheses (Bondar' *et al.* 2000) gives $L^b = 0.10(2)$ and $L^b = 0.04(2)$, respectively. The four values of L^b are in satisfactory agreement with each other. This fact is an important confirmation that the spectrum was interpreted correctly.

The mean of the four determinations is $L^b = 0.08(1)$. The out-of-eclipse V magnitude of the entire system is $V = 6^{m}_{.}75(1)$ (Bondar' *et al.* 2000). The secondary's magnitude is then $V^b = 6^{m}_{.}75 - 2.5 \log L^b = 9^{m}_{.}5(1)$. The interstellar extinction toward the system is $A_V = 0^{m}_{.}85(5)$ (Vitrichenko 1999). The extinction-corrected magnitude is $(V^b)_0 = 8^{m}_{.}7(1)$. In these calculations, the radiation from the third star can be disregarded.

CONCLUSION

Our main result is that we have managed to observe and measure secondary lines of the eclipsing system V1016 Ori for the first time.

We managed to determine the components' mass ratio, $q = 0.19$, as well as their masses, $21M_\odot$ and

$3.9M_\odot$, and radii, $3.7R_\odot$ and $3.6R_\odot$, from the measured radial velocity.

We detected lines of the third star, presumably θ^1 Ori B1, in the spectrum. The radial velocity of this star agrees, within the error limits, with the γ velocity of the eclipsing system, suggesting that the third star is physically associated with the eclipsing system.

We estimated an upper limit on the projected rotational velocity of the secondary component and the third star: $V\sin i < 30$ km s^{-1} for both stars.

ACKNOWLEDGMENTS

REFERENCES

1. N. I. Bondar', É. A. Vitrichenko, and M. M. Zakirov, Pis'ma Astron. Zh. **26**, 525 (2000) [Astron. Lett. **26**, 452 (2000)].

2. M. Bossi, A. Gaspani, M. Scardia, and M. Tadini, Astron. Astrophys. **222**, 117 (1989).

3. K. Cunha and D. L. Lambert, Astrophys. J. **399**, 586 (1992).

4. K. Cunha and D. L. Lambert, Astrophys. J. **426**, 170 (1994).

5. M. Felli, M. Massi, and V. Churchwell, Astron. Astrophys. **217**, 179 (1989).

6. M. Felli, M. Massi, and M. Catarzi, Astron. Astrophys. **248**, 453 (1991).

7. N. Z. Ismailov, Pis'ma Astron. Zh. **14**, 327 (1988) [Sov. Astron. Lett. **14**, 138 (1988)].

8. J. B. Kaler, Astrophys. J. **31**, 517 (1976).

9. F. Kupka, N. E. Piskunov, T. A. Ryabchikova, *et al.*, Astron. Astrophys. **138**, 1 (1999).

10. E. Lohsen, Inf. Bull. Var. Stars, No. 988 (1975).

11. E. Lohsen, Inf. Bull. Var. Stars, No. 1211 (1976).

12. E. P. Ney, D. W. Strecker, and R. D. Gehrz, Astrophys. J. **180**, 809 (1973).

13. M. G. Petr, V. C. Foresto, S. V. W. Beckwith, *et al.*, Astrophys. J. **500**, 825 (1998).

14. V. S. Shevchenko, *Herbig Ae/Be Stars* (Fan, Tashkent, 1989).

15. V. Straizis, *Multicolor Stellar Photometry* (Mokslas, Vilnius, 1977; Pachart Publ. House, Tucson, 1992).

16. V. Straizis and G. Kuriliene, Astrophys. Space Sci. **89**, 353 (1981).

17. V. V. Tsymbal, Astron. Soc. Pac. Conf. Ser. **108**, 198 (1995).

18. É. A. Vitrichenko, Pis'ma Astron. Zh. **24**, 708 (1998) [Astron. Lett. **24**, 611 (1998)].

19. É. A. Vitrichenko, Pis'ma Astron. Zh. **25**, 220 (1999) [Astron. Lett. **25**, 179 (1999)].

20. É. A. Vitrichenko and V. G. Klochkova, Pis'ma Astron. Zh. **26**, 133 (2000) [Astron. Lett. **26**, 104 (2000)].

21. É. A. Vitrichenko and S. I. Plachinda, Pis'ma Astron. Zh. **26**, 456 (2000) [Astron. Lett. **26**, 390 (2000)].

22. É. A. Vitrichenko, V. G. Klochkova, and S. I. Plachinda, Pis'ma Astron. Zh. **24**, 352 (1998) [Astron. Lett. **24**, 295 (1998)].

23. G. Weigelt, Y. Balega, T. Preibisch, *et al.*, Preprint No. 799 (Max Plank Inst., 1999).

24. M. M. Zakirov, Perem. Zvezdy **21**, 223 (1979).

Translated by V. Astakhov

On the Stationary Configuration
of the Heliospheric Sheet

M. M. Molodensky*

Institute of Terrestrial Magnetism, Ionosphere, and Radiowave Propagation, Russian Academy of Sciences,
Troitsk, 142092 Russia

Abstract—The expansion of solar coronal plasma is considered for the model described in Koutchmy *et al.* (1999). In addition to a spherical solar surface, the initial configuration represents a heliospheric sheet of dense plasma in the dipole equatorial plane. The heliospheric-sheet current decreases with distance as $1/r^2$, with its sign being opposite to the sign of the initial-dipole current. The latter follows from the fact that the plasma sheet is denser than the surrounding corona and that the equilibrium condition for the sheet in the gravitational and magnetic fields is satisfied. The field lines of this configuration are nearly straight. We have obtained a general solution of the steady-state MHD equations, which depends not only on distance r but also on latitude θ. Applicability of the solution to interpreting observational data, in particular, those obtained from the Ulysses spacecraft, is discussed. © *2001 MAIK "Nauka/Interperiodica"*.

Key words: *solar corona, heliospheric sheet*

INTRODUCTION

The Parker solution of the hydrodynamic equations for the solar wind is spherically symmetric. The initial approximation for it is the hydrostatic equilibrium of a gravitating gaseous sphere without any magnetic field and rotation. Accordingly, the boundary conditions refer to $r = R_\odot$ or $r = 1$ AU, and they do not depend on angular coordinates.

The solution of static equations including a magnetic field rather than the hydrostatic solution should be considered as a more realistic initial approximation. In this case, the simplest configuration is axially symmetric rather than centrally symmetric. Data on the solar wind outside the ecliptic plane are now available (Ulysses), and spacecraft that will fly above the solar poles at a distance of $\sim 20 R_\odot$ are scheduled to be launched (Solar Probe and others). The goal of these experiments is to investigate parameters of the magnetic field and the solar wind at various heliographic angles.

Koutchmy *et al.* (1995), Molodensky *et al.* (1996), and Vedenov *et al.* (2000) have shown that the main coronal structures—the so-called coronal helmets and streamers—are identified with Whitney's folds and pleats of the heliospheric-sheet surface $B_r = 0$. In general, this sheet is curved and can be constructed from data on the photospheric field. It follows from these results that the heliospheric sheet is actually observable

at a distance of $\sim 1 R_\odot$ and that it produces the main coronal structures.

For the subsequent theoretical constructions, we may disregard the curvature of the sheet and consider basic parameters of the solution—pressure, density, current, temperature—as functions of r and θ. An axisymmetric solution of the magnetostatic equations was obtained by Koutchmy *et al.* (1999). Here, our aim is to analyze the steady-state plasma expansion in the derived configuration.

MAGNETIC-FIELD CONFIGURATION

In the case of axial symmetry, the magnetic field can be expressed in terms of the poloidal magnetic flux $\psi = A_\varphi r \sin\theta$, where A_φ is the azimuthal component of the vector potential:

$$\psi = \tau + \sin\theta \sum_{n=1}^{\infty} C_n \frac{P_n^1(\cos\theta)}{r^n},$$

$$\tau = -\frac{q}{k} \ln \cosh(k\cos\theta). \tag{1}$$

Below, we consider a dipole initial field ($n = 1$), a thin sheet ($k \approx 20$), and $C_1/q < 0$, where $C_1 = M$ is the dipole term in the expansion of the potential. For the choice of τ made in Eq. (1), the magnetic field and the current are

---

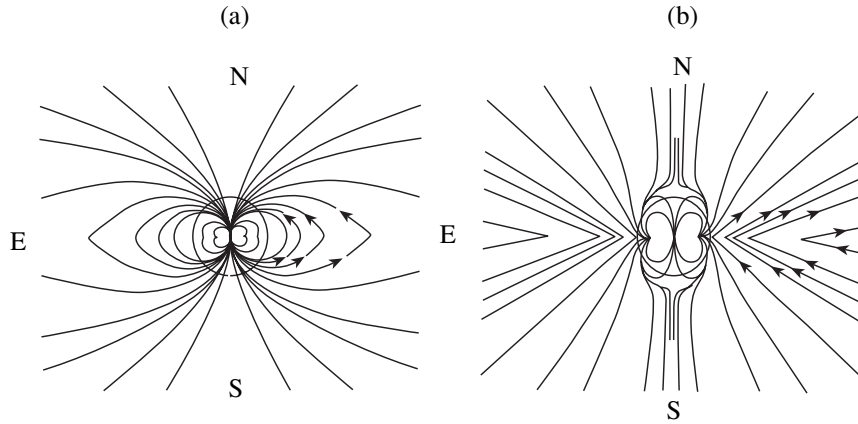* E-mail address for contacts: moloden@izmiran.ru

Fig. 1. Magnetic-field configuration for (a) $M/q > 0$ and (b) $M/q < 0$.

$$B_r = q\frac{\tanh x}{r^2} + 2M\frac{x}{r^3 k}, \quad B_\theta = \frac{M\sin\theta}{r^3}, \quad x = k\cos\theta. \tag{2}$$

$$j = j_\varphi = \frac{C}{4\pi}\frac{qk}{r^3}\frac{\sin\theta}{\cosh^2 x}. \tag{3}$$

At $k \gg 1$, the first term in B_r is $\pm\dfrac{q}{r^2}$ for $0 \leq \theta \leq \dfrac{\pi}{2}$ and $\dfrac{\pi}{2} \leq \theta \leq \pi$, respectively. For $\dfrac{M}{q} < 0$, there are two saddle points on the symmetry axis of the configuration at distance $|M/q|$ from the coordinate origin. Figure 1 shows two types of field-line configurations for $M/q > 0$ (Fig. 1a) and $M/q < 0$ (Fig. 1b).

Koutchmy *et al.* (1999) showed that the plasma density near the equatorial plane is higher than that in the surrounding corona for $M/q < 0$ and the density ratio is inverse for $M/q > 0$. Coronal observations suggest that the plasma density in the equatorial plane is higher than that in the surrounding corona (in any case, this is true for the quiescent corona). Thus, it should be concluded that $M/q < 0$ is real, and it will be used below.

Finally, note that the effect of the current emerging on the $B_r = 0$ surface in Eq. (2) is disregarded in the approximation under consideration. The equation of this new surface is

$$x^2 + y^2 + z^2 = -\frac{2M}{q}z, \tag{4}$$

where $x = r\sin\theta\cos\varphi$, $y = r\sin\theta\sin\varphi$, and $z = r\cos\theta$. The existence of such a surface and its possible role in producing polar plumes was discussed by Starkova *et al.* (1998).

STEADY-STATE PLASMA EXPANSION. GEOMETRIC PECULIARITIES OF THE EQUILIBRIUM FIELD

Below, we consider the expansion of plasma in the configuration shown in Fig. 1b for $M/q < 0$. The case with $M/q > 0$ corresponds to the configuration closed in the equatorial region, and we should set $v \equiv 0$ near the equator for it (see, e.g., Charbonneau and Hundhausen 1996). For $M/q < 0$, the situation is different.

Let us reproduce the Parker solution here. We will do this in order to introduce the necessary notation and to set the course of subsequent action. The equation of motion is

$$\rho v\frac{dv}{dr} + \frac{dp}{dr} + \rho g_\odot\frac{R^2}{r^2} = 0. \tag{5}$$

The plasma continuity condition and the equation of state with $T = \text{const}$ are

$$4\pi\rho v r^2 = \text{const}, \quad \rho = p\frac{m}{kT}. \tag{6}$$

It follows from (6) that

$$\ln p = \text{const} - \ln r^2 v + \ln v_c^2, \tag{7}$$

where $v_c^2 = \dfrac{kT}{m}$. Dividing Eq. (5) by ρ and eliminating the pressure using Eq. (7) yields

$$\frac{dv}{dr}\left(v - \frac{v_c^2}{v}\right) - \frac{2v_c^2}{r} + q\frac{R^2}{r^2} = 0. \tag{8}$$

For
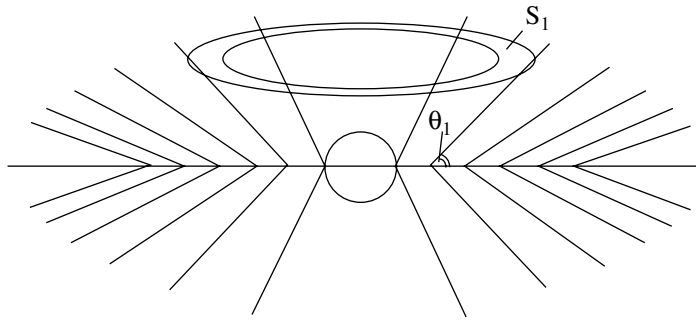
$$v = v_c, \quad r = r_c = \frac{gR^2}{2v_c^2} \tag{9}$$

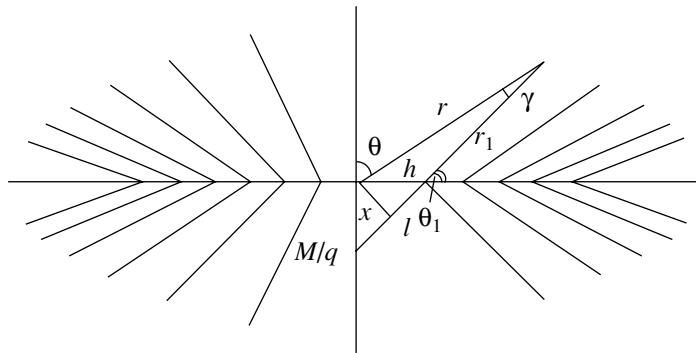**Fig. 2.** Conservation of the plasma flux through surface S_1 (see text).

Fig. 3. Relationship between coordinates r_1, θ_1 and spherical coordinates r, θ [see Eqs. (18)–(20)].

the derivative $\dfrac{dv}{dr}$ is indeterminate. This is a critical (saddle) point of Eq. (8). This equation is analytically integrable, and all its solutions can be constructed (Parker 1965).

Let us turn to the configuration described by Eqs. (1) and (2). Consider some of the geometric properties of field lines important for the subsequent analysis. We will show that near the equatorial line and for $r \gg h$, the field lines are nearly straight. For $k \gg 1$ [see Eqs. (1) and (2)], the equation of magnetic surfaces is

$$- r\cos\theta + \frac{M}{q}\left(\sin^2\theta - \frac{r}{h}\right) = 0, \qquad (10)$$

where h is the distance from the coordinate origin to the point of intersection of the field line with the equator. Introducing $z = r\cos\theta$ and $x = r\sin\theta$, we will have in the $y = 0$ plane

$$- z + \frac{M}{q}\left(\frac{x^2}{r^2} - \frac{r}{h}\right) = 0, \qquad (11)$$

differentiating Eq. (11) with respect to x for $z \longrightarrow 0$ and $x \longrightarrow r$ yields

$$\frac{dz}{dx} = -\frac{M}{qh}.$$

Hence, the equation of the family of straight lines near the equator is

$$z = -\frac{M}{qh}(x - h), \qquad (12)$$

which coincides with (11) for $r^2 \longrightarrow x^2$.

We also see from Eq. (10) that for $r \gg h$, Eq. (10) reduces to

$$\cos\theta = \frac{M}{qh}. \qquad (13)$$

This is the equation of the family of conic surfaces. A transition from one surface to another is made by changing the parameter h. The cone generatrices are straight lines.

It is convenient to introduce coordinates associated with the field lines (12): θ_1 is the angle that the field lines form with the equator and r_1 is the distance from the point of intersection to the current point (see Fig. 3). To write the plasma continuity condition in these coordinates requires determining the area of ring surface S_1 shown in Fig. 2. For this purpose, we will show that all

the straight lines described by Eq. (12) intersect at one point. Indeed, we add the equation of a close curve to Eq. (12):

$$z = \frac{M}{qh_1}(l - h_1), \quad h_1 \neq h. \qquad (14)$$

We derive from the condition of compatibility between Eqs. (12) and (14)

$$x = 0, \quad z = \frac{M}{q} \qquad (15)$$

the coordinates of the point of intersection. Designating $l = \sqrt{h^2 + \frac{M^2}{q^2}}$, we obtain the area $S_1 = 2\pi r \sin\theta(r_1 + l)d\theta_1$. Assuming that the field lines are straight and that the motion takes place only along the field lines, we write the continuity condition as

$$2\pi r \sin\theta\, v_1 (r_1 + l)\rho = \text{const.} \qquad (16)$$

The equation of motion includes $\frac{d}{dr_1} \ln\rho$, and this quantity can be expressed in terms of the geometric parameters by using the continuity equation. It follows from Eq. (16) that

$$\frac{d}{dr_1} \ln[2\pi(r_1 + l)r\sin\theta] = \frac{d}{dr_1}(r_1 + l) + \frac{\cos\theta_1}{h + r_1 \cos\theta_1}$$

$$= \frac{1}{r_1 + l} + \frac{1}{h/\cos\theta_1 + r_1} = \frac{2}{r_1 + l};$$

and the equation of motion takes the form

$$v_1 \frac{dv_1}{dr_1} + \frac{1}{\rho}\frac{dp}{dr_1} + g\frac{R^2}{r^2}\cos(\theta_1 - \theta) = 0, \qquad (17)$$

where v_1 is the plasma velocity along r_1.

In the last term of Eq. (17), r^2 must be replaced with r_1, h, θ_1. Obviously,

$$r\cos\theta = r_1 \sin\theta, \quad r\sin\theta = h + r_1 \cos\theta_1,$$

hence

$$r^2 = r_1^2 + h^2 + 2hr_1 \cos\theta_1. \qquad (18)$$

Together with the isothermality conditions, Eqs. (16)–(18) specify the equation of motion in the form (8):

$$\frac{dv_1}{dr_1}\left(v_1 - \frac{v_c^2}{v_1}\right) - v_c^2 \frac{d}{dr_1}\ln(r_1 + l)^2$$

$$+ g\frac{R^2}{r^2}\sin(\theta_1 + \theta) = 0. \qquad (19)$$

It is easy to see that $\sin(\theta_1 + \theta) = \cos\gamma$ (see Fig. 3), and

$$\cos\gamma = \frac{r_1 + l - x}{r}, \quad x = \left(\frac{M}{q}\right)^2\frac{1}{l},$$

$$l = \sqrt{\left(\frac{M}{q}\right)^2 + h^2}. \qquad (20)$$

Together with (9), relations (20) define all the quantities that appear in the equation of motion. The general integral of Eq. (19) can be written as

$$\frac{1}{2}v^2 - \ln v - 2\ln\frac{r_1 + l}{r_c} - 2\frac{r_c}{r} = \text{const}, \qquad (21)$$

where $v = \frac{v_1}{v_c}$, $r_c = \frac{gR^2}{2v_c^2}$.

ANALYSIS OF THE SOLUTION AND ESTIMATES

From integral (21), it is easy to pass to central symmetry by assuming that $M = 0$ and $h = 0$. Then, $l = 0$ and r_1 can be replaced with r using relation (18). We derive the general integral of the equation of motion for the case of central symmetry, in which the saddle points cover the $r = r_c$ spherical surface.

In the case of axial symmetry, however, the positions of the critical saddle points depend on r and θ. At the same time, those solutions for which the integral curves pass through the critical points are of interest as before.

At the critical point $v_1 = v_c$, it follows from Eq. (19) that $\frac{1}{r_1 + l} = \frac{r_c\cos\gamma}{r^2}$. Obviously, $\cos\gamma = 1$ and $r = r_1$ at the poles. Therefore, $r_1^2 = (r_1 + l)r_c$, whence $r_1 = \frac{1}{2}(r_c \pm \sqrt{r_c^2 + 4lr_c})$. Assuming that $l < r_c$, we obtain $r_1 = r_c + l$, $l \longrightarrow \left|\frac{M}{q}\right|$.

Substituting this value of r_1 in Eq. (21), we find the constant on the right-hand side of Eq. (21) for the integral curve passing through the critical point in the polar region. Assuming that $2l = r_c$, we derive

$$\text{const} = -\frac{3}{2} - 2\ln 2 = -2.88. \qquad (22)$$

Hence, at $r = 214R_\odot$, we obtain from Eq. (21)

$$v^2 = 4\ln\frac{r+l}{r_c} - 2.88 = 11.62, \qquad (23)$$

and $v_1 = 3.41 v_c = 436$ km s^{-1}.

The same operations performed for the equatorial regions lead to $v_1 = 461$ km s^{-1}.

The above numbers have a limited meaning. Indeed, v_c (1.28×10^7 cm s^{-1}) and r_c (4×10^{12} cm) appearing in Eq. (23) were determined for the temperature $T = 2 \times 10^6$ K. At the same time, in the model of an equilibrium heliospheric sheet by Koutchmy et al. (1999), the temperature decreases with distance (slightly faster than $1/r$), while the magnetic field lines near the equator emerge precisely from the heliospheric sheet. A consistent allowance for the temperature will cause Eqs. (16) and (17) to change, and the solution will be slightly different in form. However, Eq. (23) with the required temperature can be used for estimates. When the temperature decreases, the velocity near the equator also decreases ($v_t = 268$ km s^{-1} for $T = 10^6$ K); in such a situation, the position of the point of observation relative to the heliospheric sheet proves to be of greatest importance. Since the angle between the magnetic axis and the solar rotation axis at maximum solar activity can be large (see, e.g., Gulyaev 1994), field lines emerging either from the Sun or from the heliospheric sheet (with a lower temperature) can be near the Earth.

It should also be noted that the presence of coronal condensations on the Sun with an enhanced temperature in subpolar regions create conditions to assume $T > 2 \times 10^6$ K in Eq. (23). The same is true of chromospheric flares or subflares, which exist virtually always.

A natural constraint of the model is the condition that the critical point (whose position depends on temperature) lies above the solar surface. Taking $r_c \geq R_\odot$, we obtain from Eq. (21) $v_c \leq 300$ km s^{-1}, $T \leq 1.1 \times 10^7$ K, and $v \leq 1280$ km s^{-1}, which should apparently be considered as upper limits for the model parameters. As we see from the aforesaid, there is virtually no lower limit for the velocity.

The Ulysses observations (Marsden 1995a–1995c) show that the solar-wind velocity reduced to a distance of 1 AU is 400–450 km s^{-1} on the equator and 750–800 km s^{-1} in the polar regions. Both values are within the above limits, but with an addition that sources with a higher temperature than in the surrounding corona are important in high-latitude regions.

(1) The stationarity condition used in the equation of motion (17) assumes the constancy of all the quantities appearing in it with time. At the same time, we know the phenomena called *coronal mass ejections* which are accompanied by rapid changes in the distributions of density, velocity, and other parameters at each coronal point (halo-type mass ejection) or at position angles $p < 180°$. The stationarity condition used above is not applicable to these phenomena. However, mass ejec-

tions occur sporadically, at highly irregular intervals, and with a frequency of about one event in several days. During the remaining time, a static (or, more precisely, stationary) pattern with an almost immovable streamer structure is observed. Our analysis refers to such a situation.

(2) As follows from the above discussion, part of the solar wind in the model under consideration originates from the photosphere, while the other part originates from the heliospheric sheet.

As for the former, there is no doubt that its stationarity can hold, because the "store" of matter in the photosphere is virtually infinite with respect to the solar wind.

The situation with the heliospheric sheet is slightly different. In principle, it would be well to consider the formation mechanism of the heliospheric sheet (i.e., to eliminate the conditions $\frac{\partial}{\partial t}$ in advance and to solve a complete time-dependent problem) in order to solve the stationarity problem completely. However, this has not yet been done. Only several attempts to solve this problem are known (see, e.g., Linker and van Hoven 1990).

Let us now make the following estimate. Based on the solar-wind flux near the Earth ($nv = 3 \times 10^8$ cm^{-2} s^{-1}), let us calculate the time in which the heliospheric sheet with initial density $n_1 = 10^9$ cm^{-3} will be "exhausted." Obviously, $nvr^2 = n_1 v_1 R^2$. Therefore, $n_1 v_1 = 1.4 \times 10^{13}$ cm^{-2} s^{-1}. For $n_1 = 10^9$ cm^{-3}, we obtain the velocity in the corona $v_t = 0.1$ km s^{-1}. Assuming the scale height in the corona to be $h = 2 \times 10^{10}$ cm, we find the time $h/v_t = 2 \times 10^6$ s = 20 days. In other words, imagine that starting from some time, the corona would go into the solar wind without replenishment. Appreciable changes would occur in ~20 days. This time is longer than the CME rate. Therefore, we can imagine a complete "restructuring" of the entire corona with the heliospheric sheet once every two or three days and a static (or stationary) structure of the heliospheric-sheet plasma in between.

CONCLUSION

The model of a heliospheric sheet with $\frac{M}{q} < 0$ is similar to the model of quiescent filaments by Kippenhahn and Schlutter (1957). The need for this model arose, because a thin heliospheric sheet with an enhanced plasma density turned out to excellently explain the principal features of coronal structures (such as streamers, helmets, etc.). The question of how the equilibrium of relatively dense plasma of the heliospheric sheet in magnetic and gravitational fields is realized can apparently be considered solved (Koutchmy et al. 1999).

On the other hand, the peculiarities of an axially symmetric plasma configuration of the heliospheric

sheet raise the question of whether the solar-wind parameters depend on heliographic latitude. At present, this is one of the most topical questions in connection with the launches of spacecraft whose trajectories lie outside the ecliptic plane.

Clearly, the reliability of solving the corresponding questions significantly differs from the questions of the structure of the corona, a directly observable object. The necessity of recalculating the solar-wind parameters from a distance of ~1 AU (or ~5 AU, as is the case for Ulysses) to 1 $R_\odot$ contains a sufficient number of uncertainties. Therefore, the requirements for the theory of the corresponding objects are also different.

Our goal was to solve the equations of a stationary solar wind for the corresponding model. The currently available data were shown to be consistent with the model.

ACKNOWLEDGMENTS

REFERENCES

1. P. Charbonneau and A. I. Hundhausen, Sol. Phys. **165**, 237 (1996).

2. R. A. Gulyaev, Astrophys. J. **437**, 867 (1994).

3. R. Kippenhahn and A. Schlutter, Z. Astrophys. **43**, 36 (1957).

4. S. Koutchmy, M. M. Molodensky, and J.-C. Vial, Astron. Zh. **71**, 925 (1994) [Astron. Rep. **38**, 822 (1994)].

5. S. Koutchmy, M. M. Molodensky, L. I. Starkova, *et al.*, *Total Solar Eclipse of November 3, 1994*, in Revista de la Academia Nacional de Ciencial de Bolivia, No. 69, 60 (1995).

6. S. L. Koutchmy, M. M. Molodensky, O. T. Matsuura, and E. Picazzio, Pis'ma Astron. Zh. **25**, 308 (1999) [Astron. Lett. **25**, 258 (1999)].

7. I. A. Linker and G. van Hoven, Geophys. Res. Lett. **17**, 2281 (1990).

8. R. Marsden, International Heliospheric Study, Newsletters **9**, 27 (1995a).

9. R. Marsden, Space Sci. Rev. **72**, 1 (1995b).

10. R. Marsden, Science **268**, 1005 (1995c).

11. M. M. Molodensky, L. I. Starkova, S. Koutchmy, and A. V. Ershov, Astron. Soc. Pac. Conf. Ser. **95**, 385 (1996).

12. E. N. Parker, *Interplanetary Dynamical Processes* (Interscience, New York, 1963; Mir, Moscow, 1965).

13. L. Starkova, M. Molodensky, V. Koutvitsky, and S. Koutchmy, in *Proceedings of the International Meeting on Solar Jets and Coronal Plumes*, Ed. by Tan-Duc Guyenn, 1998, p. 317.

14. A. A. Vedenov, V. A. Koutvitsky, S. Koutchmy, *et al.*, Astron. Zh. **77**, 134 (2000) [Astron. Rep. **44**, 112 (2000)].

Translated by G. Rudnitskiǐ

Self-Excitation of Motions in Near-Convection Zones and the Generation of Solar Magnetic Field

Yu. V. Vandakurov*

Ioffe Physical-Technical Institute, Russian Academy of Sciences, Politekhnicheskaya ul. 26, St. Petersburg, 194021 Russia
Received March 28, 2001

Abstract—In view of the recently discovered time variations in rotation velocity within the solar differentially rotating tachocline (Howe *et al.* 2000), we study conditions for the equilibrium and excitation of motions in nonrigidly rotating magnetized layers of the radiative zones located near the boundaries of the convection zone. The emphasis is on the possible relationship between quasi-periodic tachocline pulsations and the generation of a nonaxisymmetric magnetic field in the convection zone. This field generation is studied under the assumption that it results from a reduction in the expenditure of energy on convective heat transport. The (antisymmetric about the equator) field is shown to increase in strength if there are both a radial gradient in angular velocity and steady-state axisymmetric meridional circulation of matter. The sense of circulation is assumed to change (causing the sign of the generated field to change) after the maximum permissible field strength is reached. This is apparently attributable to the excitation of the corresponding turbulent viscosity of the medium. It is also important that the cyclic field variations under discussion are accompanied by variations in solar-type dipole magnetic field. © *2001 MAIK "Nauka/Interperiodica"*.

Key words: *Sun, magnetic field, convection, pulsations*

1. INTRODUCTION

The latest helioseismic studies by Howe *et al.* (2000) have revealed nonstrictly periodic pulsations of the rotation velocity in several portions of the solar differentially rotating tachocline. The most pronounced rotation pulsations with a characteristic period of ~1.3 years are observed near the equator at relative radii $r/R_{\odot} \approx 0.63$ and 0.72. Here, the pulsation amplitude of the rotation velocity reaches 1.3%. The motions at a latitude of about 60° at $r/R_{\odot} \approx 0.63$ are slightly more chaotic, with the amplitude of the velocity variations being almost twice that quoted above.

The pulsations under discussion are of great interest for solar physics. For example, they can significantly speed up the lithium burning in the solar convection zone. The possible relationship of these pulsational motions with solar activity also needs elucidation. The hypothesis about the presence of instability that maintains pulsations of the medium runs into an obvious difficulty because of the necessity of its long existence. Accordingly, the assumption that some equilibrium conditions may not be satisfied seems promising.

It is well known that the condition of thermal equilibrium in stellar radiative zones can be satisfied only through the excitation of Eddington-Sweet meridional circulation of matter. The current status of the problem

was discussed, for example, by Tassoul (1982). In zones with sharp gradients in rotation velocity or in magnetized layers, the circulation velocity can increase. Below, we study this problem by representing all linear and nonlinear vector fields as expansions in terms of a complete system of orthogonal vector spherical harmonics (Vandakurov 1999a), allowing the radial and angular variables in the general nonlinear equations to be separated in terms of exact relations. In this case, we obtain a system of infinite equations for the radius- and time-dependent coefficients of the expansions in terms of vector harmonics mentioned above. It is important that our approach to the problem allows those components of various linear and nonlinear forces that interact with each other to be accurately taken into account. Of great interest are also configurations described by finite series of the vector harmonics mentioned above (see Vandakurov 2001a, 2001c). In particular, rigidly rotating models and models with a dipole magnetic field belong to this type of configurations.

Since the rotation distribution observed in the solar tachocline differs markedly from rigid rotation, it is unlikely that the condition of mechanical equilibrium can be satisfied in a nonmagnetic case. This conclusion is confirmed by the data given below. The hypothesis about the presence of a horizontal magnetic field in the tachocline was also discussed by Gilman (2000). Note that for the nonaxisymmetric toroidal magnetic field described by the series of vector harmonics mentioned

---

* E-mail address for contacts: yv.mhd@pop.ioffe.rssi.ru

above, there is generally a meridional field component. In that case, a strong radial electric field emerges in a rotating medium; as a result, a steady state is much more difficult to achieve. Accordingly, in section 5, we consider a model of a tachocline with an axisymmetric and antisymmetric (about the equator) toroidal magnetic field, which, as we will see below, can effectively interact with the cyclically varying dipole magnetic field when motions of the medium are excited. The latter field is known to play an important role in the solar cycle.

Our objective is to study simple equilibrium models of the solar magnetized tachocline and the properties of those motions that can be excited near the boundaries of the solar convection zone (see sections 2–5). In particular, we analyze the equilibrium in a rotating magnetized radiative zone assuming that the structure is almost convectively neutral (section 5). For the lower boundary of the solar convection zone, of particular interest are the boundary motions, which could have bearing on the solar cycle. It has recently been hypothesized (Vandakurov 1999b) that solar activity exists because of the formation of the state with the smallest expenditure of energy on convective heat transport. In this case, the conversion of thermal energy into magnetic energy is assumed to assist in reducing the expenditure of energy mentioned above.

Thus, whether magnetic-field generation is possible on condition that interactions between the large-scale velocity and field vectors play a major role is a fundamental question. According to Krause and Raedler (1980), there is reason to suppose that spherical dynamos associated with meridional circulation exist; these are modifications of the type of dynamo proposed by Gailitis (1970). In this case, fluctuational motions are of no importance, and only nonaxisymmetric magnetic fields can be generated. Note that Gailitis studied the field generation by a system of two stationary axisymmetric ring vortices.

In section 6, we analyze one of such nonviscous interactions between a nonaxisymmetric, mainly toroidal field and symmetric (about the equator) distributions of rotation and circulation assuming that the types of field symmetry and circulation are opposite to each other. For a stationary velocity field, the field grows if there are both a radial gradient in angular velocity and the circulation corresponding to the slow rise or sinking of matter near the equator and to its motion in the reverse direction at high latitudes. Note also that the change in poloidal-velocity direction causes the sign of the above growing field, which depends on azimuthal angle φ as $\sin\varphi$ or $\cos\varphi$, to change.

Since there is a radial motion of matter for the described model, a coupling between layers at different depths arises. What is the role of the motions in the tachocline in the entire process of solar magnetic field generation? Are there arguments for the fact that the pattern of increase in field amplitude described above is

actually realized on the Sun? These questions, which are of importance for the entire problem of solar activity, are considered below in the final section.

2. BASIC EQUATIONS

In the approximation of an inviscid medium and comparatively fast motions, for which heat exchange is insignificant, we have the following equations of motion, induction, energy, and continuity:

$$
\frac{\partial \mathbf{v}}{\partial t} + \frac{1}{2}\nabla(\mathbf{v}\cdot\mathbf{v}) + (\mathrm{curl}\,\mathbf{v})\times\mathbf{v}
$$
$$
- \frac{1}{4\pi\rho}(\mathrm{curl}\,\mathbf{B})\times\mathbf{B} + \frac{1}{\rho}\nabla p + \frac{1}{\rho}\nabla p + \nabla\Phi = 0, \tag{1}
$$

$$
\frac{\partial \mathbf{B}}{\partial t} = \mathrm{curl}(\mathbf{v}\times\mathbf{B}), \tag{2}
$$

$$
\frac{\partial}{\partial t}(p\rho^{-\gamma}) + (\mathbf{v}\cdot\nabla)(p\rho^{-\gamma}) = 0, \tag{3}
$$

$$
\frac{\partial\rho}{\partial t} + \mathrm{div}(\rho\mathbf{v}) = 0, \tag{4}
$$

where $\mathbf{v}$ is the hydrodynamic velocity, $\mathbf{B}$ is the magnetic field, p is the pressure, ρ is the density, $\gamma = \mathrm{const}$ is the adiabatic index, and Φ is the gravitational potential. The Poisson equation for Φ should also be added to Eqs. (1)–(4). Below, we assume that the density in the expression for magnetic force and in the second term of Eq. (4) can be roughly treated as spherically symmetric.

Applying the curl operation to the equation of motion (1) yields

$$
\frac{\partial}{\partial t}\mathrm{curl}\,\mathbf{v} + \mathbf{R} + \frac{\nabla p\times\nabla\rho}{\rho^2} = 0, \tag{5}
$$

where

$$
\mathbf{R} = \mathrm{curl}\left[(\mathrm{curl}\,\mathbf{v})\times\mathbf{v} - \frac{1}{4\pi\rho}(\mathrm{curl}\,\mathbf{B})\times\mathbf{B}\right]. \tag{6}
$$

We represent all vector (or scalar) quantities as expansions in terms of a complete system of orthogonal vector spherical harmonics $\mathbf{Y}_{JM}^{(\lambda)}$ (or spherical functions Y_{JM}), which are functions of angular coordinates. Here, the superscript is $\lambda = 0$ or ± 1, the first subscript J is a nonnegative integer, and the azimuthal number M for axisymmetric modes is zero. Note that the harmonic $\mathbf{Y}_{JM}^{(\lambda)}$ can be expressed in terms of Y_{JM} (see, e.g., Vandakurov 1999a, 2001a). The expansion coefficients are $v_{JM}^{(\lambda)}$, $B_{JM}^{(\lambda)}$, p_{JM}, etc. These quantities depend on r and t, with r, ϑ, and φ forming a spherical coordinate system with unit vectors $\mathbf{i}_r$, $\mathbf{i}_\vartheta$, and $\mathbf{i}_\varphi$. Note that $\lambda = 0$ and $\lambda = \pm 1$ correspond to the toroidal and poloidal components, respectively. Below, we consider the axisymmetric and nonaxisymmetric models separately.

3. AXIAL SYMMETRY

The equations for the above expansion coefficients including all nonlinear forces have been considered previously (Vandakurov 1999a, 2001a). They are cumbersome in general form. Given that the most complex processes of interaction between various forces take place in the tachocline zone and that this zone most likely has a nearly axisymmetric structure, let us first consider the equations for models with this symmetry. In this case, the azimuthal number M is zero.

It is appropriate to use Eq. (5) for the toroidal component $(\mathrm{rot}\,\mathbf{v})_{J0}^{(0)} = (i/r)w_{J0}$ instead of the equation for the component $v_{J0}^{(+1)}$ in Eq. (1). In addition, we ignore corrections that are quadratic in the poloidal components of the velocity and field vectors. In this approximation, the problem of solving the multi-dimensional system of equations (1)–(5) reduces to solving the following equations for the r- and t-dependent coefficients under discussion:

$$
\frac{\partial}{\partial t} v_{J0}^{(-1)} + \frac{1}{2r}\left[\frac{J(J+1)}{2J+1}\right]^{1/2}
$$

$$
\times \sum_{J_1 J_2} G_{J_1 0 J_2 0}^{J0} Z_{J_1 J_2}^{J}\left[v_{J_1 0}^{(0)} v_{J_2 0}^{(0)} - \frac{1}{8\pi\rho r}\frac{\partial}{\partial r} r^2 B_{J_1 0}^{(0)} B_{J_2 0}^{(0)}\right]
$$

$$
+ \frac{1}{\rho^2}\sum_{J_1 J_2}(C_{J_1 0 J_2 0}^{J0})^2\left[\frac{(2J_1+1)(2J_2+1)}{4\pi(2J+1)}\right]^{1/2} \tag{7}
$$

$$
\times \rho_{J_2 0}\frac{\partial}{\partial r}p_{J_1 0} + \frac{\partial}{\partial r}\Phi_{J0} = 0,
$$

$$
\frac{\partial}{\partial t}w_{J0} - \frac{\zeta_J}{4r}\sum_{J_1 J_2} G_{J_1 0 J_2 0}^{J0}
$$

$$
\times \left\{ X_{J_1 J_2}^{J} r\frac{\partial}{\partial r}\left(v_{J_1 0}^{(0)} v_{J_2 0}^{(0)} - \frac{1}{4\pi\rho}B_{J_1 0}^{(0)} B_{J_2 0}^{(0)}\right)\right.
$$

$$
+ J(J+1)Z_{J_1 J_2}^{J}\frac{1}{r}\left[\frac{\partial}{\partial r}(r^2 v_{J_1 0}^{(0)} v_{J_2 0}^{(0)})\right.
$$

$$
\left. - \frac{1}{4\pi\rho}\frac{\partial}{\partial r}(r^2 B_{J_1 0}^{(0)} B_{J_2 0}^{(0)})\right] - \frac{2r}{\rho^2}I_{J_1}I_{J_2}\left[Z_{JJ_2}^{J_1}\rho_{J_2 0}\frac{\partial}{\partial r}p_{J_1 0}\right. \tag{8}
$$

$$
\left.\left. - Z_{JJ_1}^{J_2} p_{J_1 0}\frac{\partial}{\partial r}\rho_{J_2 0}\right]\right\} = 0,
$$

$$
J > 0,
$$

$$
\frac{\partial}{\partial t}v_{J0}^{(0)} + \frac{\zeta_J}{2r}\sum_{J_1 J_2} G_{J_1 0 J_2 0}^{J0}\left\{ I_{J_2}Z_{JJ_1}^{J_2}\left[v_{J_2 0}^{(-1)}\frac{\partial}{\partial r}r v_{J_1 0}^{(0)}\right.\right.
$$

$$
\left. - \frac{1}{4\pi\rho}B_{J_2 0}^{(-1)}\frac{\partial}{\partial r}r B_{J_1 0}^{(0)}\right] - J_1(J_1+1)Z_{JJ_2}^{J_1}
$$

$$
\times \left[v_{J_1 0}^{(0)} v_{J_2 0}^{(+1)} - \frac{1}{4\pi\rho}B_{J_1 0}^{(0)} B_{J_2 0}^{(+1)}\right]\right\} = 0, \tag{9}
$$

$$
J > 0,
$$

$$
\frac{\partial}{\partial t}B_{J0}^{(0)} - \frac{\zeta_J}{2r}\sum_{J_1 J_2} G_{J_1 0 J_2 0}^{J0}\left\{ \frac{\partial}{\partial r}r[I_{J_2}Z_{JJ_1}^{J_2} v_{J_1 0}^{(0)} B_{J_2 0}^{(-1)}\right.
$$

$$
- I_{J_1}Z_{JJ_2}^{J_1} v_{J_1 0}^{(-1)} B_{J_2 0}^{(0)}] + J(J+1)Z_{J_1 J_2}^{J}
$$

$$
\times [v_{J_1 0}^{(0)} B_{J_2 0}^{(+1)} - v_{J_1 0}^{(+1)} B_{J_2 0}^{(0)}]\bigg\} = 0, \tag{10}
$$

$$
J > 0,
$$

$$
\frac{\partial}{\partial t}B_{J0}^{(-1)} - \frac{1}{2r}\left[\frac{J(J+1)}{2J+1}\right]^{1/2}
$$

$$
\times \sum_{J_1 J_2} G_{J_1 0 J_2 0}^{J0}[I_{J_2}Z_{JJ_1}^{J_2} v_{J_1 0}^{(+1)} B_{J_2 0}^{(-1)}
$$

$$
- I_{J_1}Z_{JJ_2}^{J_1} v_{J_1 0}^{(-1)} B_{J_2 0}^{(+1)}] = 0, \tag{11}
$$

$$
J > 0,
$$

$$
\frac{\partial}{\partial t}p_{J0} - \frac{\gamma p}{\rho}\frac{\partial}{\partial t}\rho_{J0} + \frac{1}{2r}\left[\frac{J(J+1)}{2J+1}\right]^{1/2}
$$

$$
\times \sum_{J_1 J_2} G_{J_1 0 J_2 0}^{J0} I_{J_2}\left[Z_{J_1 J_2}^{J} v_{J_1 0}^{(+1)}\left(p_{J_2 0} - \frac{\gamma p}{\rho}\rho_{J_2 0}\right)\right. \tag{12}
$$

$$
\left. + 2I_{J_1} v_{J_1 0}^{(-1)} r\left(\frac{\partial}{\partial r}p_{J_2 0} - \frac{\gamma p}{\rho}\frac{\partial}{\partial r}\rho_{J_2 0}\right)\right] = 0,
$$

$$
\frac{\partial}{\partial t}\rho + \frac{1}{r^2}\frac{\partial}{\partial r}r^2\rho\, v_{J0}^{(-1)} - I_J\frac{\rho}{r}v_{J0}^{(+1)} = 0, \tag{13}
$$

where

$$
w_{J0} = \frac{\partial}{\partial r}r v_{J0}^{(+1)} - I_J v_{J0}^{(-1)}, \quad J > 0, \tag{14}
$$

$$
G_{J_1 0 J_2 0}^{J0} = (C_{J_1 0 J_2 0}^{J0})^2\frac{[(2J_1+1)(2J_2+1)]^{1/2}}{2\pi^{1/2}I_J I_{J_1} I_{J_2}}, \tag{15}
$$

$$
X_{ab}^{c} = a(a+1)Z_{bc}^{a} + b(b+1)Z_{ac}^{b}, \tag{16}
$$

$$
Z_{ab}^{c} = a(a+1) + b(b+1) - c(c+1), \tag{17}
$$

here, $\zeta_a = (2a+1)^{-1/2}$, $I_a = [a(a+1)]^{1/2}$, and C_{a0b0}^{c0} is the Clebsch–Gordan coefficient. Of course, the coefficients

Φ_{J0} can be expressed in terms of ρ_{J0} using the Poisson equation

$$\frac{1}{r^2}\frac{\partial}{\partial r}r^2\frac{\partial}{\partial r}\Phi_{J0} - \frac{J(J+1)}{r^2}\Phi_{J0} = 4\pi G\rho_{J0}. \qquad (18)$$

Here, G is the gravitational constant. In view of the equation div $\mathbf{B} = 0$, we have

$$B_{J0}^{(+1)} = \frac{1}{rI_J}\frac{\partial}{\partial r}(r^2 B_{J0}^{(-1)}). \qquad (19)$$

For a zero subscript J, singularities may appear in the above equations, which can be resolved by using relations from Vandakurov (1999a). Note also that in the above equations and below, the corresponding spherically symmetric distributions are denoted by p and ρ; the zero coefficient is $p_{00} = (4\pi)^{1/2}p$ and the like.

4. TRANSFORMATION OF EQUATIONS

The serious difficulties that arise when solving the system of equations (7)–(13) are attributable to the large number of equations in the presence of high-order modes. In simple models, only the lowest order modes play a major role. For example, in our models of differential rotation (Vandakurov 1999b, 2001a), the rotation was nearly solar when the first term was principal in the expression for the rotation velocity; the subscript J of coefficients $v_{J0}^{(0)}$ was odd, and the first ratio of the succeeding coefficient to the preceding one, $v_{30}^{(0)}/v_{10}^{(0)}$, was of the order of 1/20. The other ratios of this kind were also small. Therefore, the solar rotation can be studied in the first approximation by retaining only two principal coefficients in the expansions for the main toroidal field components. As will be seen from our subsequent analysis, the small poloidal components can also be significant. In the expressions for the latter, we will retain only one lowest order term.

Taking into account the observational data, we assume that the velocity field is symmetric and that the magnetic field is antisymmetric about the equatorial plane. Including also the possible general expansion or compression of the medium for generality, we represent the vector fields under consideration as follows:

$$\mathbf{v} = \frac{1}{2(\pi)^{1/2}}\left\{\mathbf{i}_r v_{00}^{(-1)} + \frac{5^{1/2}}{2}\left[\mathbf{i}_r v_{20}^{(-1)}(3\cos^2\vartheta - 1)\right.\right.$$

$$\left.\left. -\mathbf{i}_\vartheta \frac{1}{2r\rho}\frac{\partial}{\partial r}(r^2\rho v_{20}^{(-1)})\sin 2\vartheta\right]\right\} \qquad (20)$$

$$+ \mathbf{i}_\varphi r\Omega_1\left[1 + u_3\left(\frac{7}{8}\right)^{1/2}(5\cos^2\vartheta - 1)\right]\sin\vartheta,$$

$$\mathbf{B} = \left(\frac{3}{4\pi}\right)^{1/2}\left[\mathbf{i}_r B_{10}^{(-1)}\cos\vartheta - \mathbf{i}_\vartheta\frac{1}{2r}\frac{\partial}{\partial r}(r^2 B_{10}^{(-1)})\sin\vartheta\right]$$
$$+ i\mathbf{i}_\varphi\frac{1}{4}\left(\frac{5}{\pi}\right)^{1/2}\left[\left(\frac{3}{2}\right)^{1/2}B_{20}^{(0)} - \frac{3}{4}B_{40}^{(0)}(3 - 7\cos^2\vartheta)\right]\sin 2\vartheta, \qquad (21)$$

where $\Omega_1 = i[3/(8\pi)]^{1/2}[v_{10}^{(0)}/r]$ is the angular velocity, which is described by the first term of the series for this velocity; and $u_3 = v_{30}^{(0)}/v_{10}^{(0)}$ is the ratio of the first two coefficients. All coefficients of the toroidal components are seen to be imaginary. The terms with $B_{10}^{(-1)}$ in Eq. (21) describe the dipole magnetic field.

Below, we use the following expressions for the numerical coefficients in the general equations: $G_{10J_20}^{J0} = \{3(J + J_2 + 1)/[8\pi J(J + 1)(2J_2 + 1)(3J_2 - J + 1)]\}^{1/2}(\delta_{J,J_2+1} + \delta_{J,J_2-1})$, $G_{1010}^{20} = (24\pi)^{-1/2}$, $G_{3020}^{10} = 3/[8(35\pi)^{1/2}]$, $G_{2020}^{20} = 5/[42(6\pi)^{1/2}]$, $G_{2040}^{20} = 1/[28(\pi)^{1/2}]$, $G_{2020}^{40} = 3/[28(5\pi)^{1/2}]$, $C_{2000}^{20} = 1$, $C_{2020}^{20} = -C_{2040}^{20} = -(2/7)^{1/2}$, and $C_{2020}^{40} = 3(2/35)^{1/2}$. Here, $\delta_{a,b} = 1$ if $a = b$ and $\delta_{a,b} = 0$ if a $a \neq b$.

All the equations mentioned above can be grouped together according to subscript J (irrespective of the parity of the latter), considering separately the equilibrium equations and the equations of oscillations about the equilibrium. For clarity, we nevertheless retain the terms with a time derivative in all equations. In addition, we restrict our analysis to slow motions, for which the time derivative of ρ_{J0} in the continuity equation (13) is negligible. From Eqs. (7)–(12), we then derive for the first group of equations

$$\frac{\partial}{\partial t}v_{00}^{(-1)} = -\frac{1}{2r(\pi)^{1/2}}\left[(v_{10}^{(0)})^2 - \frac{1}{8\pi\rho r}\frac{\partial}{\partial r}(rB_{20}^{(0)})^2\right]$$
$$-\frac{1}{\rho}\frac{\partial}{\partial r}p_{00} - \frac{\partial}{\partial r}\Phi_{00}, \qquad (22)$$

$$\frac{\partial}{\partial t}v_{20}^{(-1)} = \frac{1}{2r(5\pi)^{1/2}}\left\{v_{10}^{(0)}\left[v_{10}^{(0)} - 6\left(\frac{2}{7}\right)^{1/2}v_{30}^{(0)}\right]\right.$$

$$\left. + \frac{5}{56\pi\rho r}\frac{\partial}{\partial t}[r^2 B_{20}^{(0)}(B_{20}^{(0)} + 2(6)^{1/2}B_{40}^{(0)})]\right\} \qquad (23)$$

$$-\frac{1}{\rho}\left(\frac{\partial}{\partial r}p_{20} + \frac{\rho_{20}}{\rho}\frac{dp}{dr}\right) - \frac{\partial}{\partial r}\Phi_{20},$$

$$\frac{\partial}{\partial t}w_{20} = \frac{3^{1/2}}{(10\pi)^{1/2}}\left\{rv_{10}^{(0)}\frac{\partial}{\partial r}\left(\frac{v_{10}^{(0)}}{r}\right)\right.$$

$$+\left(\frac{8}{7}\right)^{1/2}\frac{1}{r^3}\frac{\partial}{\partial r}(r^3 v_{10}^{(0)} v_{30}^{(0)})$$

$$-\frac{5}{7}\frac{\partial}{\partial r}\left[\frac{1}{4\pi\rho}B_{20}^{(0)}(B_{20}^{(0)}-2(6)^{-1/2}B_{40}^{(0)})\right] \quad (24)$$

$$-\frac{5}{56\pi\rho r^2}\frac{\partial}{\partial r}[r^2 B_{20}^{(0)}(B_{20}^{(0)}+2(6)^{1/2}B_{40}^{(0)})]\Bigg\}$$

$$+\frac{6^{1/2}}{\rho^2}\left(p_{20}\frac{d\rho}{dr}-\rho_{20}\frac{dp}{dr}\right),$$

$$\frac{\partial}{\partial t}v_{40}^{(-1)} = -\frac{1}{28r^2\rho(\pi)^{3/2}}\frac{\partial}{\partial r}(rB_{20}^{(0)})^2$$

$$-\frac{1}{\rho^2}\left(\rho_{40}\frac{dp}{dr}+\rho\frac{\partial}{\partial r}p_{40}\right)-\frac{\partial}{\partial r}\Phi_{40},$$
(25)

$$\frac{\partial}{\partial t}w_{40}$$

$$=\frac{5^{1/2}}{14r^2\rho(\pi)^{3/2}}\left\{\frac{\partial}{\partial r}(rB_{20}^{(0)})^2-\frac{3r^2\rho}{2}\frac{\partial}{\partial r}\left[\frac{1}{\rho}(B_{20}^{(0)})^2\right]\right\}$$

$$+\frac{2(5)^{1/2}}{\rho^2}\left(\rho_{40}\frac{dp}{dr}-p_{40}\frac{d\rho}{dr}\right);$$
(26)

and for the second group of equations

$$\frac{\partial}{\partial t}p_{J0}-\frac{\gamma p}{\rho}\frac{\partial}{\partial t}\rho_{J0} = -v_{J0}^{(-1)}\left(\frac{dp}{dr}-\frac{\gamma p}{\rho}\frac{d\rho}{dr}\right)$$

$$-\frac{1-\delta_{J0}}{2\pi^{1/2}}v_{00}^{(-1)}\left(\frac{\partial}{\partial r}p_{J0}-\frac{\gamma p}{\rho}\frac{\partial}{\partial r}\rho_{J0}\right),$$
(27)

$$J = 0, 2, 4, \ldots,$$

$$\frac{\partial}{\partial t}v_{10}^{(0)}$$

$$=\frac{1}{2r^3\rho(5\pi)^{1/2}}\frac{\partial}{\partial r}\left[r^3\left(\rho v_{20}^{(-1)} v_{10}^{(0)}+\frac{3^{1/2}}{4\pi}B_{20}^{(0)}B_{10}^{(-1)}\right)\right],$$
(28)

$$\frac{\partial}{\partial t}v_{30}^{(0)} = -\frac{1}{r(70\pi)^{1/2}}\left\{3v_{20}^{(-1)}\frac{\partial}{\partial r}rv_{10}^{(0)}\right.$$

$$-\frac{2}{r\rho}v_{10}^{(0)}\frac{\partial}{\partial r}(r^2\rho v_{20}^{(-1)})$$
(29)

$$-\frac{3^{1/2}}{4\pi\rho}\left[2B_{10}^{(-1)}\frac{\partial}{\partial r}rB_{20}^{(0)}-\frac{3}{r}B_{20}^{(0)}\frac{\partial}{\partial r}r^2 B_{10}^{(-1)}\right]\Bigg\},$$

$$\frac{\partial}{\partial t}B_{20}^{(0)} = \frac{1}{2r(5\pi)^{1/2}}\left\{3^{1/2}r^2 B_{10}^{(-1)}\frac{\partial}{\partial r}\left(\frac{v_{10}^{(0)}}{r}\right)\right.$$

$$-\frac{5}{7}\left[\frac{\partial}{\partial r}(rv_{20}^{(-1)}B_{20}^{(0)})+\frac{1}{r\rho}B_{20}^{(0)}\frac{\partial}{\partial r}(r^2\rho v_{20}^{(-1)})\right]\Bigg\},$$
(30)

$$\frac{\partial}{\partial t}B_{40}^{(0)} = -\frac{1}{7r}\left(\frac{15}{2\pi}\right)^{1/2}\left[\frac{\partial}{\partial r}(rv_{20}^{(-1)}B_{20}^{(0)})\right.$$

$$-\frac{4}{3r\rho}B_{20}^{(0)}\frac{\partial}{\partial r}(r^2\rho v_{20}^{(-1)})\Bigg],$$
(31)

$$\frac{\partial}{\partial t}B_{10}^{(-1)} = \frac{1}{r^4\rho(20\pi)^{1/2}}\frac{\partial}{\partial r}[r^4\rho v_{20}^{(-1)}B_{10}^{(-1)}], \quad (32)$$

where

$$w_{J0} = [J(J+1)]^{-1/2}\frac{\partial}{\partial r}\frac{1}{\rho}\frac{\partial}{\partial r}(r^2\rho v_{J0}^{(-1)})$$

$$-[J(J+1)]^{1/2}v_{J0}^{(-1)}.$$
(33)

Here, only the principal terms were retained in the equations for the modes of the highest order of smallness. Actually, the spherically symmetric coefficient v_{00} is small, and all terms with this coefficient have the second order of smallness; in the approximation under consideration, these terms should be discarded.

In general, the above equations allow the behavior of the principal modes that determine the equilibrium or motion of the medium to be studied. The presence of correction terms with $v_{30}^{(0)}$ and $B_{40}^{(0)}$ in the equilibrium equations (23) and (24) proves to be important (even if these corrections are small), because the right-hand parts in Eqs. (28)-(29) or in similar equations (30)–(31) are equal in order of magnitude. This effect is unrelated to the corrections of a higher order of smallness if the poloidal components are described by the coefficients $v_{20}^{(-1)}$ and $B_{10}^{(-1)}$ alone. In other words, during the excitation of motions, the latitudinal structure of the field and rotation distributions significantly changes, which appreciably affects the general motion of the medium. It is worthwhile analyzing such changes using the equations derived by differentiating the equilibrium equations (23)–(24) with respect to time. This procedure allows the correction terms mentioned above to be eliminated in the first approximation. As a result, we obtain

$$\frac{\partial^2}{\partial t^2}v_{20}^{(-1)} = \frac{1}{10r^2\pi}\left\{\frac{1}{r^2\rho}v_{10}^{(0)}\left[\frac{\partial}{\partial r}r^3\left(\rho v_{10}^{(0)}v_{20}^{(-1)}\right.\right.\right.$$

$$+ \frac{3^{1/2}}{4\pi} B_{20}^{(0)} B_{10}^{(-1)} \Big) \Big] + \frac{5}{56\pi\rho} \frac{\partial}{\partial r} r \Big[3^{1/2} r^2 B_{20}^{(0)} B_{10}^{(-1)} \frac{\partial}{\partial r} \Big(\frac{v_{10}^{(0)}}{r} \Big)$$

$$- \frac{5}{7}(H_1 + 6H_2) \Big] + \frac{6}{7}(\Psi_v - \Psi_b) \Big\} \qquad (34)$$

$$- \frac{1}{\rho} \Big[\frac{\partial}{\partial t} \frac{\partial p_{20}}{\partial r} + \frac{1}{\rho} \frac{dp}{dr} \frac{\partial \rho_{20}}{\partial t} \Big] - \frac{\partial}{\partial r} \frac{\partial \Phi_{20}}{\partial t},$$

$$\frac{\partial^2}{\partial t^2} w_{20} = \frac{1}{5\pi} \Big(\frac{3}{2} \Big)^{1/2} \Big\{ \frac{r^2}{2} \frac{\partial}{\partial r}$$

$$\times \Big[\frac{1}{r^5 \rho} v_{10}^{(0)} \frac{\partial}{\partial r} r^3 \Big(\rho v_{10}^{(0)} v_{20}^{(-1)} + \frac{3^{1/2}}{4\pi} B_{20}^{(0)} B_{10}^{(-1)} \Big) \Big]$$

$$- \frac{5(3)^{1/2}}{28\pi} \Big[\frac{\partial}{\partial r} \frac{r}{\rho} B_{20}^{(0)} B_{10}^{(-1)} \frac{\partial}{\partial r} \Big(\frac{v_{10}^{(0)}}{r} \Big)$$

$$+ \frac{1}{2r^2\rho} \frac{\partial}{\partial r} r^3 B_{20}^{(0)} B_{10}^{(-1)} \frac{\partial}{\partial r} \Big(\frac{v_{10}^{(0)}}{r} \Big) \Big] \qquad (35)$$

$$- \frac{2}{7r^3} \frac{\partial}{\partial r} r^2 (\Psi_v - \Psi_b) + \frac{1}{4\pi} \Big(\frac{5}{7} \Big)^2$$

$$\times \Big[\frac{\partial}{\partial r} \frac{1}{r\rho} (H_1 - H_2) + \frac{1}{2r^2\rho} \frac{\partial}{\partial r} r(H_1 + 6H_2) \Big] \Big\}$$

$$- \frac{6^{1/2}}{\rho^2} \Big(\frac{dp}{dr} - \frac{\gamma p}{\rho} \frac{d\rho}{dr} \Big) \Big(\frac{\partial}{\partial t} \rho_{20} + v_{20}^{(-1)} \frac{d\rho}{dr} \Big),$$

where

$$H_k = B_{20}^{(0)} \Big[\frac{\partial}{\partial r} (r v_{20}^{(-1)} B_{20}^{(0)}) + \frac{a_k}{r\rho} B_{20}^{(0)} \frac{\partial}{\partial r} (r^2 \rho v_{20}^{(-1)}) \Big], (36)$$

$$\Psi_v = v_{10}^{(0)} \Big[3 v_{20}^{(-1)} \frac{\partial}{\partial r} r v_{10}^{(0)} - \frac{2}{r\rho} v_{10}^{(0)} \frac{\partial}{\partial r} (r^2 \rho v_{20}^{(-1)}) \Big], (37)$$

$$\Psi_b = \frac{3^{1/2}}{4\pi\rho} v_{10}^{(0)} \Big[2 B_{10}^{(-1)} \frac{\partial}{\partial r} r B_{20}^{(0)} - \frac{3}{r} B_{20}^{(0)} \frac{\partial}{\partial r} r^2 B_{10}^{(-1)} \Big], (38)$$

with $a_1 = 1$, $a_2 = -4/3$, and $k = 1$ or 2.

5. POSSIBLE EQUILIBRIUM STRUCTURES

Let us first consider the problems associated with the satisfaction of equilibrium equations (22)–(26), in which the left-hand parts are negligible. For the steady-state rigid rotation of a nonmagnetic medium, $v_{10}^{(0)}/r = $ const and $[v_{J0}^{(0)}]_{J>1} = 0$. Eq. (22) takes the form

$$\frac{1}{\rho} \frac{\partial p}{\partial r} + \frac{\partial \Phi}{\partial r} = \frac{2}{3} r \Omega_1^2. \qquad (39)$$

In addition, Eq. (24) is satisfied if

$$p_{20}\rho' = \rho_{20}p', \qquad (40)$$

where the prime denotes a derivative with respect to r. Using Eqs. (18) and (39) and setting the right-hand part of Eq. (23) equal to zero, we obtain a system of three equations for p_{20}, ρ_{20}, and Φ_{20}. Since p_{20} and ρ_{20} are determinate, difficulties in satisfying the condition of thermal equilibrium will arise. Actually, the standard Eddington-Sweet meridional circulation will be excited. This problem was discussed in detail, for example, by Tassoul (1982).

If, however, the radial gradient in angular velocity is nonzero and if there is a toroidal magnetic field, then the additional variable $B_{20}^{(0)}$ can be used to satisfy Eqs. (23)–(24). This allows the condition of thermal equilibrium to be satisfied in the first approximation. Still, the conclusion that meridional circulation must be excited remains valid, because a similar situation arises when solving the system of equations (18), (25), and (26) for the higher order variables p_{40}, ρ_{40}, and Φ_{40}.

We restrict our analysis to the equilibrium state and to the possible slow unsteady flows in the radiative zone close to a convectively neutral zone, so that

$$p'/\gamma p - \rho'/\rho \approx 0, \qquad (41)$$

where the left-hand part is still positive. In this case, the last term in Eq. (35) and the right-hand part of Eq. (27) are insignificant. In addition, the difference $p_{20}\rho' - \rho_{20}p'$ in Eq. (24) remains approximately constant during the excitation of any motions. If unsteady, for example, quasi-periodic motions are involved, this difference should be set equal to zero; the last terms in Eqs. (24) and (35) can then be discarded. Actually, we derive the same relation (40) between corrections p_{20} and ρ_{20}, which holds for a rigidly rotating medium. Here, the corrections to pressure and density do not have to be stationary; only nonadiabatic time variations of the temperature distribution, which are unrelated to heat exchange in our approximation, are hampered. In particular, relation (40) must be satisfied if random small changes in equilibrium quantities occur in the medium. Under condition (40) and without small corrections being applied, Eq. (24) takes the form

$$\frac{\partial}{\partial t} w_{20} = \Big(\frac{3}{10\pi} \Big)^{1/2} \Big\{ r v_{10}^{(0)} \frac{\partial}{\partial r} \Big(\frac{v_{10}^{(0)}}{r} \Big)$$

$$- \frac{5}{7} \Big[\frac{\partial}{\partial r} \frac{1}{4\pi\rho} (B_{20}^{(0)})^2 + \frac{1}{8\pi\rho r^2} \frac{\partial}{\partial r} (r B_{20}^{(0)})^2 \Big] \Big\}. \qquad (42)$$

Here, the coefficients $v_{10}^{(0)}$ and $B_{20}^{(0)}$ are imaginary.
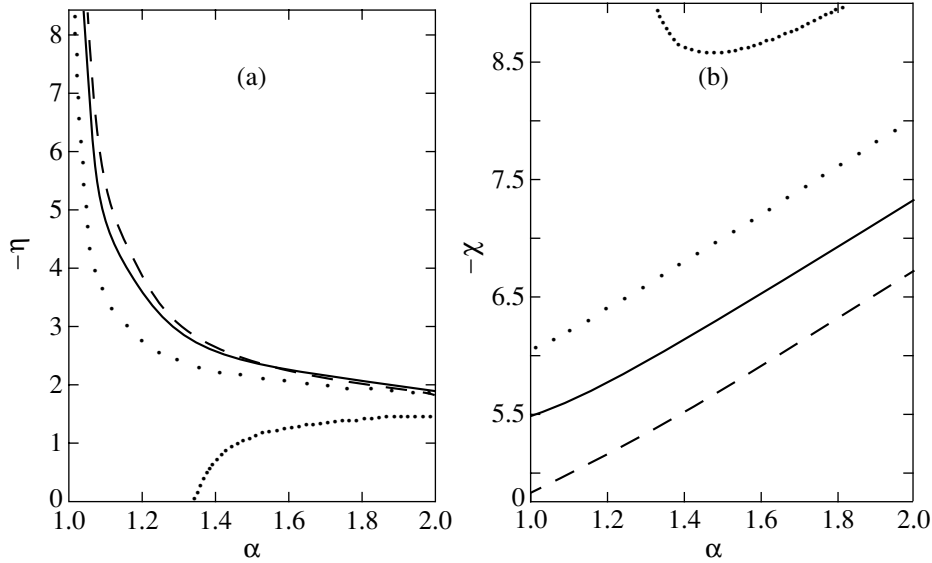
Parameters (a) η and (b) χ versus α for $s = 3, 5, 7$, and 10 (respectively, dashes, solid line, widely and narrowly spaced dots).

Since the inertial term in Eq. (42) is generally small, an important relation holds between the equilibrium Alfvén and rotation velocities. For example, if $v_{J0}^{(0)}$, $B_{J0}^{(0)}$, and ρ are proportional to r to the power of α, $\alpha - s/2$, and $-s$, respectively, then all terms in the equation under consideration will have the same dependence on radius, and we will obtain for the field

$$\frac{(B_{20}^{(0)})^2}{4\pi\rho} \approx \frac{7(\alpha - 1)}{5(3\alpha - s/2 + 1)}(v_{10}^{(0)})^2, \qquad (43)$$

where α and s are constant.

For the equatorial region of the solar tachocline, $\alpha \sim 1.5$; if the azimuthal velocity is ~ 2 km s^{-1}, $\rho \sim 0.2$ g cm^{-3}, and $s \approx 5$ [these values roughly correspond to the numerical data of Guenther *et al.* (1992)], we obtain $B_\varphi \approx 170$ kG for the maximum main azimuthal field (i.e., the Alfvén velocity accounts for 0.54 of the rotation velocity). We see from formula (21) that this field is zero on the equator and at the poles and reaches a maximum at latitude 45°. However, $s \gg 1$ for the radiative zone near the upper boundary of the solar convection zone, so $(\alpha - 1) < 0$.

During the excitation of slow motions, the main toroidal velocities in Eqs. (28), (30), and (35) remain approximately constant; i.e., the coefficients $v_{J0}^{(0)}$ and $B_{J0}^{(0)}$ change only slightly. If, in addition, the layer under consideration is sufficiently thin, then the above rough approximation of the radial dependence of nearly equilibrium quantities will be valid. We also assume that $v_{20}^{(-1)}$ and $B_{10}^{(-1)}/(4\pi\rho)^{1/2}$ are proportional to r^χ, where χ is constant. In this approximation and under condition (40), Eq. (35) reduces to

$$(5\pi/3)[(\chi - s + 2)(\chi + 1) - 6]r^2(\partial^2/\partial t^2)v_{20}^{(-1)}$$

$$= (1/2)(\chi + \alpha - s + 3)(\chi + 2\alpha - 3)(D_v + D_b)$$

$$- (5/14)(\alpha - 1)(3\chi + 6\alpha - s - 1)D_b$$

$$+ (2/7)[(2\chi - 3\alpha - 2s + 1)D_v \qquad (44)$$

$$- (3\chi - 2\alpha - s/2 + 4)D_b](\chi + 2\alpha + 2)$$

$$+ (25/7)[(1/3)(\chi + 2\alpha - 1)(\chi - s + 2)$$

$$+ (1/2)(\chi + 2\alpha - s + 1)(\alpha + s/2 - 1)]v_{20}^{(-1)}(A_{20}^{(0)})^2,$$

where $D_v = [v_{10}^{(0)}]^2 v_{20}^{(-1)}$, $D_b = 3^{1/2}v_{10}^{(0)}A_{20}^{(0)}A_{10}^{(-1)}$, and $A_{J0}^{(\lambda)} = B_{J0}^{(\lambda)}/(4\pi\rho)^{1/2}$ is the Alfvén velocity.

If there is no magnetic field, then the satisfaction of condition (41) becomes unnecessary, because $\alpha = 1$ in this case and relation (40) is satisfied. Setting now the right-hand part of Eq. (44) equal to zero yields

$$\chi = \frac{s - 3}{2} \pm \left[\left(\frac{s - 3}{2}\right)^2 + \frac{5s + 12}{3}\right]^{1/2}. \qquad (45)$$

$s = 5$ is apparently typical of the lower boundary of the solar convection zone (see, e.g., Guenther *et al.* 1992); in this case, χ is either 4.64 or –2.64. The solution obtained can describe the sporadically emerging motions of matter attributable to random violations of the equilibrium conditions. Note that the above solution is applicable if α is close to unity, and this condition is satisfied in those layers where the angular velocity depends weakly on radius. In Fig. 1 from Howe *et al.* (2000), such zones are at relative radii of about 0.63 and 0.74 for the equatorial region. The first of these values

agrees with the zone of observed nonperiodic oscillations, whereas the relative radius for the upper oscillation zone is slightly larger than the observed value (0.72). The above hypothesis about the possible nature of the observed oscillations seems to deserve a further study.

In a medium with an antisymmetric (about the equatorial plane) magnetic field, the excitation of flows can be accompanied by variations in dipole magnetic field. In the approximation under consideration, the system of equations for the coefficients $v_{10}^{(0)}$, $B_{20}^{(0)}$, $v_{20}^{(-1)}$, and $B_{10}^{(-1)}$ includes Eqs. (44), (28), (30), and (32). In this case, s and α are considered as specified parameters, while χ, which characterizes the radial dependence of poloidal velocities, is an eigenvalue of the problem. Since we are interested only in very slow motions, we supplement the above equations with yet another relation, which expresses the fact that the equilibrium equation (43) must also hold during the motion of matter in the approximation under consideration. Setting the time derivative of this equation equal to zero yields

$$v_{10}^{(0)}(\partial/\partial t)B_{20}^{(0)} = B_{20}^{(0)}(\partial/\partial t)v_{10}^{(0)}. \qquad (46)$$

Here, the derivatives with respect to t can be represented explicitly using Eqs. (28) and (30). Under the conditions in question, the presence of a weak dipole magnetic field becomes necessary for the existence of a solution.

The derived equations (44), (28), (30), (32), (46), and (43) allow us to study slow steady flows with the corresponding eigenvalues χ for specified s and α; the real velocity ratios $\xi = A_{20}^{(0)}/v_{10}^{(0)}$ and $\eta = A_{10}^{(-1)}/v_{20}^{(-1)}$ can also be determined. Incidentally, the first of these ratios can be easily found from the equilibrium condition (43), while the characteristic values of χ and η are considered below.

For

$$3\alpha + 1 > s/2, \qquad (47)$$

the case in point is usually the bottom of the convection zone, where s is small. In the figure, the derived η and χ are plotted against α for several values of s. For the equatorial layer at the very bottom of the convection zone, $s \approx 5$ and $\alpha \approx 1.5$, so $\chi \approx -6.32$, $\xi \approx 0.483$, and $\eta \approx -2.40$. We failed to find a different solution. It is important that the derived equations contain only the ratio of the radial field and velocity components; therefore, if the direction of poloidal motion changes, the sign of the dipole field will also change. This fact may have a bearing on the variations in solar dipole magnetic field (see section 7).

In the layers adjoining the solar convection zone from above, the density decreases sharply with height and $s \gg 1$. In this case, the system of equations under discussion has an approximate solution:

$$\frac{A_{10}^{(-1)}}{v_{20}^{(-1)}} \approx \pm \frac{29}{9}\left[\frac{5s}{42(1-\alpha)}\right]^{1/2}, \qquad (48)$$

with χ being also characterized by a sharp dependence on r. For example, at $s \sim 10^3$ and $\alpha = -1$, χ is either -74.2 or 41.7 with $\xi = A_{20}^{(0)}/v_{10}^{(0)} \approx 0.0747$ and $|\eta| = |A_{10}^{(-1)}/v_{20}^{(-1)}| \approx 25$; if, alternatively, α is chosen to be -10, then the possible values of χ will be -98.5 and 73.4, while $\xi \approx 0.170$ and $|\eta| \approx 11$.

A distinctive feature of the above solution is a singularity at α close to unity. Equilibrium is possible if α is exactly equal to unity. In that case, however, there must be neither the dipole magnetic field nor the poloidal motion. Thus, the rigid rotation proves to be isolated in that the equilibrium condition is sharply violated when the difference $(\alpha - 1)$ is nearly zero. Since there are always small perturbations in the upper solar layers, the formation of such isolation apparently involves difficulty. An alternative possibility lies in the formation of a structure with an angular velocity decreasing with height. Observations suggest that a structure of the latter type actually takes place on the Sun (see, e.g., Schou *et al.* 1998). This coincidence argues that the medium in the upper solar layers is magnetized. If the density is $\rho \sim 10^{-7}$ g cm^{-3}, the rotation velocity is $r\Omega_1 \approx 2$ km s^{-1}, and $\alpha = -1$, then the maximum azimuthal field will be approximately 16 G; for a dipole field at the pole of 1 G, the equatorial radial velocity will be ≈ 200 cm s^{-1}. Under the same conditions, passing to the model with $\alpha = -10$ will result in an almost twofold increase both in azimuthal field and in equatorial radial velocity. Thus, the models of the upper solar layers under discussion are characterized by outflow of matter, which can also contribute to the heating of the solar corona.

6. A MODEL FOR MAGNETIC-FIELD GENERATION

One of the outstanding problems of solar activity is the mechanism of magnetic-field generation in the convection zone. We consider a simple nonviscous interaction between steady flows and a time-dependent magnetic field assuming that these flows include both rotation and poloidal motion and are described by Eq. (20); in this equation, $u_3 = 0$ and the magnetic field is antisymmetric about the equatorial plane and depends on azimuthal angle as $\sin\varphi$ or $\cos\varphi$. This type of field and the approximate stationarity of velocity **v** agree with those observed on the Sun. However, for simplicity, we take into account only the radial differentiation of solar rotation.

We consider a model in which the vectors **v** and **B** are represented as expansions in terms of vector spherical harmonics, with only terms containing the coefficients $v_{10}^{(0)}$ and $v_{20}^{(\pm 1)}$ being retained in the expansion

for the velocity. An explicit expression for **v** is then given by Eq. (20) at $u_3 = 0$; i.e., the velocity is axisymmetric. However, for a magnetic field that depends on azimuth as $\exp(\pm i\varphi)$, the subscript M is equal to ± 1, so the general expression can be written either as the above expansion in terms of vector harmonics or as

$$\mathbf{B} = -\sum_J \{[\mathbf{i}_r U_J B_{J1}^{(-1)} e^{i\varphi} \sin\vartheta$$

$$+ \mathbf{i}_\vartheta [J(J+1)]^{-1/2}(W_J B_{J1}^{(+1)} e^{i\varphi} - U_J B_{J1}^{(0)} e^{i\varphi}) \quad (49)$$

$$+ \mathbf{i}_\varphi [J(J+1)]^{-1/2}(U_J B_{J1}^{(+1)} i e^{i\varphi} - W_J B_{J1}^{(0)} i e^{i\varphi})] + \text{c.c.}\},$$

where $B_{J1}^{(\lambda)} = B_{J1}^{(\lambda)}(r, t)$, $W_J = d(U_J \sin\varphi)/d\vartheta$, $U_J = U_J(\vartheta)$ is the function of ϑ in the expression for the spherical function $Y_{J,\pm 1} = \mp U_J e^{\pm i\varphi} \sin\vartheta$, $|\lambda| + J$ is odd, $\lambda = 0$ or ± 1, and the letters c.c. or * denote a complex conjugate. Here, $U_1 = (3/8\pi)^{1/2}$, $U_2 = U_1 5^{1/2}\cos\vartheta$, $U_3 = U_1(7/8)^{1/2}(5\cos^2\vartheta - 1)$, etc.; Eq. (19) and the following relations between the coefficients are valid:

$$B_{J-1}^{(0)} = B_{J1}^{(0)*}, \quad B_{J-1}^{(-1)} = -B_{J1}^{(-1)*}. \quad (50)$$

In our case, the time dependence of the field can be found from Eq. (2), which is considerably simplified if an expansion in terms of vector spherical harmonics is used. This equation can be represented as an expansion in terms of the above harmonics by using relations from Vandakurov (1999a, 2001a). As a result, we obtain (see also Vandakurov 2001b)

$$\left(\frac{\partial}{\partial t} + iM\Omega_1\right) B_{J,M}^{(0)} = \frac{U_1}{r}\{(J^2 - 1)^{1/2} f_J D_{J-1,M}$$

$$- [J(J+2)]^{1/2} g_J D_{J+1,M}\}, \quad (51)$$

$$J = 1, 3, \ldots,$$

$$\left(\frac{\partial}{\partial t} + iM\Omega_1\right) B_{J,M}^{(-1)}$$

$$= \frac{U_1}{r} M(30)^{1/2} v_{20}^{(-1)}[f_J B_{J-1,M}^{(0)} + g_J B_{J+1,M}^{(0)}], \quad (52)$$

$$J = 2, 4, \ldots,$$

where

$$f_J = \left[\frac{J+1}{J(2J-1)(2J+1)}\right]^{1/2},$$

$$g_J = \left[\frac{J}{(J+1)(2J+1)(2J+3)}\right]^{1/2}, \quad (53)$$

$$D_{J,M} = \frac{\partial}{\partial r} r v_{10}^{(0)} B_{J,M}^{(-1)} - [J(J+1)]^{1/2} v_{10}^{(0)} B_{J,M}^{(+1)}$$

$$= r^2 B_{J,M}^{(-1)} \frac{\partial}{\partial r}\left[\frac{v_{10}^{(0)}}{r}\right], \quad (54)$$

$M = \pm 1$ and terms of the order of $(v_{20}^{(+1)}/r) B_{J,M}^{(0)}$ were omitted from Eq. (51) for the main toroidal field component.

Eqs. (51)–(52) contain both rapidly oscillating (with angular velocity Ω_1) and slowly varying terms. The frequency of the latter is of the order of $[i\psi]^{1/2}$, where $\psi = v_{20}^{(-1)}(d\Omega_1/dr)$. Note that for latitudinally differential rotation, the angular frequencies of the rapid oscillations generally differ from the angular frequency of rotation (Vandakurov 2001b).

We can pass to the equations that describe the slow oscillations by using the substitution

$$B_{J,M}^{(\lambda)} = e^{-iM\Omega_1 t} Q_{J,M}^{(\lambda)}, \quad (55)$$

As a result, we obtain equations with the same right-hand parts as those in Eqs. (51)–(52) but for the slowly changing variables $Q_{J,M}^{(0)}$ and $Q_{J,M}^{(-1)}$. For example,

$$\frac{\partial}{\partial t} Q_{J,M}^{(-1)} = M\frac{1}{r}\left(\frac{45}{4\pi}\right)^{1/2} v_{20}^{(-1)}[f_J Q_{J-1,M}^{(0)} + g_J Q_{J+1,M}^{(0)}],$$

$$J = 2, 4, \ldots, \quad M = \pm 1. \quad (56)$$

This equation can be used to eliminate the variable $Q_{J,M}^{(-1)}$, which yields

$$\frac{\partial^2}{\partial t^2} Q_{J,M}^{(0)} = -iM\left(\frac{45}{4\pi}\right)^{1/2}$$

$$\times \psi\{(J^2-1)^{1/2} f_J[f_{J-1} Q_{J-2,M}^{(0)} + g_{J-1} Q_{J,M}^{(0)}] \quad (57)$$

$$- [J(J+2)]^{1/2} g_J[f_{J+1} Q_{J,M}^{(0)} + g_{J+1} Q_{J+2,M}^{(0)}]\},$$

$$J = 1, 3, \ldots, \quad M = \pm 1.$$

We see that the radial dependence of velocity $v_{20}^{(-1)}$ in the approximation under consideration is given by

$$\psi = v_{20}^{(-1)} d\Omega_1/dr = \text{const}, \quad (58)$$

with the condition for slow time variations of $Q_{J,M}^{(0)}$ being satisfied if $|\psi|^{1/2} \ll \Omega_1$. In addition, the small terms discarded when deriving Eq. (51) will be much smaller than the retained ones if

$$v_{20}^{(+1)}/(r|\psi|^{1/2}) \ll 1. \quad (59)$$

Significantly, for the poloidal motion for which relation (58) is satisfied, the coefficients in Eq. (57) are con-

stant. Thus, instead of the initial system of partial differential equations, we derive a system of ordinary differential equations (57) for the coefficients $Q_{J,M}^{(0)}(r, t)$, where the radius r acts as a parameter. This suggests that the application of the described procedure of passage to slowly changing variables is valid, although the medium rotates with different angular velocities at different depths.

Since the coefficients in the system of equations (57) are constant, its general solution can be written as $\sum_k A_k \exp(\sigma_k t)$, where $A_k = $ const, k is the number of the particular solution, and σ_k are the roots of the characteristic equation that follows from system (57) if we substitute σ_k for $\partial/\partial t$. By calculating the dimensionless complex eigenvalues

$$q_k = \sigma_k^2/[M(45/4\pi)^{1/2}\psi], \qquad (60)$$

from this system, we can then determine the squares of the reciprocal growth (if $\sigma_k > 0$) or damping (if $\sigma_k < 0$) times for all k modes from relation (60). We performed calculations by retaining only N coefficients $Q_{J,M}^{(0)}$ in Eqs. (57). For example, at $N = 1$, only the coefficient $Q_{1,M}^{(0)}$ is nonzero and $k = 1$. In the next approximation ($N = 2$), another coefficient, $Q_{3,M}^{(0)}$, and an additional mode, $k = 2$, appear, etc. Solutions q_k for the models corresponding to N from 1 to 4 are given in the table.

Of greatest interest are the rapidly growing modes with positive and maximum (in magnitude) real parts of the square root $(q_k)^{1/2}$. In our case, these real parts are nonzero; they are designated as $\mathrm{Re}[(q_k)]_{\max}^{1/2}$ and are given in the last column of the table. Substituting them in Eq. (60) yields the corresponding positive $\mathrm{Re}(\sigma_k)$. We see that these values approach an asymptotic level for $N > 3$; i.e., they cease to depend on N. The corresponding value is the sough-for solution of our problem. Note, however, that $\mathrm{Im}(\sigma_k)$ can significantly depend on the pattern of latitudinal differential rotation.

It should also be emphasized that when the direction of poloidal motion changes, the sign of the generated magnetic field also changes. Indeed, the signs of coefficients $v_{20}^{(-1)}$, $B_{J,M}^{(-1)}$, and $D_{J,M}$ are uniquely related to each other. In addition, when such a sign changes, the passage to another solution for the eigenvalue q_k occurs, which is characterized by the highest rate of increase in the amplitude of the general magnetic field. In turn, the latter passage is accompanied by the change of sign of the toroidal field.

Two important conclusions can be drawn from our results. First, a vibrationally growing (with time) mode is present for any signs of both the coefficient $v_{20}^{(-1)}$ and the radial gradient in angular velocity $d\Omega_1/dr$. Second,

Table

No.	q_k		$\mathrm{Re}[(q_k)_{\max}^{1/2}]$
1	$0.0000 + i0.1000$		0.2236
2	$\pm0.0649 + i0.0417$		0.2665
3	$\pm0.0799 + i0.0199$	$0.0000 + i0.0359$	0.2847
4	$\pm0.0824 + i0.0146$	$\pm0.0250 + i0.0211$	0.2882

the characteristic time τ of the most rapidly growing field modes depends weakly on the number N of retained modes if $N > 3$. Assuming that $q_{\max}^{1/2} \approx 0.29$, we obtain

$$\tau \approx 2.5|\psi|^{-1/2}. \qquad (61)$$

In the main lower part of the solar convection zone, the gradient $d\Omega_1/dr$ can be approximately replaced with $0.1\Omega_1/r$ (see, e.g., Schou *et al.* 1998); the time τ will then be of the order of 10 years if $v_{20}^{(-1)} \sim 10$ cm s^{-1}. In this case, the horizontal poloidal velocities, according to Eq. (20), will be larger than the radial ones approximately by a factor of $|d\ln\rho/d\ln r|$. Under such circumstances, condition (59) will be satisfied for the lower half of the convection zone.

The situation is different in the subsurface layers of the solar convection zone, where the radial gradient in angular velocity is negative and may be larger than the value quoted above by almost two orders of magnitude (in absolute value). Under such conditions and for the same coefficient $v_{20}^{(-1)}$, the field generation under discussion can be faster than that considered above by an order of magnitude. We do not rule out the possible relationship of such a comparatively rapid process to the quasi-biannual cycle of field generation studied by Benevolenskaya and Makarov (1992). In this case, the horizontal poloidal velocities in the solar subsurface layers can reach ~10 m s^{-1}, and condition (59) will be satisfied if $|d\Omega_1/dr|$ is large enough.

Motions with velocities of about 50 m s^{-1} in the layer bounded by the relative radii of 0.97 and 0.999 are known to have been discovered by Gonzalez Hernandez *et al.* (1999) when analyzing helioseismic data. The observed velocities are close or even slightly higher than that quoted above. In this case, the motion was directed poleward with a maximum horizontal velocity somewhere at mid-latitudes, in agreement with Eq. (20) for the general slow rise of the medium in the equatorial region and for its sinking at high latitudes.

7. DISCUSSION

The hypothesis under consideration is that a state in which the maximum possible amount of energy coming

to the convection zone transforms into magnetic energy is realized on the Sun. We performed a preliminary analysis for an equatorial region in which the latitudinal differentiation of rotation velocity can be disregarded in the first approximation. These analyses argue that the above transformation can take place and that the main generated magnetic field will be of the solar type if the following three main conditions are satisfied.

First, a radial gradient in angular velocity whose sign is of little importance must be present. Second, there must be a poloidal component of the medium displacement, which, for the most effective interaction with the field, corresponds to the axisymmetric sinking (or rise) of matter in the central zone and to its rise (or sinking) in the axial region. This structure of motions coincides with that found by Gonzalez Hernandez *et al.* (1999) in the upper layers of the solar convection zone. Under conditions typical of the lower layer of the convection zone, the radial velocities are slightly lower than 10 cm s^{-1}. The third condition is the stationarity of total velocity vector **v**, although it remains unclear how important this condition is. The field generation simultaneously with a significant change in the distribution of rotation velocity appears to be severely hampered. Therefore, it may well be that the latitudinal differentiation of rotation is established from the condition that the velocity field is approximately stationary. Observational data also confirm that the latter condition is satisfied on the Sun.

However, the field cannot grow to infinity; therefore, it seems plausible that when the field reaches the limiting permissible strength in particular layers, turbulent viscosity will be excited, which will facilitate the cessation of field generation. If turbulent magnetic viscosity ζ is included in Eqs. (51)–(52), then the term $(\partial/\partial t) B_{JM}^{(\lambda)}$ will be replaced by

$$\frac{\partial}{\partial t} B_{JM}^{(\lambda)} - \frac{1}{r}\frac{\partial}{\partial r}\zeta\frac{\partial}{\partial r}[rB_{JM}^{(\lambda)}] + J(J+1)\frac{\zeta}{r^2}B_{JM}^{(\lambda)},$$

where λ is equal to 0 or –1. Clearly, the effect of increase in field strength with time can be eliminated for an appropriate $\zeta(r, t)$ distribution. We assume that, because the transformation of thermal energy into magnetic energy must be resumed, conditions will be created under which a similar effect will cause a reversal of the poloidal velocity. To put it another way, a wave of change both in the direction of the poloidal flow and in the sign of the generated magnetic field will be triggered. As a result, we obtain a model of the solar cycle in which the sign of the emerging field changes cyclically.

It follows from the calculations of section 5 that the penetration of the poloidal motions considered above into the lower lying subconvection layers can give rise to an additional zone of the transformation of thermal energy into the energy of dipole magnetic field in these layers. First, it should be noted that the condition of

mechanical equilibrium is violated in a nonmagnetic radiative zone with a nonzero radial gradient in angular velocity. The latter condition can be satisfied in the presence of an axisymmetric azimuthal magnetic field. For an antisymmetric (about the equator) field, its maximum strength (at latitude ±45°) is approximately 170 kG. If a cyclically changing motion of matter emerges in such a medium, then a time-dependent dipole magnetic field whose symmetry is the same as that of the solar dipole field will inevitably appear. It is also important that the field sign changes concurrently with the direction of the radial flow (section 5). Hence, the flow variations are attributable to the generation of a new dipole magnetic field.

The latter field is generally believed to appear on the Sun through the decay and diffusion of a strong spot field. However, Makarov and Tlatov (2000) have recently showed that the observed weak large-scale solar magnetic field does not result from the decay of strong fields in active regions; on the contrary, the appearance of this field precedes the 11-year sunspot cycle by 5.5 years, on average. In our model, the sign of the dipole field changes simultaneously with the direction of the poloidal motion of matter; i.e., these events occur at the very outset of a new generation cycle of the main toroidal field. Consequently, the generation sequence of the dipole and toroidal magnetic fields coincides with that found by Makarov and Tlatov (2000). If $\rho \sim 0.2$ g cm^{-3}, $s \sim 5$, $\alpha \sim 1.5$, and $v_{20}^{(-1)} \sim 10$ cm s^{-1} at the bottom of the convection zone under consideration, then we find, by using the figure, that the radial magnetic field on the axis is $B_r \sim 19$ G.

The phenomena under study are coupled mainly with large-scale heat transport. However, these phenomena take place in the convection zone, in which turbulent heat transport plays a major role. It is therefore clear that the total energy E_B lost through the transformation of thermal energy into magnetic energy followed by field removal into the surrounding space must be much smaller than the total emitted energy E. The experimental E_B/E ratio is 0.1% (Foukal and Lean 1988). Previously (Vandakurov 1999b, 2001a), we obtained the same fraction of energy when studying magnetized models of a differentially rotating solar convection zone on condition that the pattern of motion did not depend on the type of magnetic field. In this case, the magnetic field in the lower layers was ~10 kG. Thus, the model under discussion has consistent parameters, and it deserves a further study.

In conclusion, note that the equilibrium conditions near the upper boundary of a rotating convection zone if it lies in a low-density region are not simple. In this case, as was shown in section 5, the rigid rotation can be equilibrium one, but the state corresponding to any small deviation from this rotation law is a highly nonequilibrium one. Under such conditions, the formation of a state with an angular velocity decreasing with height seems more likely. It may well be that the spin-

down of the surface layers observed on the Sun is associated with this. Note also that the magnetic-field generation we considered can also take place for a negative gradient in angular velocity (see Section 6).

ACKNOWLEDGMENTS

REFERENCES

1. E. E. Benevolenskaya and V. I. Makarov, Pis'ma Astron. Zh. **18**, 195 (1992) [Sov. Astron. Lett. **18**, 108 (1992)].
2. P. A. Foukal and J. Lean, Astrophys. J. **328**, 347 (1988).
3. A. Gailitis, Magn. Gidrodin. **1**, 19 (1970).
4. P. A. Gilman, Astrophys. J. Lett. **544**, L79 (2000).
5. I. González Hernández, J. Patrón, R. S. Bogart, *et al.*, Astrophys. J. Lett. **510**, L153 (1999).
6. D. B. Guenther, P. Demarque, Y.-C. Kim, *et al.*, Astrophys. J. **387**, 372 (1992).
7. R. Howe, J. Christensen-Dalsgaard, F. Hill, *et al.*, Science **287**, 2456 (2000).
8. F. Krause and K. Radler, *Mean-Field Magnetohydrodynamics and Dynamo* (Akademie-Verlag, Berlin, 1980; Mir, Moscow, 1984).
9. V. I. Makarov and A. G. Tlatov, Astron. Zh. **77**, 858 (2000) [Astron. Rep. **44**, 759 (2000)].
10. J. Schou, H. M. Antia, S. Basu, *et al.*, Astrophys. J. **505**, 390 (1998).
11. J.-L. Tassoul, *Theory of Rotating Stars* (Princeton Univ. Press, Princeton, 1979; Mir, Moscow, 1982).
12. Yu. V. Vandakurov, Astron. Zh. **76**, 29 (1999a) [Astron. Rep. **43**, 24 (1999)].
13. Yu. V. Vandakurov, Pis'ma Astron. Zh. **25**, 868 (1999b) [Astron. Lett. **25**, 758 (1999b)].
14. Yu. V. Vandakurov, Astron. Zh. **78**, 253 (2001a) [Astron. Rep. **45**, 216 (2001a)].
15. Yu. V. Vandakurov, Izv. Vyssh. Uchebn. Zaved., Radiofiz. (2001b) (in press).
16. Yu. V. Vandakurov, Zh. Tekh. Fiz. **71** (6), 1 (2001c) [Tech. Phys. **46**, 645 (2001c)].

Translated by V. Astakhov

Heterogeneity of the Interstellar Diamond in the CV3 Meteorite Efremovka

A. V. Fisenko[1]*, A. B. Verchovsky[2], L. F. Semjonova[1], and C. T. Pillinger[2]

[1] *Vernadsky Institute of Geochemistry and Analytical Chemistry, Russian Academy of Sciences, ul. Kosygina 19, Moscow, 117975 Russia*
[2] *Institute for Planetary Research, Open University, Milton Keynes, UK*
Received February 21, 2001

Abstract—Based on the heterogeneity in the contents and isotopic compositions of carbon, nitrogen, and rare gases found in different (in grain size) interstellar diamond fractions of the meteorite Efremovka, we discuss issues associated with the nature of the diamond, the distribution of the isotopic components of impurity chemical elements in it, and the kinetics of their release. © *2001 MAIK "Nauka/Interperiodica".*

Until now, almost all studies of interstellar diamond (ID) in meteorites have been carried out by using bulk samples. This has significantly limited the ID investigation compared, for example, to interstellar SiC and graphite, whose grain sizes in several cases are large enough to analyze them individually. The latter is not possible for ID because of the Angstrom sizes of its grains (Lewis *et al.* 1989).

For the first time, we have separated ID of the meteorite Efremovka into fractions by grain sizes using sedimentation via ultracentrifugation (about 10^5 g) and simultaneously measured the amounts of released carbon, nitrogen, and rare gases and their isotopic composition during stepped pyrolysis and oxidation of these fractions (Verchovsky *et al.* 1998; Fisenko *et al.* 1998, 2000). Here, we present data on the heterogeneity of ID fractions and discuss its nature.

For the fractions as a whole, the contents of the elements studied and their weighted mean isotopic compositions calculated from the data obtained during the stepped pyrolysis (300–2000°C) and oxidation (300–1000°C) of fractions are given in the table. The standard deviations for $\delta^{13}N$ and $\delta^{15}C$ do not exceed 1 and 3‰ (1σ), respectively. The measurement errors in the contents of rare gases, carbon, and nitrogen are no larger than 10, 5, and 2%, respectively.

All diamond fractions, like bulk ID samples (Russell *et al.* 1996), are depleted of the ^{13}C and ^{15}N isotopes and contain the HL component of rare gases of nucleogenic origin whose xenon is simultaneously enriched with light and heavy isotopes. The fractions are also similar to the bulk diamond samples in the release

kinetics of carbon and nitrogen isotopic components: as the degree of oxidation or pyrolysis increases, the fraction of released components enriched with heavy isotopes of these elements decreases. Such a similarity of diamond fractions to bulk samples suggests either a common nature of the diamond grains or homogeneous mixing in a protoplanetary cloud of grain populations that have different astrophysical sources but are similar in their sizes. At the same time, the diamond fractions differ in the contents of nitrogen and rare gases, in their isotopic composition, and in the isotopic composition of carbon, particularly the coarse-grain fraction from the fine-grain one (table). Such differences for the diamond aliquots of the same meteorite have been revealed for the first time.

The carbon enrichment with ^{13}C in the fine-grain fractions, to a first approximation, is consistent with the model of diamond-grain production by the chemical vapor deposition of atomic carbon in the gaseous medium (CVD process) of the outer part of an expanding helium shell after a supernova explosion (Clayton *et al.* 1995), in which the content of the heavy carbon isotope gradually increases. However, the degree of this enrichment is considerably lower than that suggested by the model of Clayton *et al.* (1995). Thus, for example, the difference in $\delta^{13}C$ for EA-4 and EA-9 can reach 60‰ instead of the observed 7‰ (table). In this model, it should probably be assumed that the diamond grains grew in different regions of the supernova helium shell, in which the carbon isotopic composition changed differently.

An alternative to the above model is that the surface layers of diamond grains of all sizes are enriched with ^{13}C. In this case, to explain the data requires that, for example, a mere ~12 and 41 carbon atoms from the supernova helium shell [$\delta^{13}C$ ~ 3100‰ (Clayton *et al.*

* E-mail address for contacts: anatolii@fis.home.chg.ru

Contents and isotopic compositions of C, N, and rare gases in the interstellar-diamond fractions of the meteorite Efremovka

Parameters	EA-3	EA-2	EA-4	EA-9
Grain size, nm	1.5(0.7–3.1)	1.8(1.5–2.7)	2.0(1.2–2.7)	3.7(1.5–9.0)
$\delta^{13}C$, ‰	–26.0	–26.3	–26.3	–32.8
N, %	0.92	0.71	0.95	0.87
$\delta^{15}N$, ‰	–204	–225	–239	–282
^{4}He, cm^3 g^{-1} C	0.0085	0.0098	0.011	0.019
^{20}Ne, cm^3 g^{-1} C	6.9×10^{-5}	9.9×10^{-5}	8.1×10^{-5}	1.3×10^{-4}
^{20}Ne/^{22}Ne	8.74 ± 0.10	8.39 ± 0.10	8.44 ± 0.10	8.26 ± 0.10
^{21}Ne/^{22}Ne, 10^{-2}	3.0 ± 0.2	3.1 ± 0.1	3.2 ± 0.1	4.0 ± 0.3
^{36}Ar, cm^3 g^{-1} C	7.1×10^{-6}	10.0×10^{-6}	1.3×10^{-5}	3.3×10^{-5}
^{38}Ar/^{36}Ar	0.216 ± 0.003	0.208 ± 0.002	0.217 ± 0.005	0.196 ± 0.004
^{132}Xe, cm^3 g^{-1} C	1.6×10^{-7}	1.6×10^{-7}	1.9×10^{-7}	4.0×10^{-7}
^{136}Xe/^{132}Xe	0.678 ± 0.008	0.671 ± 0.010	0.659 ± 0.010	0.609 ± 0.007
^{134}Xe/^{132}Xe	0.637 ± 0.009	0.609 ± 0.010	0.614 ± 0.010	0.572 ± 0.009
^{129}Xe/^{132}Xe	1.030 ± 0.010	1.051 ± 0.010	1.015 ± 0.010	1.080 ± 0.010

1995)] be added to the grains with mean sizes of about 2 and 4 nm (EA-4 and EA-9 fractions, respectively) under the assumption that the ^{12}C/^{13}C ratio for the diamond was initially 92.7 (δ^{13}C = –40‰). Note that the ratio of the numbers of carbon atoms added to the grains with the above sizes is similar to the surface ratio of these grains. This may be considered as an indirect confirmation of the autoepitaxial buildup of heavy carbon on diamond grains. In the case under consideration, the latter could be produced both by the CVD process in a medium with a constant carbon isotopic composition and during a rapid nonequilibrium process from carbonaceous phases under the effect of shock waves near a supernova (Blake *et al.* 1988; Fisenko *et al.* 2000).

By analogy with carbon, the difference between the diamond fractions in the nitrogen isotopic composition can be explained by also invoking its two components: one is surface-bonded and enriched with ^{15}N and the other is volume-bonded and enriched with ^{14}N. The latter component may have initially been contained in the carbonaceous phases (or in the gaseous medium) from which (or in which) the diamond grains were formed. Heavy nitrogen could be added to the grain surface layer through chemisorption and/or adsorption in a protoplanetary cloud and/or during the release of diamond from meteoritic material under laboratory conditions. In the former and latter cases, the source could be the solar wind and the Earth's atmosphere, respectively.

For stepped oxidation, the concentration curves of the released nitrogen, argon, and xenon are similar for all fractions, but the variations in these concentrations between the elements significantly differ in pattern (Fig. 1). When interpreting this result, we adhere, as was done by Russell *et al.* (1996) and Clayton *et al.* (1995), to the model of the layer-by-layer oxidation of diamond grains. In this case, the dependencies in Fig. 1 are determined mainly by the distribution of elements over the grain volume or, more specifically, by the fact that Ar atoms enrich the grain subsurface region, while N atoms enrich their central part. Xe atoms are distributed over the grain volume more or less uniformly. The enhanced xenon yield at the initial oxidation stage of EA-3 and EA-4 probably results from the oxidation of the finest grains. Note that the concentration profiles for He and Ne are similar to those for N and Xe, respectively.

The revealed features in the distribution of rare gases in diamond grains cannot be explained by the diffusion of elements at a particular ID evolutionary stage because of the different directions of radial gradients for Ar, on the one hand, and for Ne and Xe, on the other. They are probably attributable directly to the capture (captures) of these gases by diamond grains, for example, by implantation (Verchovsky *et al.* 1999). If it was implantation, then it must have proceeded in several steps. For example, Ar and Xe were implanted under some conditions, whereas Ne was implanted under other conditions. Note that the implantation of rare gases into a diamond, at least of the Xe–HL component, was previously suggested to justify the absence of ^{129}Xe excesses in it (Lewis and Anders 1981). Helium diffusion at one of the diamond evolutionary stages may have significantly affected only its distribution in the grains.

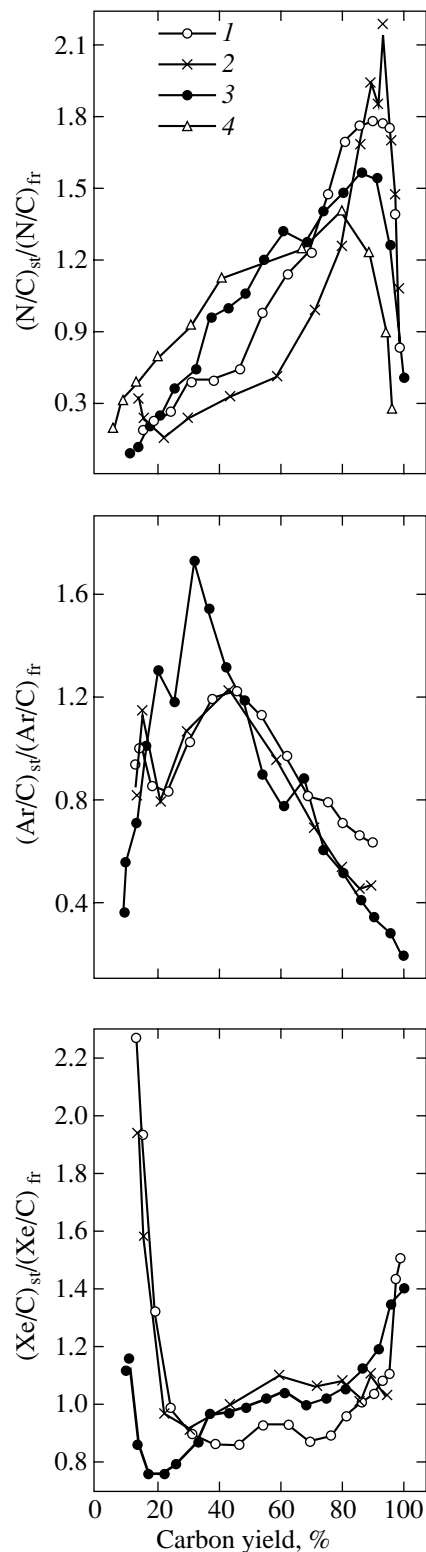The peculiar features in the distribution of nitrogen atoms over the volume of the fraction diamond grains

Fig. 1. Relative concentrations of elements versus total carbon yield during the oxidation of different (in grain sizes) diamond fractions in the meteorite Efremovka (*1–3*) and a sample of synthetic diamond of detonation synthesis (*4*). *1, 2,* and *3* are the EA-3, EA-4, and EA-9 fractions, respectively. The subscripts "st" and "fr" correspond to the values for each step and the fraction as a whole.

result mainly from the diffusion losses of some of its fraction from the grains during diamond formation. This assumption is based on the similarity between the nitrogen concentration profiles for ID and nanometer diamond of detonation synthesis, which was not heated above 200°C (Fig. 1). Considering the Angstrom sizes of ID, we must assume that the nitrogen diffusion losses are of a short duration. This constraint is consistent with the model of ID production during a highly nonequilibrium process in a gaseous medium composed of carbonaceous phases under the effect of shock waves during supernova explosions (Blake *et al.* 1988; Fisenko *et al.* 2000). The production of diamond by the CVD process requires an additional, short-duration and high-temperature heating. There were also nitrogen diffusion losses at the last high-temperature oxidation stages in the experiment, as suggested by the reduction in nitrogen concentration by the end of the oxidation (Fig. 1).

During the pyrolysis of EA-2 and EA-9, the N and Ne release curves were bimodal (Fig. 2). In the temperature range of the first peak (800–1100°C), the yield of elements depends, to some extent, on their masses; i.e., we may assume that the release of elements in this temperature range is attributable mainly to their diffusion. This is indirectly confirmed by the fact that the maximum of element release for the EA-2 fine-grain fraction occurs at a lower temperature than that for the coarse-grain fraction.

If nitrogen in the crystal lattice of ID diamond is in the form of single atoms and their associations (Russell 1992; Hill *et al.* 1997), then a higher activation energy of the disperse nitrogen atoms than that for the associations could lead to the observed pattern of the difference in its release from the fine- and coarse-grain diamond fractions during pyrolysis. In this case, it is necessary that the fine-grain diamond be depleted of nitrogen atom associations from the outset, i.e., at its formation stage. The enrichment of coarse diamond grains with associations of nitrogen atoms was also suggested by Hill *et al.* (1997) based on infrared spectrometry of ID. After the release of clusters of nitrogen atoms, the vacancies could probably cause an increase in the diffusion of other elements, particularly the lightest (in mass) ones (helium).

According to the data obtained during the pyrolysis of fractions above 1100°C, when the main process of diamond grain destruction is their graphitization, the curves of total nitrogen and rare-gas yield as a function of pyrolysis temperature for EA-2 pass systematically lower than those for EA-9; i.e., the EA-2 grains are more heat-resistant than the EA-9 grains. This may be attributable to an increase in the fraction of defective grains and/or in the degree of their defectiveness with increasing diamond grain size due to variations in the PT conditions of ID grain growth and/or in the composition of the gaseous medium in which this process proceeded.

The higher defectiveness of the coarse-grain diamond and its enrichment with associations of nitrogen atoms could result in the observed sharp reduction (by a factor of 2 or 3) in the nitrogen content in bulk diamond samples of meteorites that underwent thermal metamorphism (Russell *et al.* 1996) due to the destruction of most of the coarse-grain diamond.

Differences in the depth distributions of Ar and Xe atoms in diamond grains can be used to elucidate the release mechanism of these atoms during the stepped pyrolysis or oxidation of diamond. The Efremovka CV3 chondritic material underwent thermal metamorphism (Guilmon *et al.* 1995). In this case, as suggested by Koshcheev *et al.* (2000a, 2000b), the remaining Ar and Xe atoms are in defects of the diamond crystal lattice with a high activation energy, and their releases must differ from each other and depend on heating temperature. Therefore, the patterns of change in the ratio of Ar to Xe released during the pyrolysis and oxidation of diamond must be different because of the sharply different ranges of heating temperatures for these processes and depth distributions of these elements. However, as we see from Fig. 3, this does not occur. This figure shows the plots of normalized Ar/Xe ratios against total Xe yield constructed from the data obtained for the EA-9 coarse-grain fraction during its pyrolysis (300–2000°C) and oxidation (300–800°C). We see that the pattern of change in Ar/Xe ratio for the two processes of diamond grain destruction is essentially the same after ~18% of xenon is released.

Thus, we assume that the bulk of the Ar and Xe is released mainly when the crystal lattice of the diamond grains is destroyed, and that the destruction of at least coarse diamond grains during pyrolysis and oxidation proceeds more or less similarly, for example, as suggested above, layer by layer. This means that the argon and xenon atoms of all rare-gas components in the diamond of the meteorite Efremovka are firmly held by the crystal lattice of the diamond grains and are released mostly only during its destruction.

In the original ID, i.e., before its combination with matter of the meteorite parent bodies in a protoplanetary cloud, the positions of the atoms of rare-gas components are probably slightly different: the atoms of the isotopically anomalous component are mostly in defects of the diamond crystal lattice with an extremely high activation energy, whereas those of the isotopically normal component are both in defects of these types and in defects with a considerably lower activation energy. As a result of the latter, the atoms of rare gases contained in them are lost almost completely during thermal metamorphism of material of the meteorite parent bodies or when heated to a temperature of ~700°C under laboratory conditions. As suggested by Koshcheev *et al.* (2000a), atoms of these rare-gas components were captured by diamond grains through implantation at different temperatures: above 700°C for
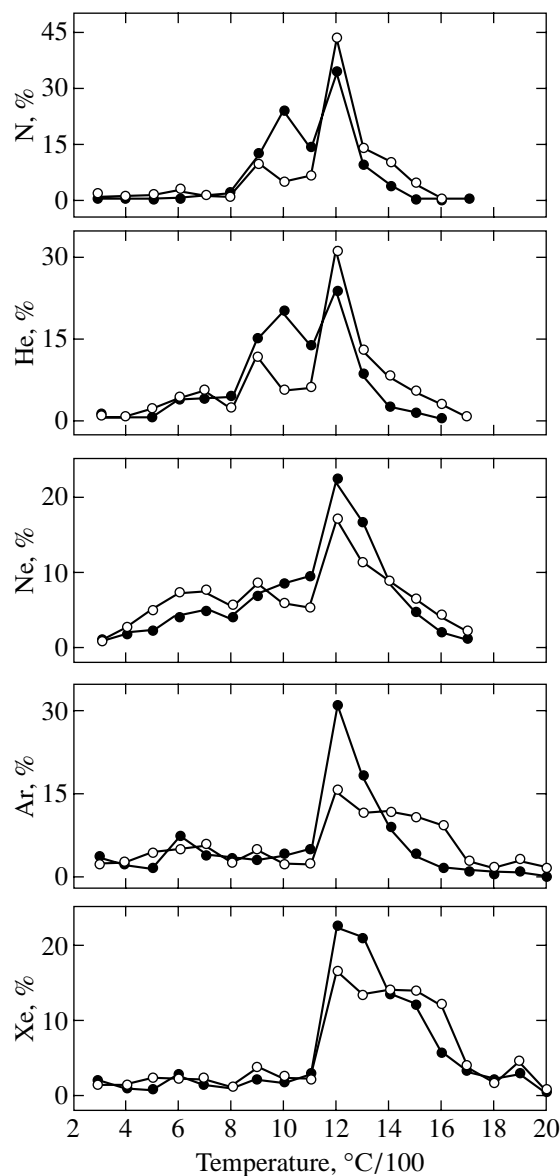

Fig. 2. Relative yield of elements versus EA-2 (open symbols) and EA-9 (filled symbols) pyrolysis temperature.

the isotropically anomalous component and at lower temperatures for the P3 component.

Thus, the revealed heterogeneity in the contents and isotopic compositions of C, N, and rare gases in different (in grain sizes) ID fractions of the meteorite Efremovka leads us to the following main conclusions. (1) The heterogeneity of the diamond fractions is attributable to different ratios of the same isotopic components of chemical elements. This suggests either a single astrophysical source of ID or homogeneous mixing in a protoplanetary cloud of different populations of diamond grains but similar in their size distribution. (2) The production of ID during a highly nonequilibrium process in a gaseous medium composed of car-
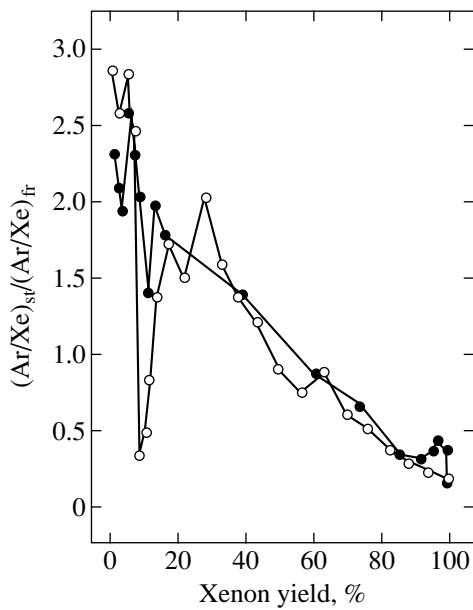
Fig. 3. Ratio of argon and xenon relative yields versus total xenon yield during EA-9 pyrolysis (filled symbols) and oxidation (open symbols). ^{36}Ar and ^{132}Xe were used to calculate the ratio.

bonaceous phases under the effect of shock waves during supernova explosions is more consistent with our data obtained than the CVD process. (3) The heterogeneous distribution of rare-gas and nitrogen atoms over the grain volume is attributable, respectively, to the different conditions of their implantation and to diffusion losses during the formation of diamond grains. Argon and xenon in ID of the meteorite Efremovka are contained in defects of the diamond grain crystal lattice with an extremely high activation energy; as a result, the atoms of these elements are released mostly during grain destruction. (4) The model of two-component carbon and nitrogen, in which the heavy (in isotopic composition) component of each of the elements is surface-bonded and the light component is volume-bonded, is most suitable for explaining the isotopic data for these elements obtained during the oxidation or pyrolysis of diamond fractions.

REFERENCES

1. D. Blake, P. Freund, T. Bunch, *et al.*, in *Abstracts of the Lunar and Planetary Science Conference, 1988*, Vol. 19, p. 94.
2. D. D. Clayton, C. I. Sanderson, S. S. Russell, and C. T. Pillinger, Astrophys. J. **447**, 894 (1995).
3. A. V. Fisenko, L. F. Semenova, A. S. Aronin, *et al.*, Geokhimiya, No. 5, 532 (1998).
4. A. V. Fisenko, A. B. Verkhovskiĭ, L. F. Semenova, and K. T. Pillindzher, Astron. Vestn. **34**, 24 (2000).
5. R. K. Guilmon, S. K. Symes, D. W. G. Sears, and P. H. Benoit, Meteoritics **30**, 704 (1995).
6. H. G. M. Hill, L. B. D'Hendecourt, C. Perron, and A. P. Jones, Meteorit. Planet. Sci. **32**, 713 (1997).
7. A. P. Koscheev, M. D. Gromov, S. Herrmann, and U. Ott, in *Proceedings of the 31st Annual Lunar and Planetary Science Conference, Houston, 2000a*, CD-ROM, Abstract No. 1551.
8. A. P. Koscheev and U. Ott, Meteorit. Planet. Sci., Suppl. **35**, A92 (2000b).
9. R. S. Lewis and E. Anders, Astrophys. J. **247**, 1122 (1981).
10. R. S. Lewis, E. Anders, and B. T. Draine, Nature **339**, 117 (1989).
11. S. S. Russell, PhD Thesis (Department of Earth Sciences, Open Univ., 1992).
12. S. S. Russell, J. W. Arden, and C. T. Pwlinger, Meteorit. Planet. Sci. **31**, 343 (1996).
13. A. B. Verchovsky, A. V. Fisenko, L. F. Semjonova, *et al.*, in *Proceedings of the 30th Annual Lunar and Planetary Science Conference, Houston, 1999*, CD-ROM, Abstract No. 1757.
14. A. B. Verchovsky, A. V. Fisenko, L. F. Semjonova, *et al.*, Science **281**, 1165 (1998).

Translated by V. Astakhov

=== **ERRATA** ===

Erratum: "Ultrahigh-Energy Gamma-Ray Emission from the Geminga Pulsar"
[*Pis'ma Astron. Zh.* 27, 266 (2001); *Astronomy Letters* 27, 228 (2001)]

**Yu. I. Neshpor, A. A. Stepanyan, Yu. L. Zyskin, O. R. Kalekin,
V. P. Fomin, N. N. Chalenko, and V. G. Shitov**

On page 269, the value $\dot{T}$ with a minus in the left column in line 11 from above should be with a plus. The same mistake takes place on the same page and in the same column in lines 12 and 15.

Page 269, left column, line 11 from above

Printed: –1.09715948, should be: 1.09715948; page 269, left column, line 12 from above

Printed: –1.09765, should be: 1.09765; page 269, left column, line 15 from above

Printed: –1.09713706, should be: 1.09713706.

Thus, the above sentences should be read as follows:

We used the above results to compute the period and its derivative for the epoch of our observations. For November 13, 1996, $T = 0.2370993496$ s and $\dot{T} = 1.09715948 \times 10^{-14}$ s s^{-1} (Mattox *et al.* 1998) and $T = 0.2370993506$ s and $\dot{T} = 1.09765 \times 10^{-14}$ s s^{-1} (Shitov and Pugachev 1997) (the second derivative was not determined). For November 1, 1997, $T = 0.2370996833$ s and $\dot{T} = 1.09713706 \times 10^{-14}$ s s^{-1} (Mattox *et al.* 1998) and $T = 0.2370996845$ s and its derivative is the same (Shitov and Pugachev 1997).